

2

# NAVAL POSTGRADUATE SCHOOL Monterey, California

AD-A238 487



DTIC  
ELECTE  
JUL 16 1991  
S B D

## THESIS

EXPERIMENTAL ANALYSIS OF B-DOT SENSORS

by

Holly L. Nye

June 1990

Thesis Advisor:

J. Neighbours

Approved for public release; distribution is unlimited

91-04935



91 7 12 064

UNCLASSIFIED

SECURITY CLASSIFICATION OF THIS PAGE

REPORT DOCUMENTATION PAGE

Form Approved OMB No 0704-0188

1a REPORT SECURITY CLASSIFICATION <b>UNCLASSIFIED</b>		1b RESTRICTIVE MARKINGS	
2a SECURITY CLASSIFICATION AUTHORITY		3 DISTRIBUTION AVAILABILITY OF REPORT Approved for public release; distribution is unlimited	
2b DECLASSIFICATION/DOWNGRADING SCHEDULE			
4 PERFORMING ORGANIZATION REPORT NUMBER(S)		5 MONITORING ORGANIZATION REPORT NUMBER(S)	
6a NAME OF PERFORMING ORGANIZATION Naval Postgraduate School	6b OFFICE SYMBOL (If applicable)	7a NAME OF MONITORING ORGANIZATION Naval Postgraduate School	
6c ADDRESS (City, State, and ZIP Code) Monterey, California 93943-5000		7b ADDRESS (City, State, and ZIP Code) Monterey, California 93943-5000	
8a NAME OF FUNDING SPONSORING ORGANIZATION	8b OFFICE SYMBOL (If applicable)	9 PROCUREMENT INSTRUMENT IDENTIFICATION NUMBER	
8c ADDRESS (City, State, and ZIP Code)		10 SOURCE OF FUNDING NUMBERS	
		PROGRAM ELEMENT NO	PROJECT NO
		TASK NO	WORK UNIT ACCESSION NO
11 TITLE (Include Security Classification) <b>EXPERIMENTAL ANALYSIS OF B-DOT SENSORS</b>			
12 PERSONAL AUTHOR(S) NYE, Holly L.			
13a TYPE OF REPORT Master's Thesis	13b TIME COVERED FROM _____ TO _____	14 DATE OF REPORT (Year, Month, Day) June 1990	15 PAGE COUNT 167
16 SUPPLEMENTARY NOTATION The views expressed in this thesis are those of the author and do not reflect the official policy or position of the Department of Defense or the U.S. Government			
17 COSATI CODES		18 SUBJECT TERMS (Continue on reverse if necessary and identify by block number)	
FIELD	GROUP	SUB-GROUP	
		B-dot sensors; non-self integrating inductive loop sensors; REX	
19 ABSTRACT (Continue on reverse if necessary and identify by block number) A new design for non-self integrating magnetic-loop sensors (B-dots) has been developed at Los Alamos National Laboratory. Experiments and tests were performed using the Relativistic Electron Beam Experiment (REX) machine to compare the B-dot sensors to optical beam diagnostics (streak camera). The B-dots were assessed to have the capability of measuring the REX electron beam's position to within 0.25mm with 2 percent error, and its transverse oscillatory movement to within 0.5mm amplitude, with 7 percent error, over a 1 GHz bandwidth. Many calibration parameters and factors affecting sensor signals were examined during the experiment. The experimental calibration of the B-dots, and the resulting certified accuracy of their remote, non-instrusive measurements of relativistic electron beam parameters should have a wide range of application to many other electron beam machines.			
20 DISTRIBUTION AVAILABILITY OF ABSTRACT <input checked="" type="checkbox"/> UNCLASSIFIED, UNLIMITED <input type="checkbox"/> SAME AS PRT <input type="checkbox"/> DTIC USERS		21 ABSTRACT SECURITY CLASSIFICATION <b>UNCLASSIFIED</b>	
22a NAME OF RESPONSIBLE INDIVIDUAL NEIGHBOURS, John R.		22b TELEPHONE (Include Area Code) 408-646-2922	22c OFFICE SYMBOL PH/Nb

Approved for public release; distribution is unlimited

Experimental Analysis of Beam B-dot Sensors

by

Holly Lawrence Nye  
Lieutenant Commander, United States Navy  
B.S., Oregon State University, 1976

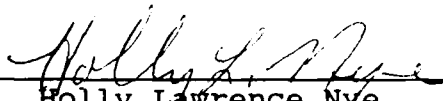
Submitted in partial fulfillment of the  
requirements of degree of

MASTER OF SCIENCE IN PHYSICS

from the

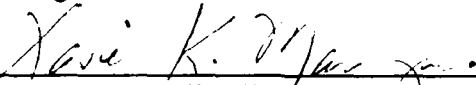
NAVAL POSTGRADUATE SCHOOL  
June 1990


Author:

  
\_\_\_\_\_  
Holly Lawrence Nye

Approved by:

  
\_\_\_\_\_  
J. R. Neighbours, Thesis Advisor

  
\_\_\_\_\_  
X. K. Maruyama, Second Reader

  
\_\_\_\_\_  
K. E. Woehler, Chairman  
Department of Physics

ABSTRACT

A new design for non-self integrating magnetic-loop sensors (B-dots) has been developed at Los Alamos National Laboratory. Experiments and tests were performed using the Relativistic Electron Beam Experiment (REX) machine to compare the B-dot sensors to optical beam diagnostics (streak camera). The B-dots were assessed to have the capability of measuring the REX electron beam's position to within 0.25mm with 2 percent error, and its transverse oscillatory movement to within 0.5mm amplitude with 7 percent error, over a 1 GHz bandwidth. Many calibration parameters and factors affecting sensor signals were examined during the experiment. The experimental calibration of the B-dots, and the resulting certified accuracy of their remote, non-intrusive measurements of relativistic electron beam parameters should have a wide range of application to many other electron beam machines.

Accession For	
NTIS GRA&I	<input checked="" type="checkbox"/>
DTIC TAB	<input type="checkbox"/>
Unannounced	<input type="checkbox"/>
Justification	
By _____	
Distribution/	
Availability Codes	
Dist	Avail and/or Special
A-i	



TABLE OF CONTENTS

I. INTRODUCTION.....1

II. THEORY OF B-DOT MEASUREMENTS.....8

III. DESCRIPTION OF RELATIVISTIC ELECTRON EXPERIMENT (REX)...15

IV. EXPERIMENTS.....23

    A. EXPERIMENTAL GOALS:PRELIMINARY EXPERIMENT.....23

    B. PRELIMINARY EXPERIMENT AND CONCLUSIONS.....26

    C. EXPERIMENTAL GOALS:CALIBRATION EXPERIMENT.....42

    D. CALIBRATION EXPERIMENT.....43

        1. Test Stand Phase Procedure.....43

        2. Test Stand Phase Data Collection, Reduction,  
           and Results.....47

            (a) Port-to-Port Differences for  
                B-dot Rings.....47

            (b) Individual B-dot Loop Area Measurement...49

            (c) B-dot Sensitivity to Static Position....52

            (d) Sources of Experimental Error.....63

        3. Dynamic Phase Procedure.....67

        4. Dynamic Phase Data Collection, Reduction,  
           and Results.....68

            (a) Factors Affecting Waveform Shape.....68

            (b) Fourier Analysis.....73

            (c) Comparison of B-dot Signals with 74  
                Streak Camera Data.....74

V. CONCLUSIONS.....93

APPENDIX A:EQUATIONS USED IN DATA ANALYSIS.....97

APPENDIX B:DESCRIPTIONS OF REX.....114

APPENDIX C:DESCRIPTIONS OF EQUIPMENT.....126

APPENDIX D: B-DOT DETAILED DRAWINGS.....142  
APPENDIX E: DATA TABLES.....146  
LIST OF REFERENCES.....155  
BIBLIOGRAPHY.....157  
DISTRIBUTION LIST.....158

## ACKNOWLEDGEMENT

At this time, I would like to voice my gratitude to many people who made it possible for me to participate in this experiment.

The experience, technical expertise, and hard work of Dr. Randolph L. Carlson, Dr. David C. Moir, Mr. Todd J. Kauppila, and Mr. Rae N. Ridlon were crucial to the achievement of the result of this paper.

The preliminary work done by Richard Lally, Captain, U.S. Army and the above listed personnel, solved many technical problems, provided preliminary data, and guided the framework and physical parameters of this experiment.

The support and coordination efforts by Mr. Douglas Lier smoothed many paths, broadened my range of experiences at LANL, and allowed me to immediately become immersed in my experiment and research upon arrival (necessary for completion on time).

Finally, the advice, insights, suggestions for directions in the data analysis, patience, and cracking-of-the-whip-when-needed by Professors J. Neighbours and X. Maruyama were invaluable during all phases of this work: preparation, course work, performance of the experiment, the analysis, and the report. May their shadows never grow thinner.

## I. INTRODUCTION

Methods for sensing the parameters of a relativistic electron beam: position, current, and movement, have been sought since the invention of accelerators. The requirements for the measurement devices are that they must be non-intrusive, accurate, remotely monitored, free of self-noise, able to handle the high currents and broad bandwidths of the beam, simple to manufacture, and cost-effective. Several sensing methods are currently used. E-dot sensors, or resistive monitors, measure the return current present in the conductive walls of electron beam propagation pipes, and consist of a resistor imbedded in the walls. The resistor intercepts the return current, which is proportional to the time rate of change of the electric field at the probe. The E-dot output voltage signal is a measure of the beam electronic field [Ref. 1:p. 43]. Streak cameras use scanning optics to take photographs of an electron beam pulse that has passed through a scintillator to create a light image of the pulse [Ref 2:p. 1]. B-dot sensors indirectly measure the current of an electron beam by sensing the EMF induced through a wire loop by the derivative of the magnetic flux that results from an electron beam pulse [Ref. 3:p. 2471].

B-dot sensors have several advantages. They can accurately measure both transverse static beam displacement



(beam position) and small amplitude transverse beam oscillations over a frequency range of 1 GHz. E-dots contain ferrites whose responses vary with frequency; so that the E-dot signals are frequency dependent, an undesirable complication in signal analysis. Streak cameras are not as sensitive. Streak camera resolution is limited by the camera and film to 0.1mm in position and 5% in frequency, and streak cameras cannot measure beam current [Ref. 2:pp. 6-8]. B-dots can measure beam current, position, and small amplitude transverse beam oscillation simultaneously [Ref. 4:p. 2507].

An experiment was conducted at the Los Alamos National Laboratory to design and calibrate an improved B-dot sensor. This experiment was a portion of the development of the Dual Axis Radiographic Hydro-Test Facility (DARHT) project, which also employed the Relativistic Electron Experiment (REX) machine, a velvet cathode electron injector [Ref. 5:p. 1]. The improvement was necessary because previous B-dot designs contained undesirably large sensor port uncertainties (on the order of 8%), and had never been calibrated against an independent sensor. A major goal in the development of the DARHT and REX machines is to use the calibrated B-dot sensors to ensure that the electron beam generated by the injector is well-centered and free from small amplitude transverse beam oscillations [Ref. 5:p. 1].

There are several causes for undesired movement of an electron beam. These include variations in the beam

generation due to fluctuations in the pulse power source, positioning and focusing motion due to magnet errors, undesired modulation of the beam current intensity, and interactions of the beam with resonant dipole modes of the beam diode cavity. If the cavity resonant frequencies are matched to the high frequency components of the rise and fall of the beam pulse, transverse magnetic fields can occur which move the beam rigidly from side to side [Ref. 6:p. D-2]. (See Figures 1 and 2). These oscillations impair the coupling of an injector beam into the cavities of a linear accelerator. The coupling impairment and beam breakup instability may increase throughout the accelerating line until at the end of the final accelerating cavity, the beam spot size is so large that the beam is rendered useless [Ref. 4:p. 1]. Although there are ways to damp the oscillators in the accelerator cavities, it is important to ensure that the newly generated beam is as free of oscillations as possible in the injector. The magnitude of investments of research efforts and funds in the development of DARHT and other electron beam facilities underscores the importance of careful diagnostic beam sensor experiments, and motivates the development of a more accurate B-dot sensor.

The B-dot sensor experiment was carried out in two phases. The first phase, called the "preliminary B-dot experiment," was conducted in August and September 1989. Its purposes were to test the B-dot signal recording apparatus and software,

determine the REX electron beam pulse characteristics desired for the calibration experiment purposes, and to finalize requirements for the new B-dot design. The second phase, called the "calibration experiment," was performed in February-March in February 1990, to calibrate the new B-dot sensors and perform preliminary analysis of the B-dot signals. Both phases are described in this paper. The major results of the preliminary experiment included the validation of data recording apparatus and hardware, the determination of B-dot sensor port manufacturing requirements, determination of the electron beam pulse length required for statistically meaningful B-dot voltage signal analysis, and the selection of equipment and circuit devices that would be used in the calibration experiment. The calibration experiment determined the beam position resolution capability of the newly designed B-dot sensors using both ideal test stand conditions and REX electron beam pulses, identified and quantified sources of experimental error, and compared the B-dot sensor voltage waveforms with streak camera imaging data. Factors affecting the B-dot waveform were studied so that the signals could be better understood. Fourier analysis of the waveforms was conducted to correlate B-dot sensor indications of small amplitude beam oscillations to corresponding streak camera data and previously calculated REX diode TE/TM resonant modes. The calibration experiment determined that the static displacement (beam position) resolving capability of the B-

dot sensor designed at Los Alamos was 0.25 mm, and the sensor was able to accurately detect the frequency of transverse beam oscillations with amplitudes as small as 0.5 mm.

# Streak Camera Record of Emittance Mask

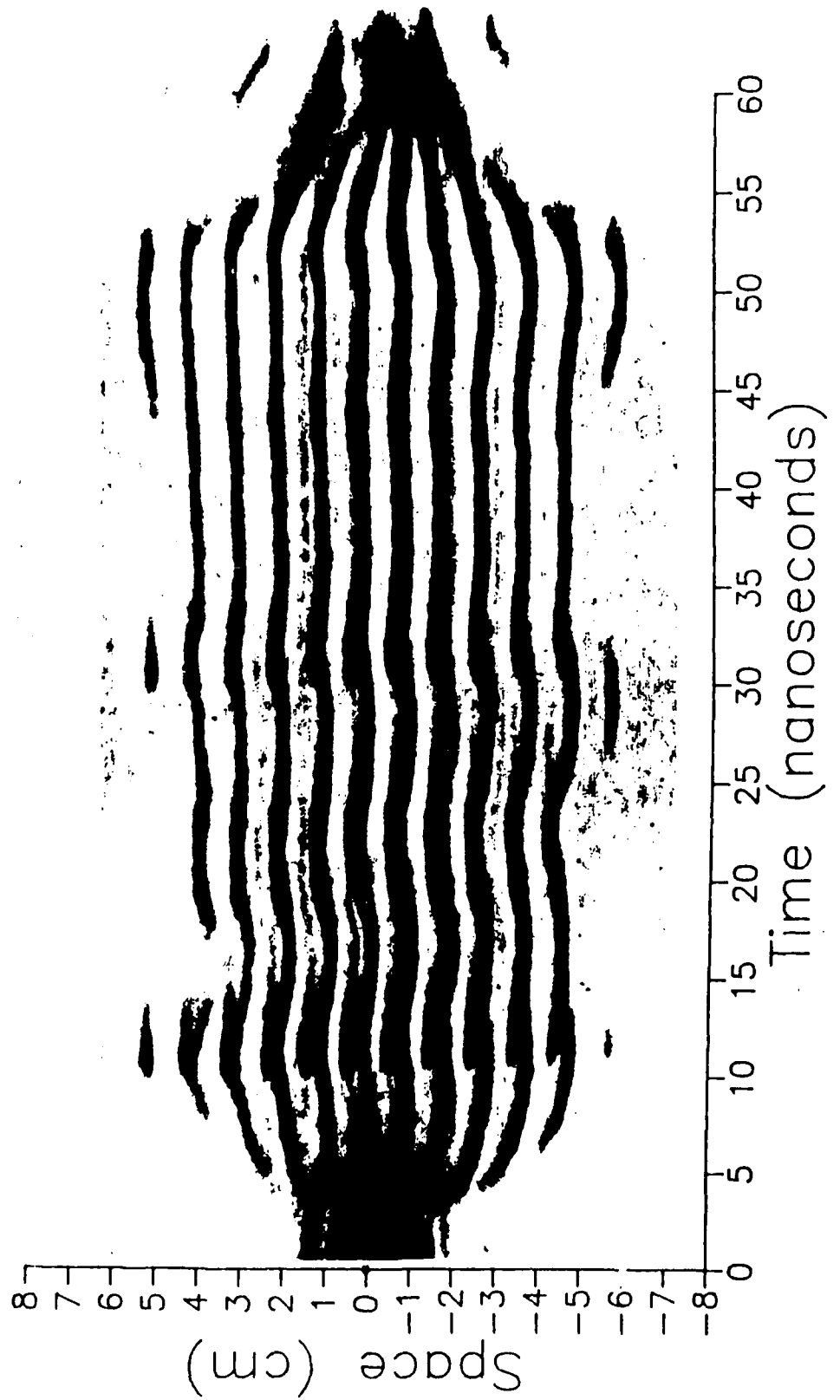


Figure 1. Streak camera photograph of electron beam with oscillations [Ref. 6:p. D-23]

# Streak Camera Record of Emittance Mask

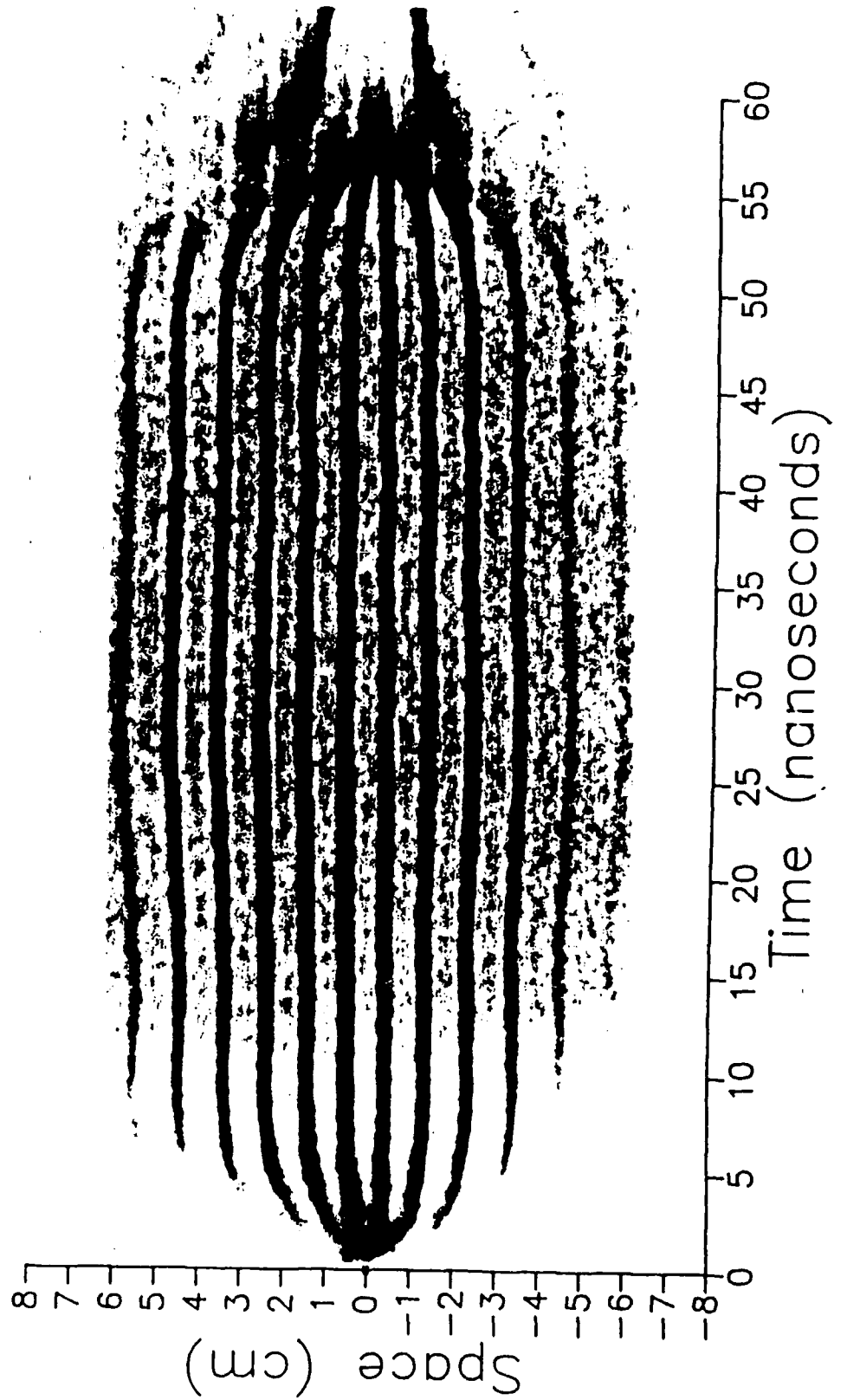


Figure 2. Streak camera photographs of electron beam without oscillations [Ref. 6:p. D-17]

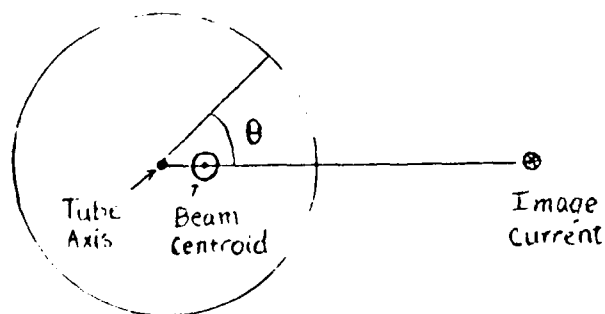
## II. THEORY OF B-DOT MEASUREMENTS

The B-dot sensor developed at Los Alamos consists of a set of four opposed wire loop sensor ports imbedded in an aluminum ring with flanges which may be bolted in the electron beam propagation piping. See Figure 3. The ring diameter is the same as that of the pipe, so that the electron beam pulse passes through the center of the B-dot ring.

The beam produces a magnetic field:  $B = \frac{\mu I}{2\pi R}$ , where  $\mu$  is the magnetic permeability of the surrounding medium,  $I$  is the electron beam current, and  $R$  is the radius of the propagation tube. The tube is made of metal, and is conductive. There is, therefore, a return current through the tube walls induced by the beam [Ref. 7:p. 1054]. The B-dot sensor does not directly exploit the return current, but it does modify the B field. The magnetic field at the tube wall is given by

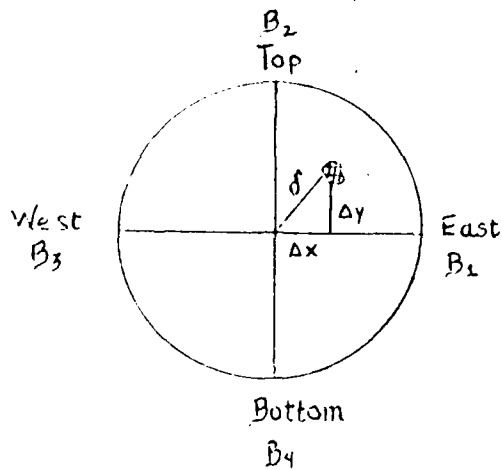
$$B = \frac{\mu I}{2\pi R} \frac{(1 - \rho^2)}{(1 + \rho - 2\rho \cos \theta)} \quad (1)$$

Drawing A



where  $\rho = \frac{\Delta R}{R}$ , the scaled displacement of the beam centroid from the ideal axis, and  $\theta =$  the angle at which the beam centroid is located relative to an arbitrarily chosen plane of reference. (A summary of the derivation of the magnetic field at the tube walls is given in Appendix A) [Ref. 8:pp. 1-4]. To first order, Equation 1 reduces to [Ref. 9:p. 1956]:

Drawing B



$$B_1 = \frac{\mu I}{2\pi R}(1 + 2\rho \cos \theta) \quad (2)$$

$$B_2 = \frac{\mu I}{2\pi R}(1 + 2\rho \sin \theta) \quad (3)$$

$$B_3 = \frac{\mu I}{2\pi R}(1 - 2\rho \cos \theta) \quad (4)$$

$$B_4 = \frac{\mu I}{2\pi R}(1 - 2\rho \sin \theta) \quad (5)$$

$$\delta = \sqrt{\Delta x^2 + \Delta y^2} \quad (6)$$

According to Faraday's Law, the voltage induced in a single turn wire loop of area A oriented perpendicular to the tube wall (as in B-dot sensor) is

$$V = \frac{-d}{dt}[BA]$$

It is seen from the geometry pictured in Drawing B that Probes 1 and 3 oppose each other in the x-direction, and Probes 2 and 4 oppose each other in the y-direction. These opposing pairs



may be summed or differenced, with the following results (derivations in detail are given in Appendix A):

Voltage difference in Probes 1 and 3:

$$\Delta V_x = -\frac{\mu A}{2\pi R} \left(\frac{4}{R}\right) \frac{d}{dt} [I\Delta X] \quad (7)$$

$$\sum V_x = -\frac{\mu A}{2\pi R} \frac{d}{dt} \quad (8)$$

Sum of Probes 1 and 3:

These two basic equations can be used to derive the following expressions:

$$I = -\frac{\pi R}{\mu A} \int \sum V_x dt \quad (9)$$

Static displacement of the beam centroid in the x-direction, given by the sum and difference of probes 1 and 3, with  $\epsilon$  = increase in voltage seen by the probe closest to the centroid:

$$I = -\frac{2\pi R}{4\mu A} \int (\sum V_x + \sum V_y) dt \quad (10)$$

$$\Delta X = \frac{R}{2} \left[ \frac{\int \Delta V_x dt}{\int \sum V_y dt} \right] = \frac{R}{2} \epsilon \quad (11)$$

Amplitude of oscillation of the beam centroid in the x-direction, given by the difference in probes 1 and 3 and  $\omega$ , the frequency of transverse oscillation of the moving beam; i.e., for this case, the beam is both off center and oscillating with single frequency:

$$\Delta X_0 = \frac{2\pi R^2}{4\mu A I \omega} [|\Delta V_x|] \quad (12)$$

Similar to Equation 12, but Equation 13 accounts for oscillation in both x and y planes:

$$\delta = \frac{2\pi R^2}{4\mu A I \omega} \left[ |\Delta V_x|^2 + |\Delta V_y|^2 \right]^{\frac{1}{2}} \quad (13)$$

These equations are used to analyze the B-dot signals. The B-dot signals are proportional to the time derivatives of the beam current pulse.

If the beam is located in the tube center axis and is not oscillating, a differenced signal will result in  $\Delta X = 0$ . If the beam is displaced from the center but not oscillating, the  $\Delta X$  (and  $\Delta Y$ , using the other two probes), displacement can be found by Equation 11.

The beam current can be found regardless of whether the beam is displaced, or centered, or oscillating or not, by Equations 9 or 10. Note that Equations 9 and 10 require the summed voltage signals to be integrated. This can be done passively, using ANZAC or MCL voltage adder/dividers and a locally manufactured integrator, or digitally, using Tektronix software "sum waveform" and "integrate waveform" options. If the beam is oscillating in a sinusoidal fashion, Equations 12 and 13 calculate these effects.

In this experiment, pulse waveforms sensed by the B-dots are transmitted through solid shielded 50 ohm Heliac Superflex cables to the control room, where they are terminated in 1 GHz bandwidth Tektronix R7103 Oscilloscopes. The oscilloscope screens are viewed by Tektronix DCS C1002 video cameras, which digitize the waveforms pictured and send them to the IBM PC

AT computers, which contain the Tektronix "DCS" signals analysis and storage software. A B-dot sensor ring with eight probe ports: four opposed 50 ohm resistor ports, and four opposed plain wire ports, is shown in Figure 3. A detailed drawing for the B-dot sensor is given in Appendix D.

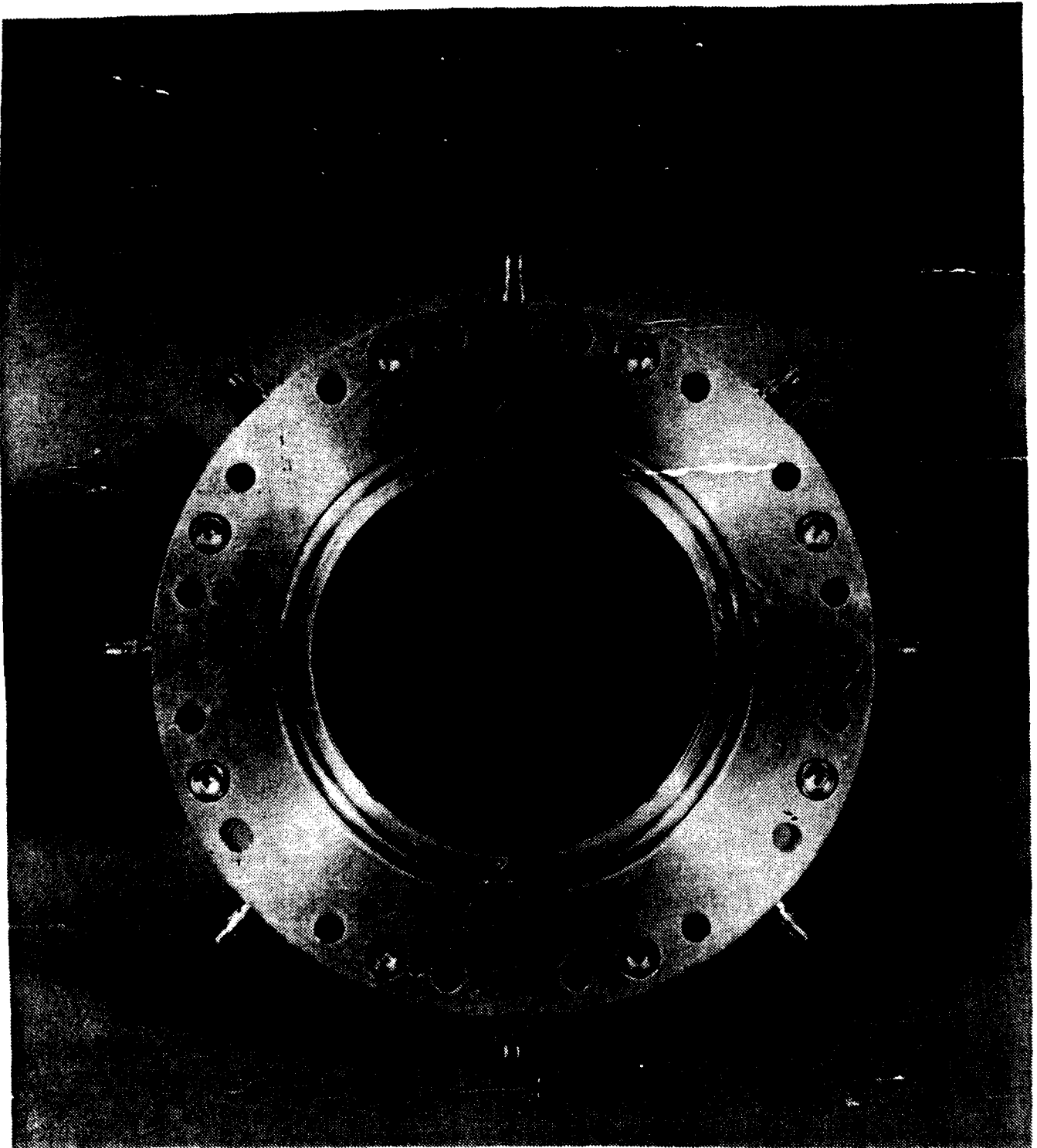


Figure 3(a). Aluminum B-dot ring (ABR2) front view  
(photo by Mark Martinez)

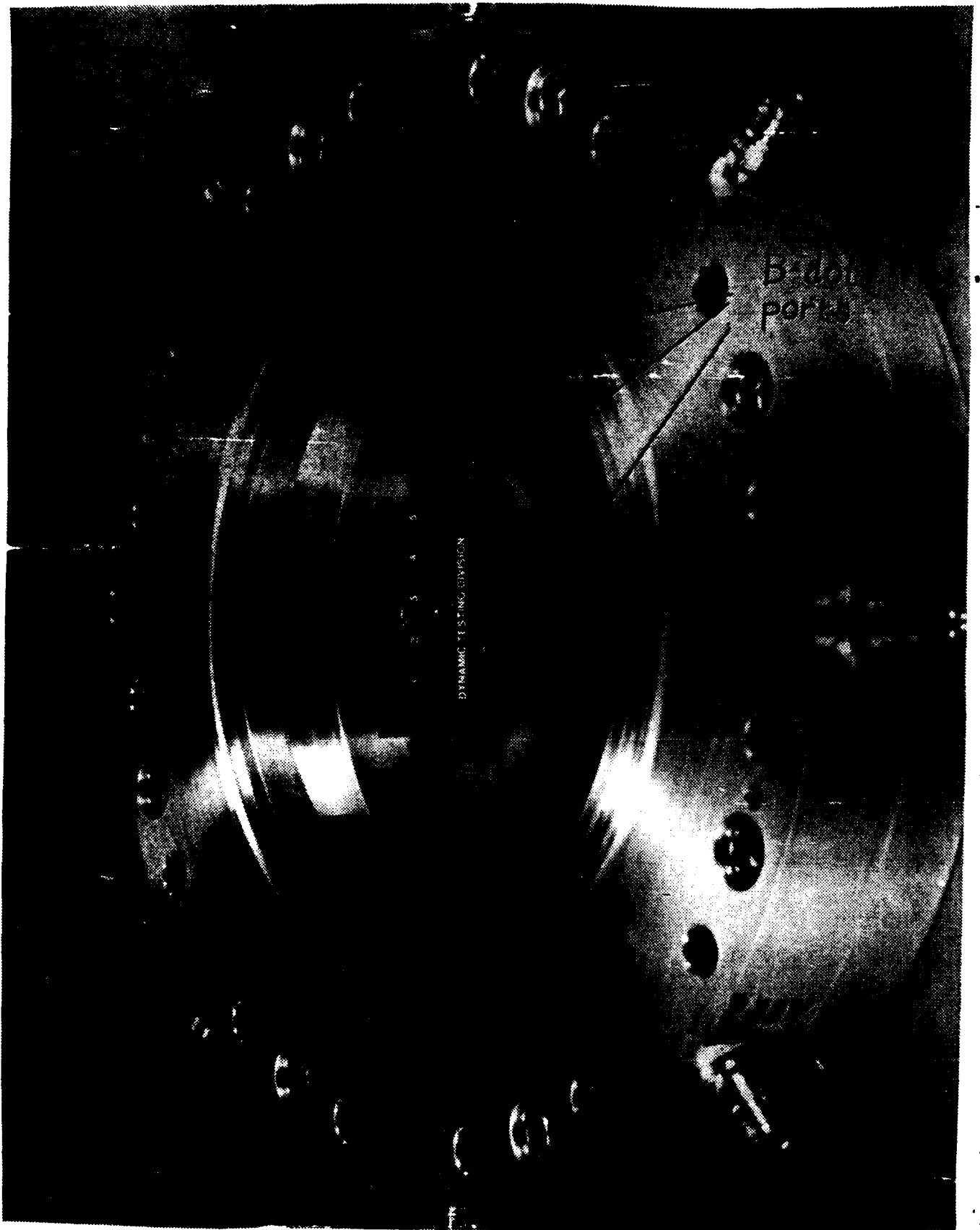


Figure 3(b). Aluminum B-dot ring (ABR2) angled front view  
(photo by Mark Martinez)

### III. DESCRIPTION OF RELATIVISTIC ELECTRON EXPERIMENT (REX)

In order to clearly picture the sensor diagnostic procedure and place diagnostic dynamics in context, a short description of the REX assembly is presented here. (More complete details are given in Appendices B through D). See Figures 4(a) and (b). The Marx generator is the power source for the REX 4MV, 4kA, 35kA/cm<sup>2</sup> rad<sup>2</sup> brightness, 15ns rise/fall time, 80ns duration electron beam pulse. It contains a high voltage power supply and 62½ capacitive stages that are charged in parallel and discharged in series. (The generator is capable of delivering a 6.2 MV pulse to the pulse forming line, but this pulse magnitude is not required for REX). The Marx output stage is connected by a 10 μH copper inductor to the water-dielectric section of the Pulse Forming Line (PFL, see Figure 5). When a pulse enters the water PFL, it becomes charged until the break-down voltage of its output switch is reached (2.5 MV). The pulse leading edge is peaked with a peaking dome within the PFL. The pulse energy then enters the glycol-dielectric line (GLY1), via the first of two LC filters (F1), which produces a pulse of longer duration than the PFL pulse. It then exits the GLY1 via the second LF filter (F2) which maintains the peaked leading edge of the pulse. The pulse then enters the second dielectric (oil) line (OL2). OL2 steps up the pulse voltage by a factor of 1.47 and is

terminated in a radial liquid resistor. Then energy of the pulse flows out radially along equipotential lines via this resistor and is stepped up by another factor of 1.48 before it is made available to the cathode stalk on the vacuum side of the resistor diaphragm. The cathode stalk supports the 2.5 inch diameter velvet field emission cathode. The peak field on the cathode surface is 30 kV/cm. A stream of electrons is released by the cathode [Ref. 10:p. 5] (See Figure 6). (Example calculation: for a +35kV, -35kV Marx charge, 2 x (35kV charge) x (0.58 gain,PFL) x (0.73 gain,GLY1) x (1.4 gain,OL2) x (1.48 gain,output) = 4MV anode-to-cathode. Then, (80ns,FWHM) x (4MV) x (4kA current) = 1.3kJ beam energy). The electrons are accelerated toward the anode, which has an open 3 inch diameter central channel to permit a large portion of the electron beam to continue through to the extraction solenoidal magnet area. The magnet focuses the electrons 91 cm from the cathode into a beam approximately 2 cm in diameter. The beam is allowed to exit the focussing magnet via a gate valve into a cylindrical pipe housing the B-dot sensory rings, the Lambertson steering magnets, streak camera emission mask and a scintillator "can" (see Figure 7). The "can" is terminated by a glass or quartz beam stop. Streak camera photographs are obtained by observing the beam through the beam stop with a series of mirrors and a telescope and camera located outside a "window" in the REX cement block radiation shielding [Ref. 1:pp. 1-18].

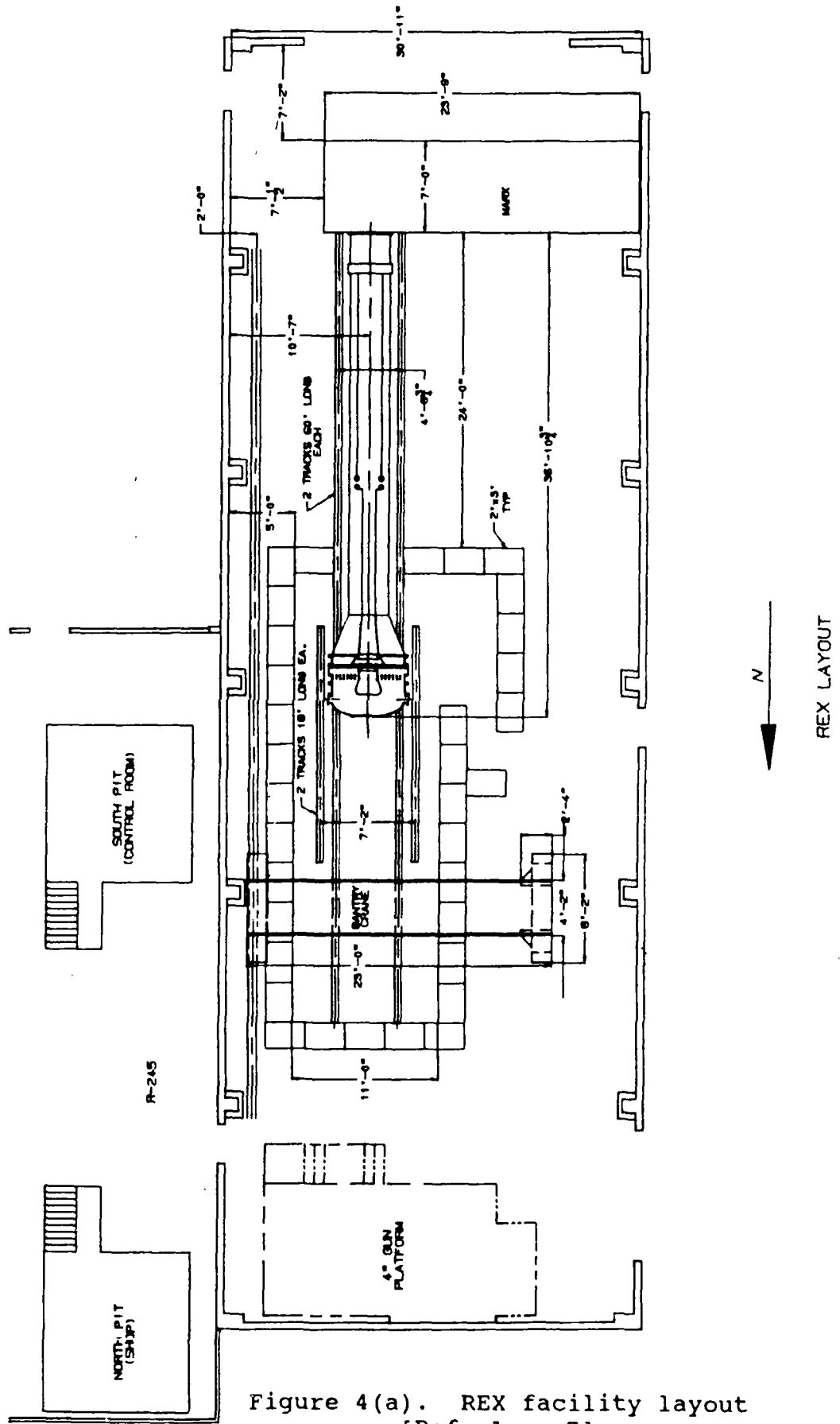


Figure 4(a). REX facility layout  
[Ref. 1:p. 7]



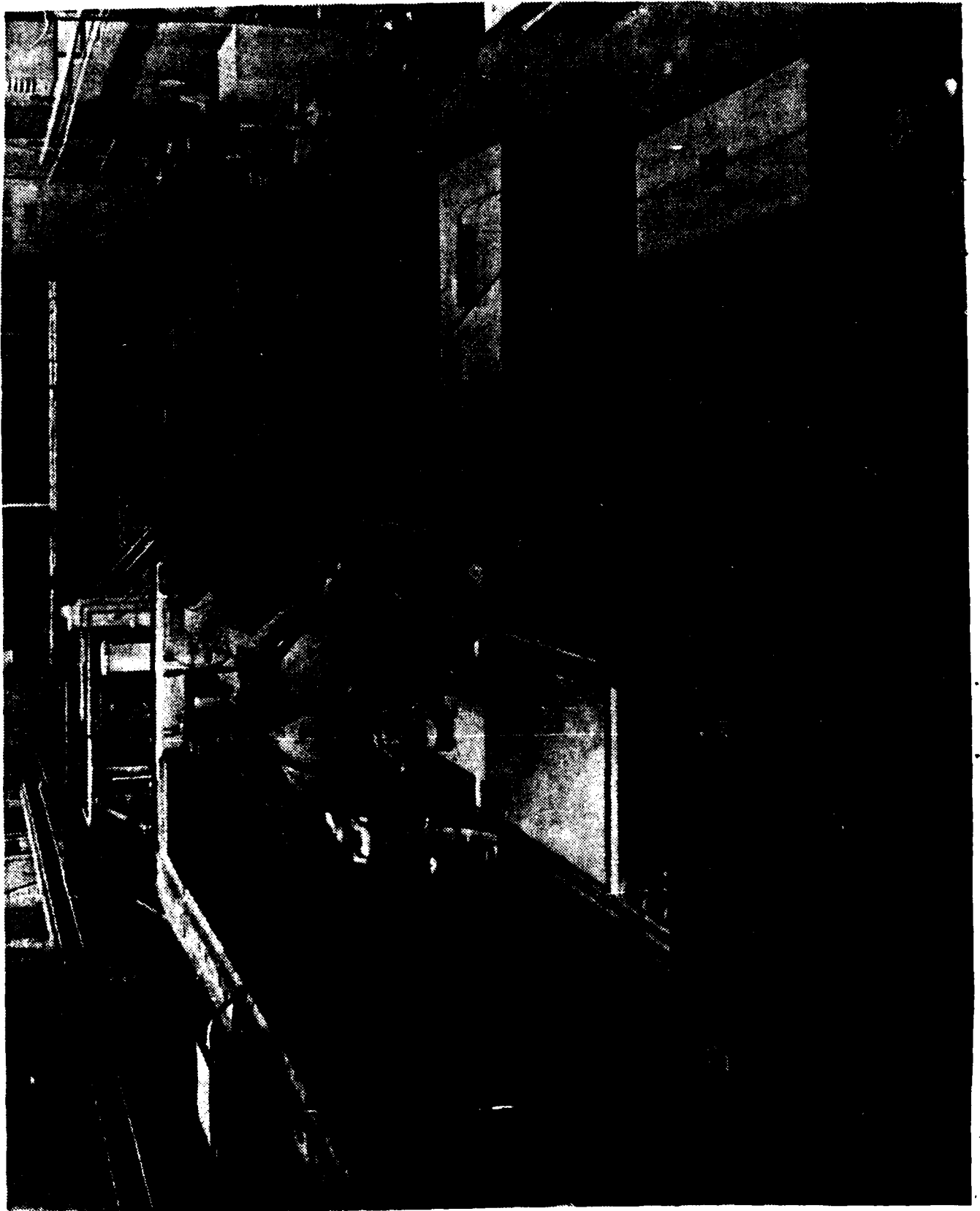


Figure 4(b). Photograph of REX  
(photo by Mark Martinez)

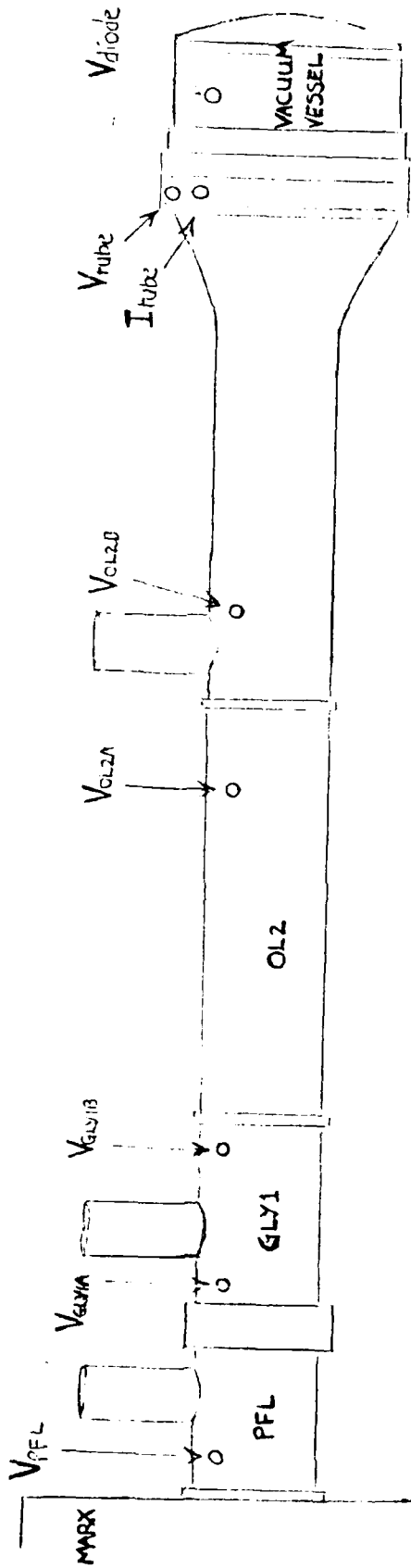


Figure 5. REX pulse power system

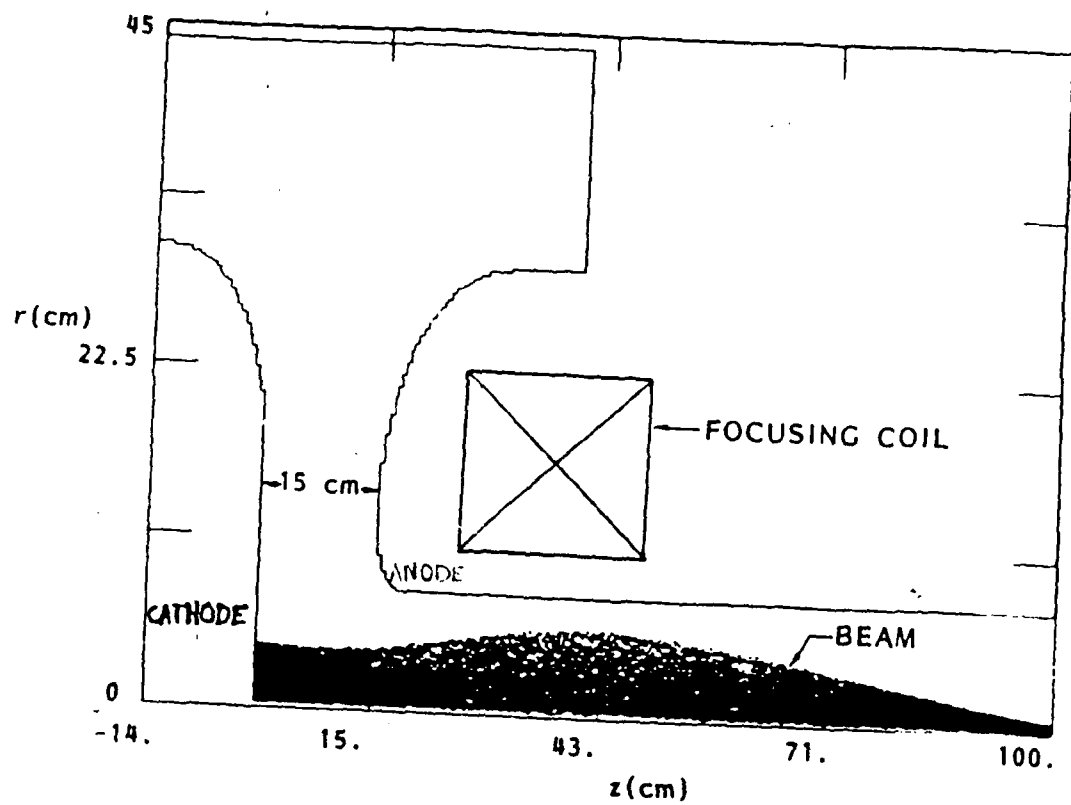


Figure 6. ISIS Model: Emission of electron beam base from cathode [Ref. 10:p. 5]

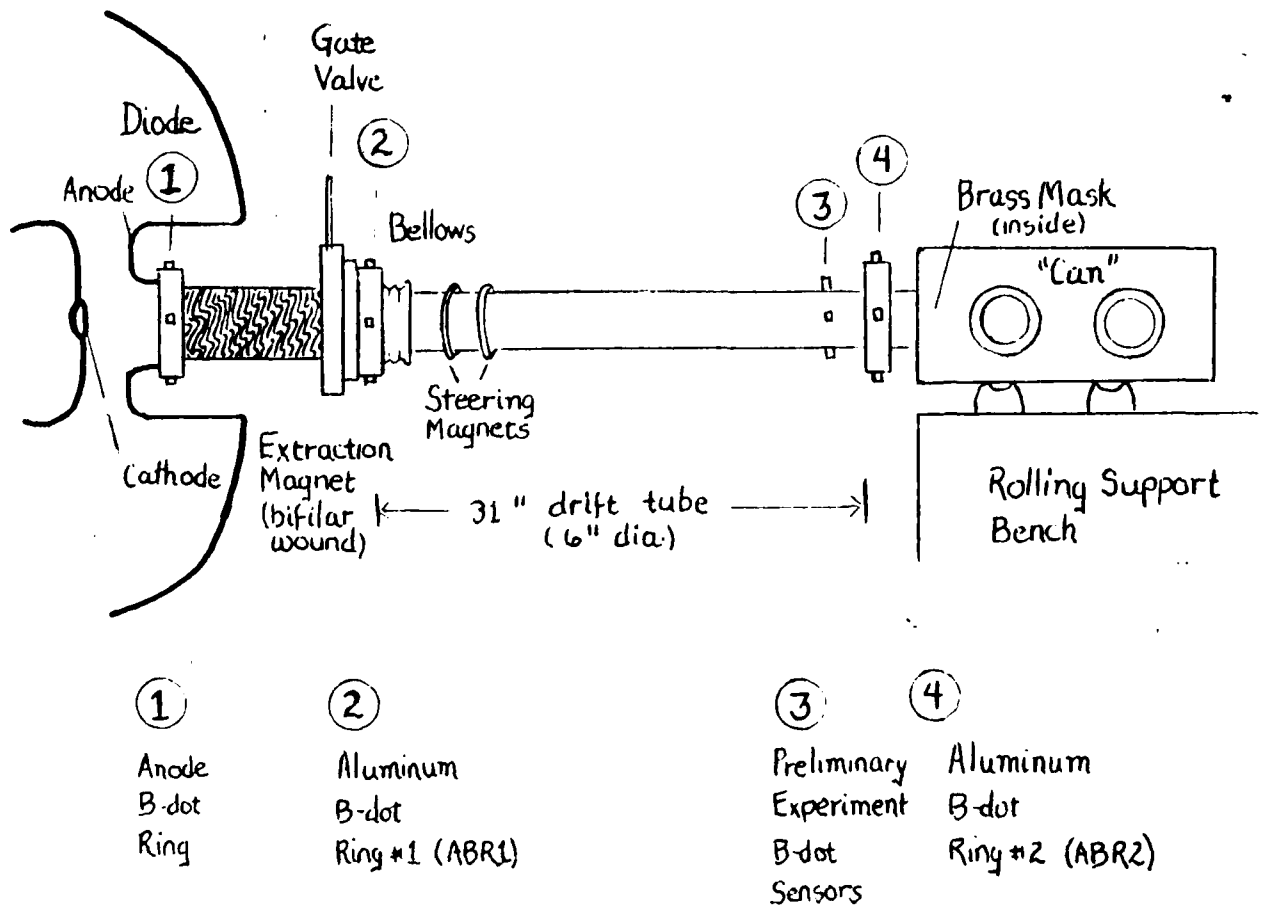


Figure 7(a). Diagram of REX front end

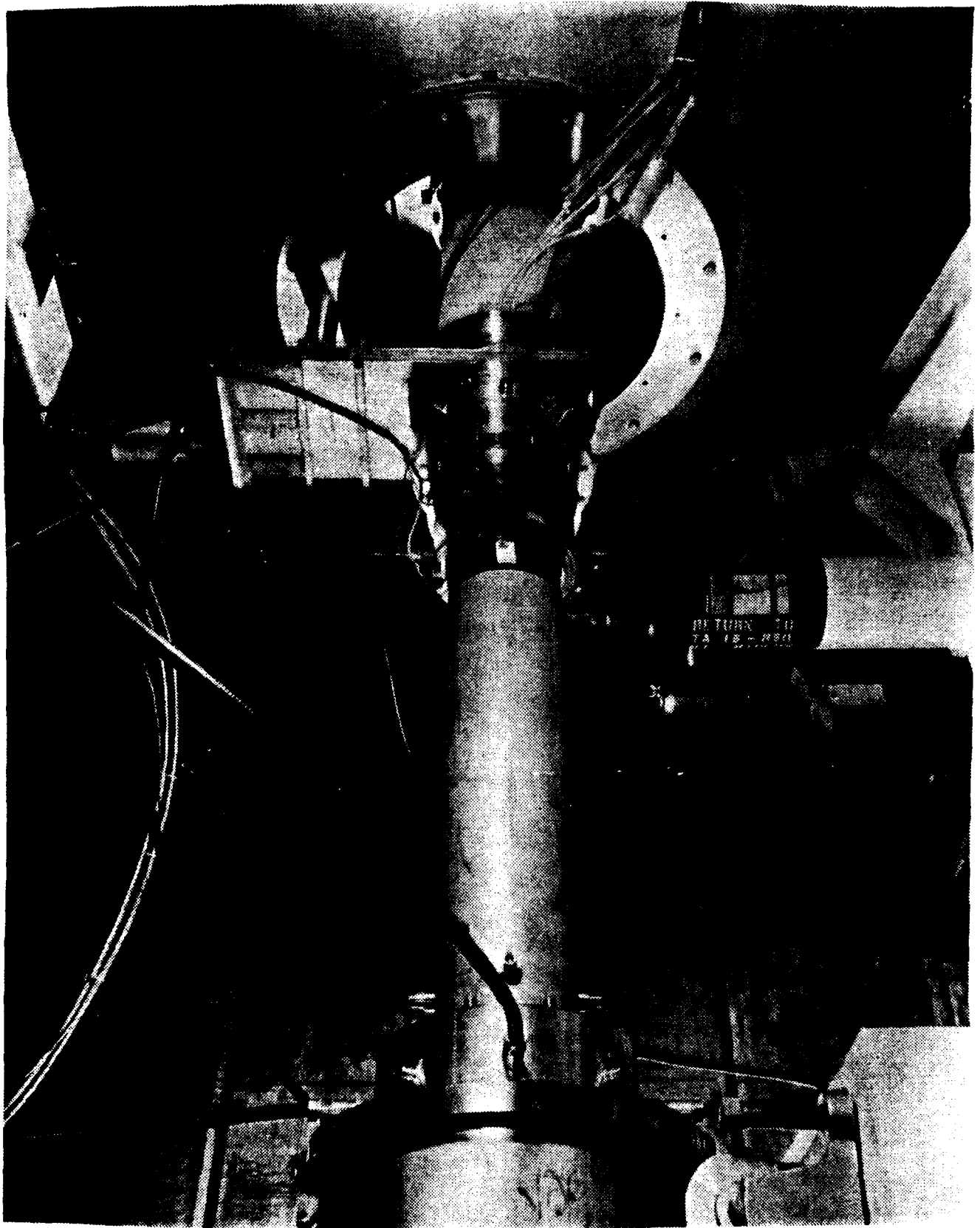


Figure 7(b). Experiment front end  
(photo by Mark Martinez)

## IV. EXPERIMENTS

### A. EXPERIMENTAL GOALS: PRELIMINARY EXPERIMENT

Before a detailed B-dot measurement experiment could be conducted, several questions had to be explored. The preliminary experiment was conducted in the summer of 1989. A 60-70ns pulse with 10-15ns rise/fall times, a simple solenoidal magnet, and a four-sensor port zero resistance B-dot ring with wire loops protruding into the beam propagation cavity (see Figures 8 and 9) were used to determine: a) how well the Tektronix data analysis software interfaced with the Tektronix C1002 digitizing camera and R7103 Oscilloscope; b) the accuracy of the B-dot measurements made on a test stand (see Figure 10); c) what machining and manufacturing accuracy were necessary in the design of a B-dot sensor; d) how long the electron pulse should be in order to gather statistically meaningful information about beam movement; e) what factors were affecting the pulse waveform shape; and f) whether it was better to digitally sum and subtract individual B-dot readings, or to use passive resistive or inductive adders/dividers. The conclusions and data were continually compared and used during the calibration experiment.

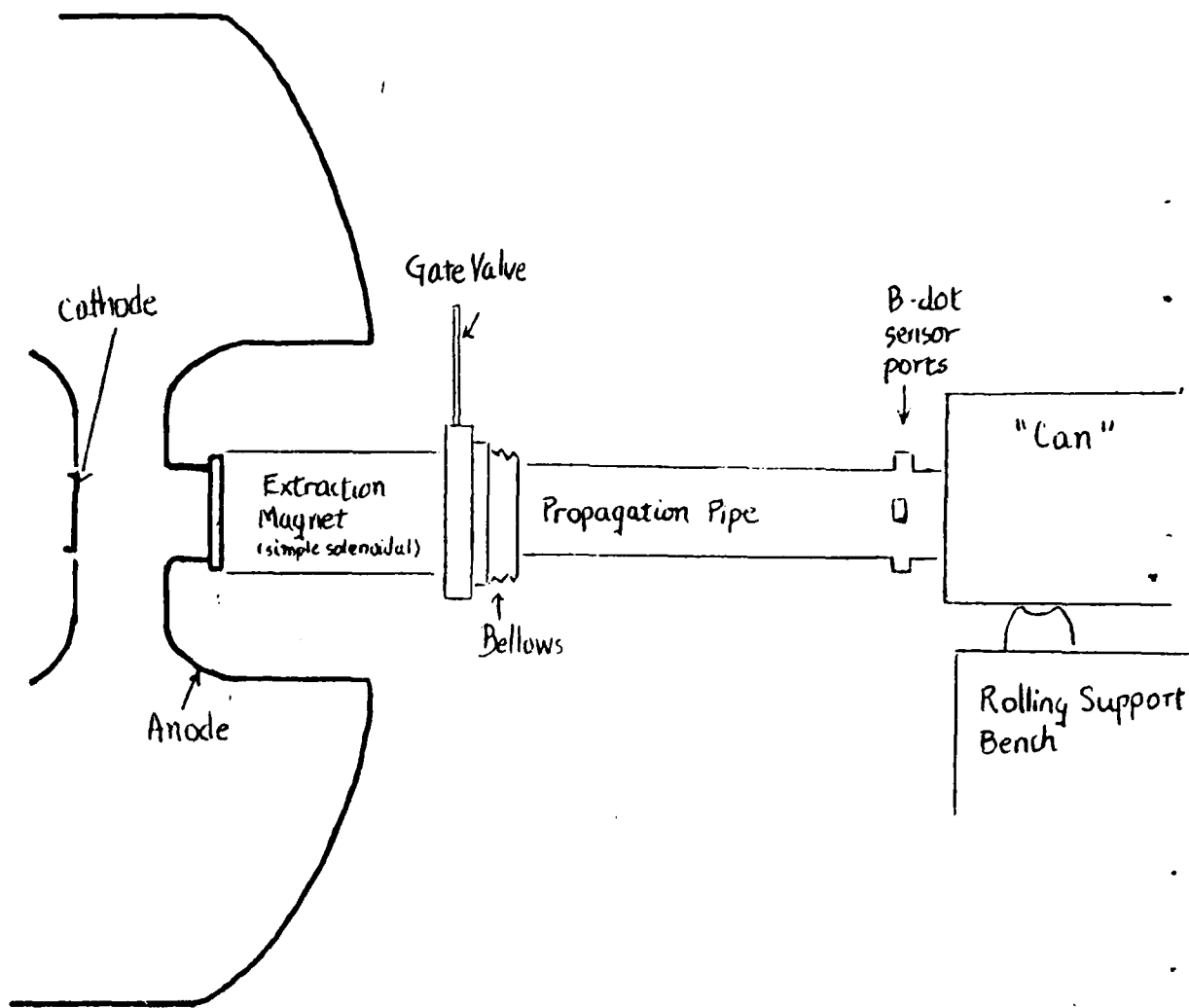


Figure 8. Preliminary experiment

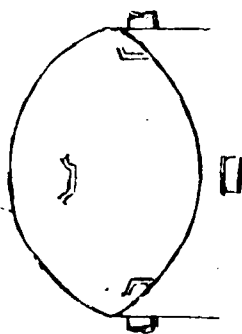


Figure 9. Drift tube B-dot ring

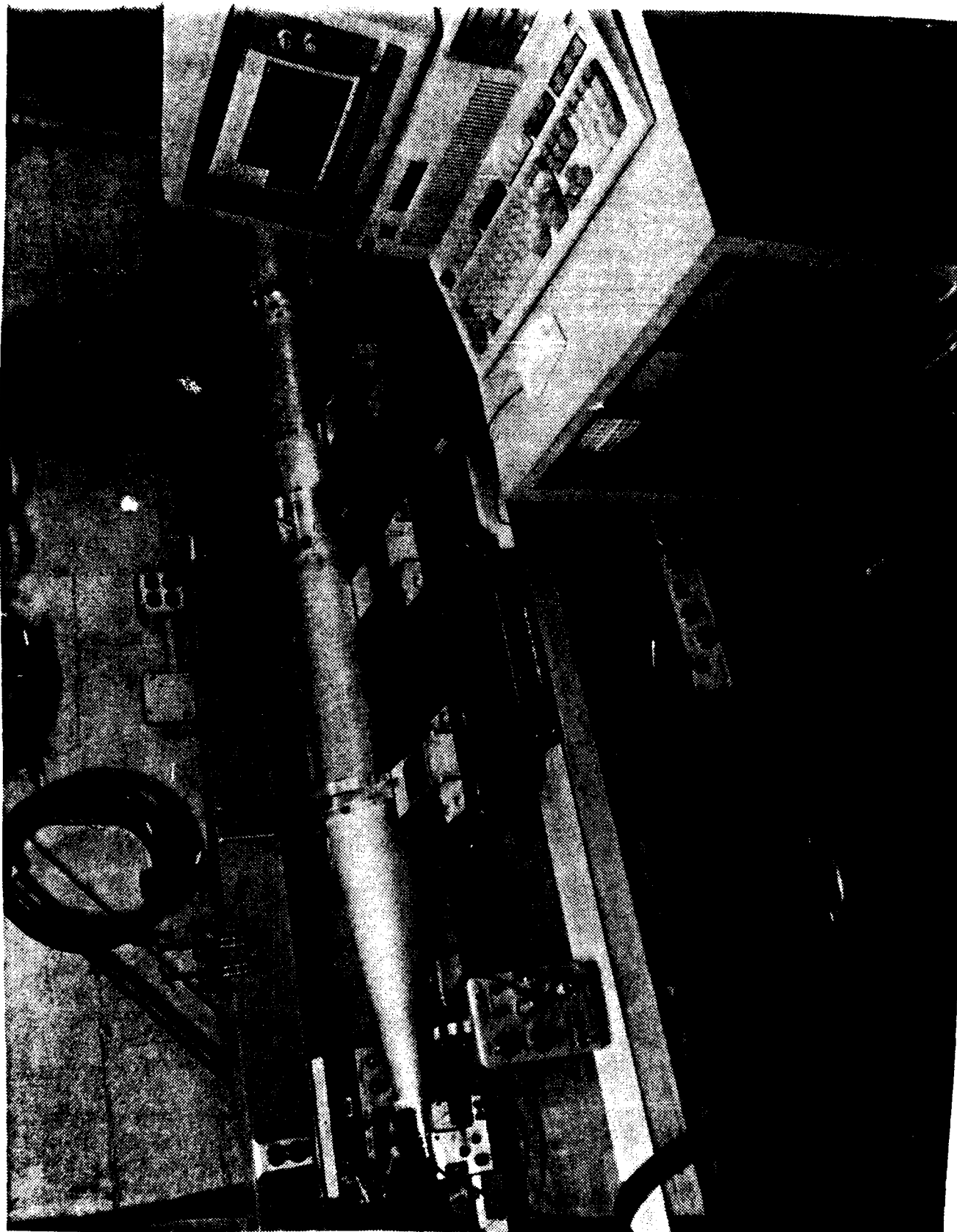


Figure 10. Test stand  
(photo by Mark Martinez)



## B. PRELIMINARY EXPERIMENT AND CONCLUSIONS

The experiment was conducted by the M-4 Hydrodynamics Group and CPT Richard Lally, Naval Postgraduate School student, in August-September 1989. The major equipment used included:

1. AST Premium/286 PC with IBM monitor
2. Tektronix R7103 Oscilloscopes with 7A29 amplifiers and 7B15 time base (~5 -10% error, rough calibration, comparing known signals from one O-scope to another)
3. Tektronix C1002 video cameras, not calibrated with a known waveform (20-30% error, largest error source)
4. B-dot sensor ring (port-to-port difference 5-8%)
5. Two ANZAC H-9 2-2000 MHz adder/dividers, 40 ft. lengths of Heliac, Superflex coaxial cable, various connectors (negligible errors assumed)

The equipment was arranged as follows: The REX machine, solenoidal magnet, and a "drift tube" housing the B-dot ring were located in the shielded experimental area, as shown in Figure 8. The coaxial cables, one for each of four opposed-pair B-dot ports, led from the B-dot ring back to the control room, where they were connected to attenuators and oscilloscope input ports, or to the ANZAC adder/dividers and then to the oscilloscopes, for summed or differenced signals. The DCS cameras, one for each oscilloscope, digitized the waveforms on the oscilloscope screens for the AST 96 PC computer with Tektronix Digitizing Camera System (DCS)

software (version 2.05). The resulting signal waveforms were stored on the computer hard drive and on floppy disks.

The results of this experiment will be discussed in the order that the topics of investigation were set forth at the beginning of this section.

Numerous difficulties in the interfaces between the oscilloscope and the camera, and between the camera and the Tektronix software were encountered. When a new version of the DCS software was installed (version 2.06), the interface problems were eliminated.

The issue of test stand B-dot accuracy was explored to determine which factors could result in correctable errors, and which factors would result in remaining finite errors. The B-dot ring (see Figure 9) contained a number of machining and manufacturing specifications which were difficult to exactly duplicate on each of the four ports. The largest manufacturing port-to-port difference was probably the wire loop area. The rectangle shape enclosed by the wire loops differed visibly from port to port and when the B-dot ring was entered as closely as possible on the test stand (Figure 10), the ports' signals differed in magnitude by 5-8 percent (see Figure 11). The follow-on design was to reduce this error. A Tektronix DCS software camera-to-oscilloscope calibration procedure was attempted, but failed to be successful on the

centered teststand B-dots, with large port-to-port variation

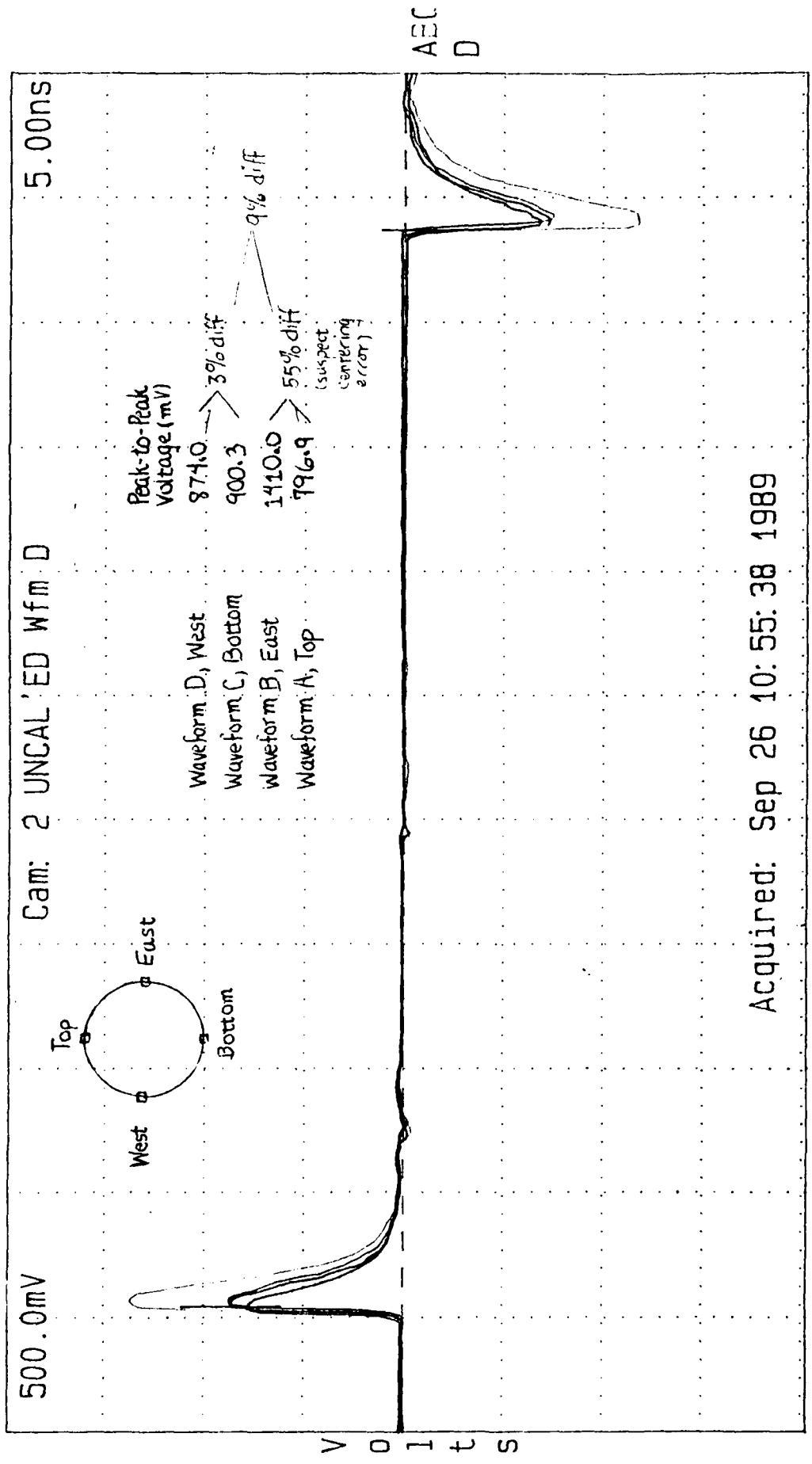


Figure 11. Centered test stand B-dots with large port-to-port variation

then current version 2.05. (Since version 2.06 was forthcoming, it was decided that camera-to-oscilloscope calibration would be performed at a later time. The result is that the voltage magnitudes and periodicities of the recorded waveforms for the preliminary experiment were in error to 20-30 percent.) The ability of the B-dot ring and software to sense position differences was explored in a general manner: the B-dot ring was shifted so that the test stand center conductor came progressively (0.3 cm, then 0.6 cm, then 1.3 cm) closer to one port. The result was that the port's waveform increased in magnitude by 8.8 percent, then 12.2 percent, then 26 percent. (See Figures 12(a) and (b)). These data represent a linear increase in magnitude with displacement, as predicted by Equation 11,

$$\Delta X = \frac{R}{2} \epsilon$$

where  $\Delta X$  = displacement,  $R$  = radius of the test stand, and  $\epsilon$  is the increment in voltage seen due to the displacement; assuming no errors due to cables or connectors, no subtraction error, and no test stand noise. (When the calibration experiment was performed, this formula was tested again, and an assessment of errors due to cables/connectors, subtraction errors (both digitally, using Tektronix DSC software operation called "subtract two waveforms," and passively, using ANZAC or other adder/dividers) as made). The test stand oscilloscope left and right amplifier modules varied between

12.1% increase in East port magnitude, mvmt = 0.6 cm

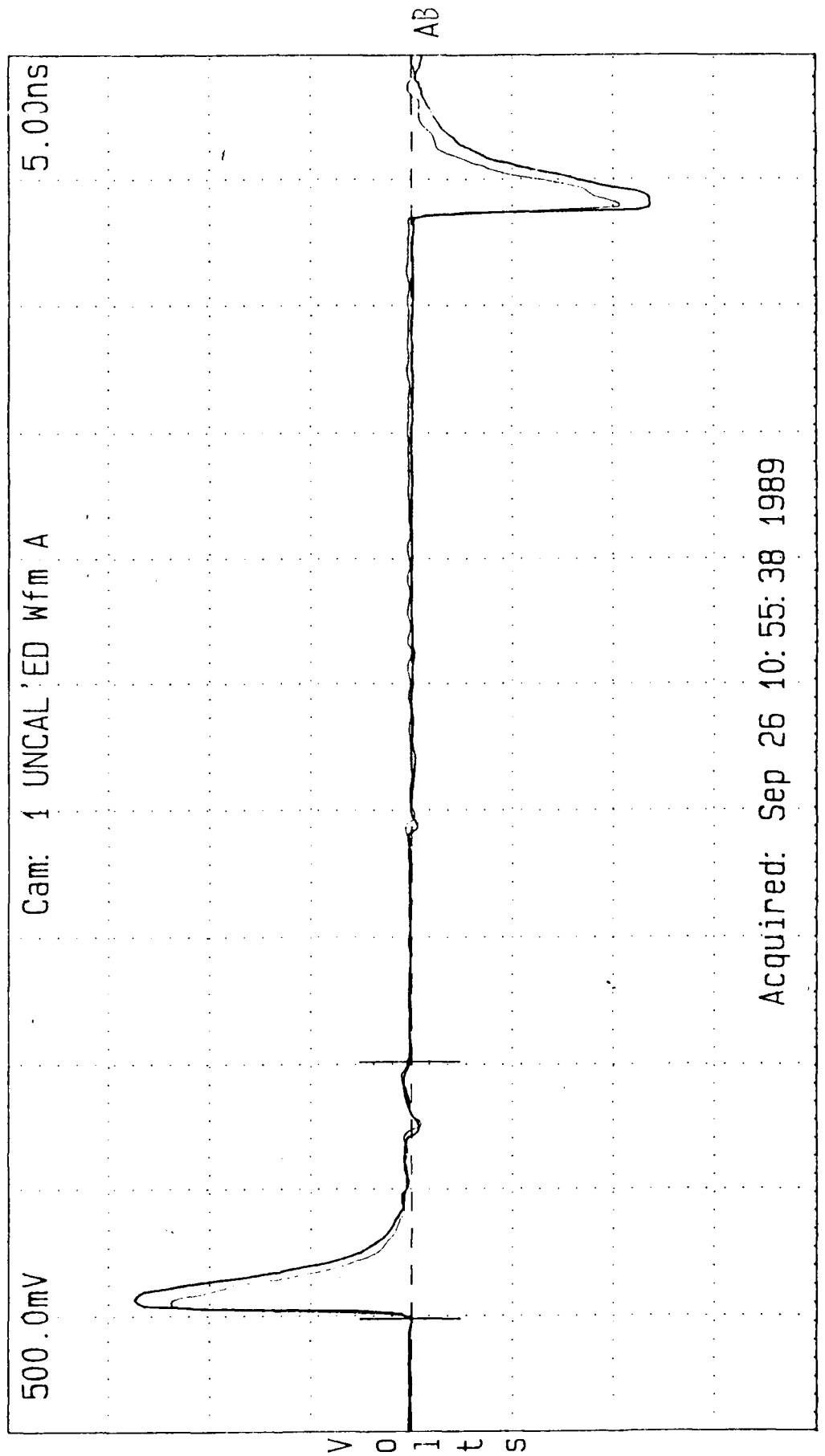


Figure 12(a). 12.1% increase in East port magnitude, mvmt = 0.6 cm

V1: 7.29mV T1: 4.46ns seconds • DV: 1.04mV, DT: 10.2ns

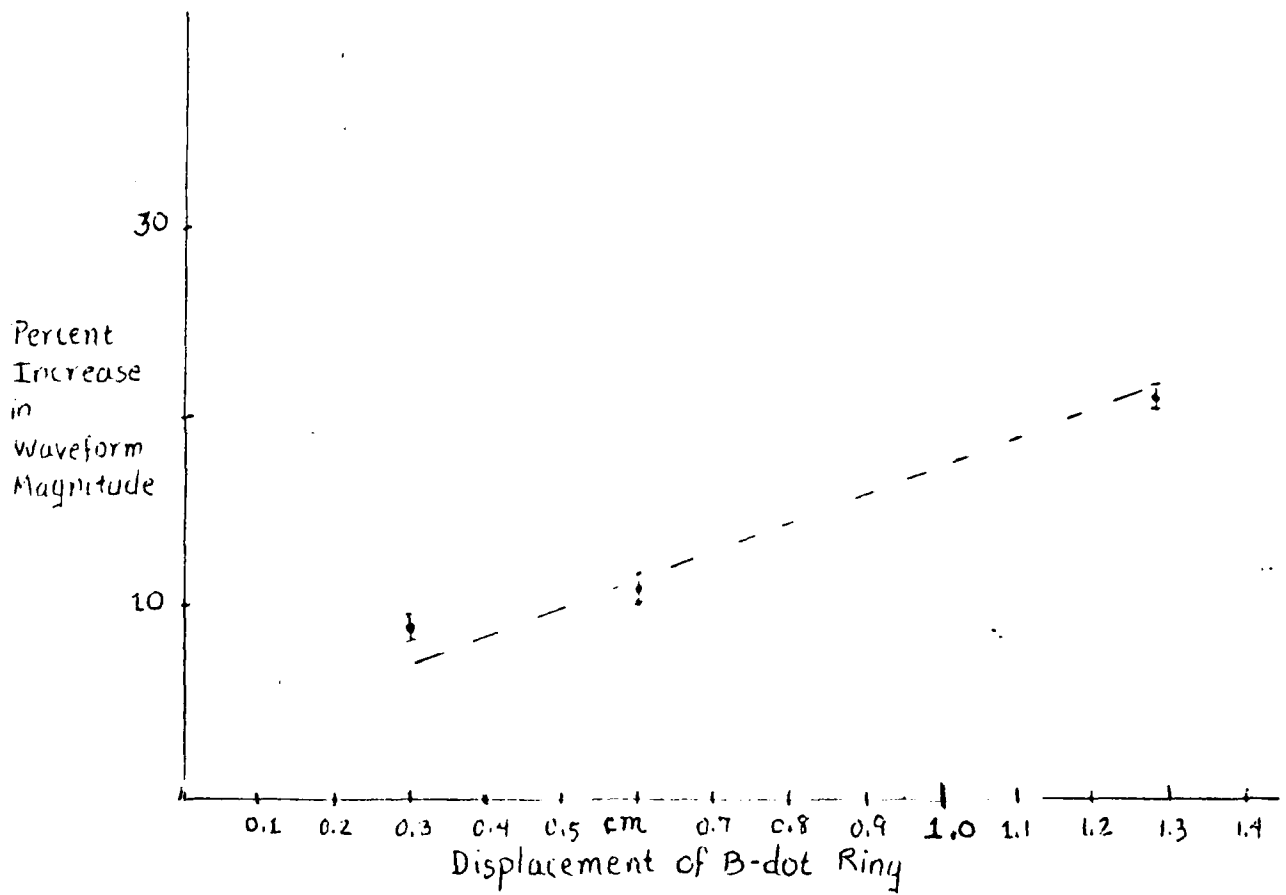


Figure 12(b). Linear increase in waveform magnitude with displacement

5 and 10 percent of each other, given the same input signal; for the preliminary experiment, this was satisfactory. For the next experiment, calibration and monitoring goals were to reduce all individual sources of test stand error to the order to 1 percent each.

The manufacturing and machining precision on the original B-dot ring was not crucial, but for the calibration experiment, it was deemed critical to redesign the following portions: the B-dot ports resulted in different shape waveforms if shorter or longer pulse rise times are used. (See Figure 13). The distortion that results for the very short (less than one nanosecond) rise time is unacceptable for B-dot sensors in their use in other machines (such as PHERMEX, for which the new design was also to apply) [Ref. 3:p. 1]. This distortion is eliminated if the port incorporates a 50 ohm precision resistor. This resistor effectively damps out the self-resonance of the natural inductance and stray capacitance of the wire B-dot. However, the passive adder/dividers do not respond well when driven by the 50 ohm B-dot ports. The ANZAC passive devices introduce a 5 percent "artificial droop" effect, which was not present when they were driven by B-dot ports with plain wires. MCL devices do not do this, but their inputs must be reduced by attenuators from MV levels to less than 250V.

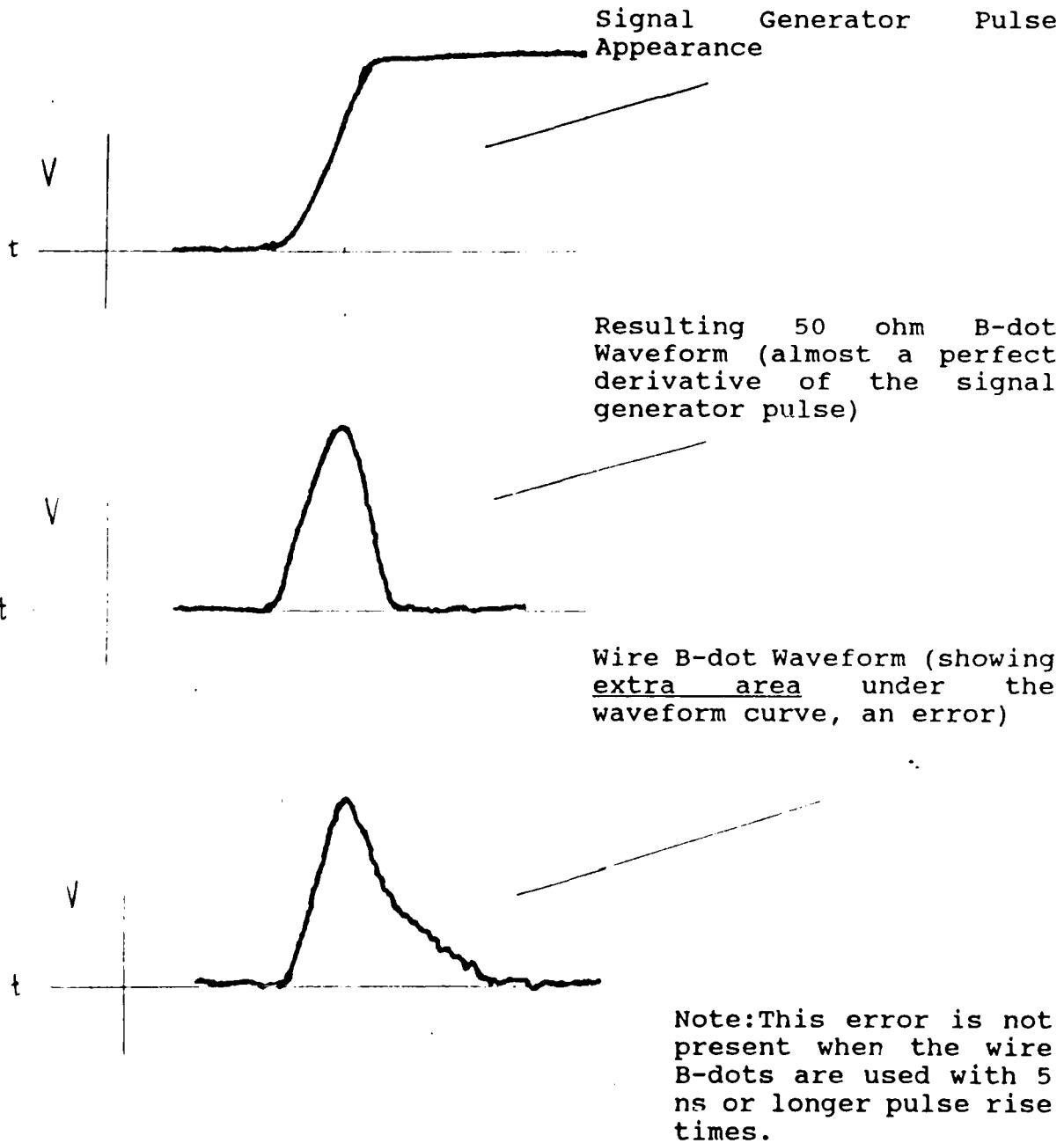


Figure 13. B-dot wire sensor vs B-dot 50 ohm sensor performance for short pulses (~1 ns rise time)



The wire loop configuration was redesigned to be much more uniform: the wires were supported by a precision made ring with an individual pin tab and pin for each port (see Figure 14). The theoretical loop area that was to result was a combination of a machined base surface, a ring pin tab, and a pin. These parts would be individually manufactured to be identical, then carefully placed by hand into the aluminum (lighter in weight than the original stainless steel) B-dot ring base. The precision and effectiveness of this design would be tested on the test stand.

The preliminary experiment showed that the pulse length of 50ns was too short. In a typical differenced signal, for instance, the center portion, which contains important beam movement information, was not of sufficient duration to allow a statistically meaningful Fast Fourier analysis to be performed (see Figure 15). For the calibration experiment, the pulse length was increased to approximately 100 ns. With this length, a center portion of ~60 ns duration was available between the rise and the fall of the pulse.

The preliminary experiment focusing magnet was a simple solenoidal magnet that had been "borrowed" from another experiment. Some inconsistencies in the manner in which it guided the electron beam were apparent when the B-dot waveforms for ideally centered (B-dot ring not offset in any direction) were examined. For one REX pulse on 27 September, the strongest signal was seen by the East port (1.49v peak-

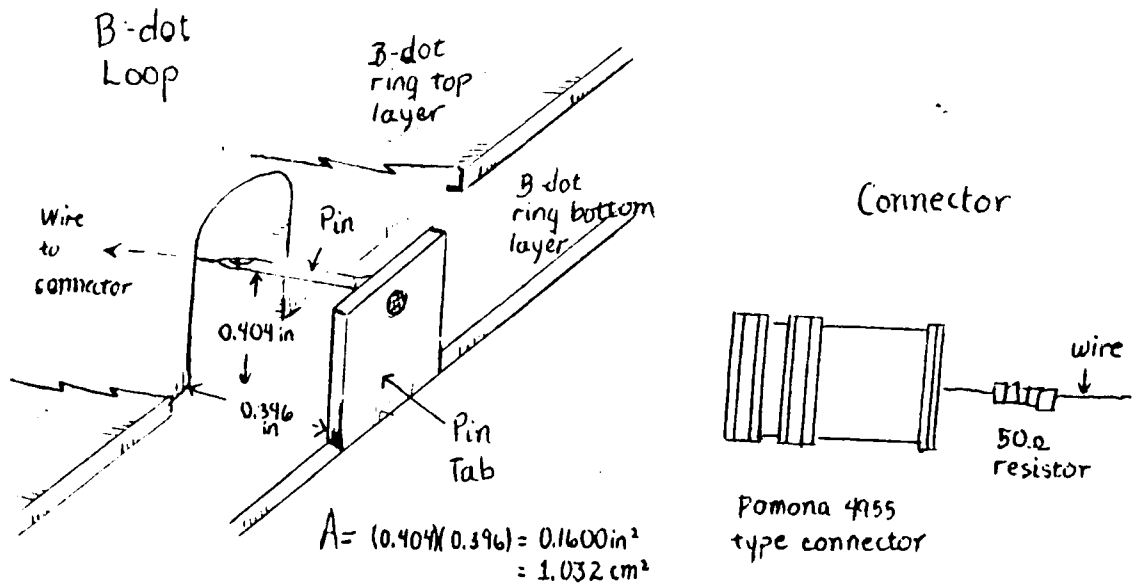
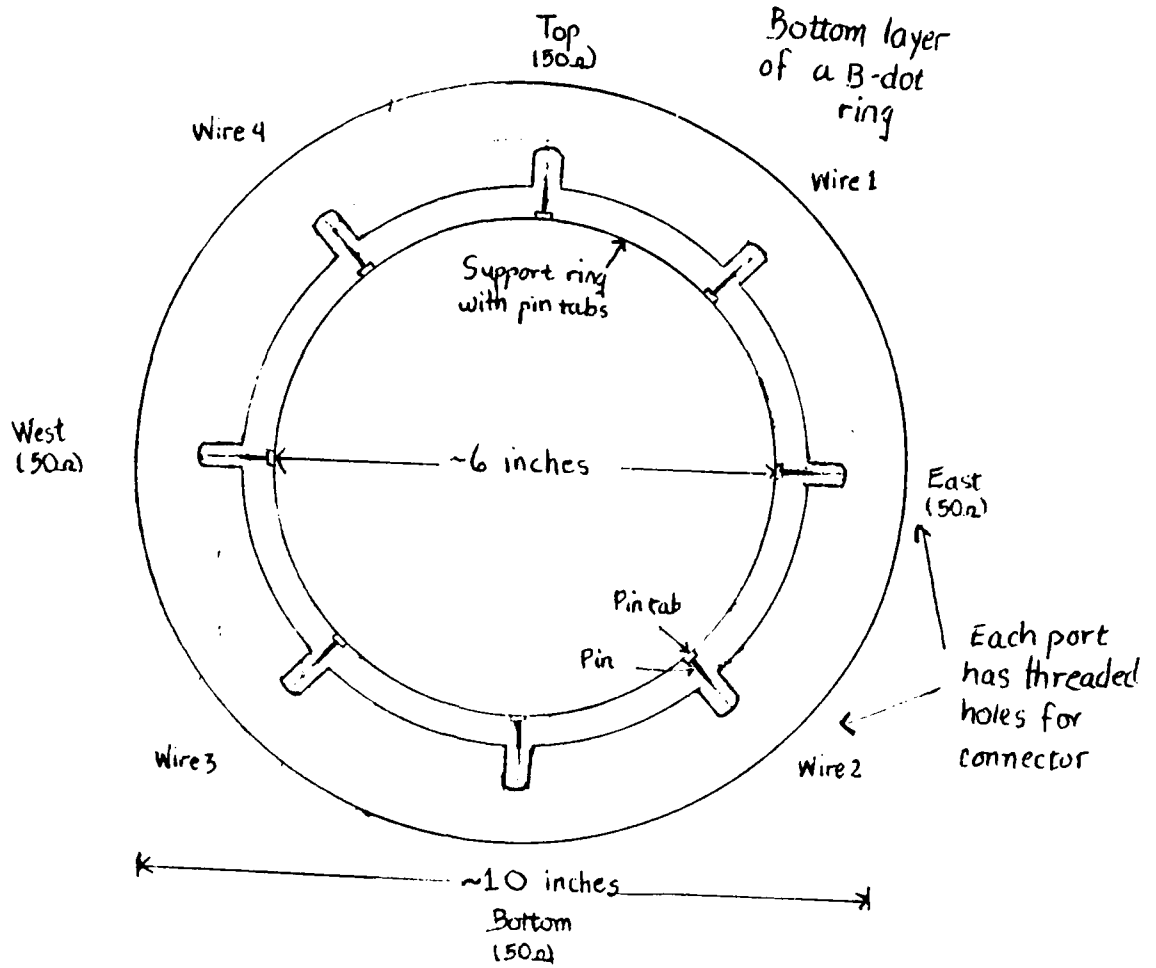


Figure 14. New aluminum B-dot ring design

E-W subtracted signal, insufficient center portion length

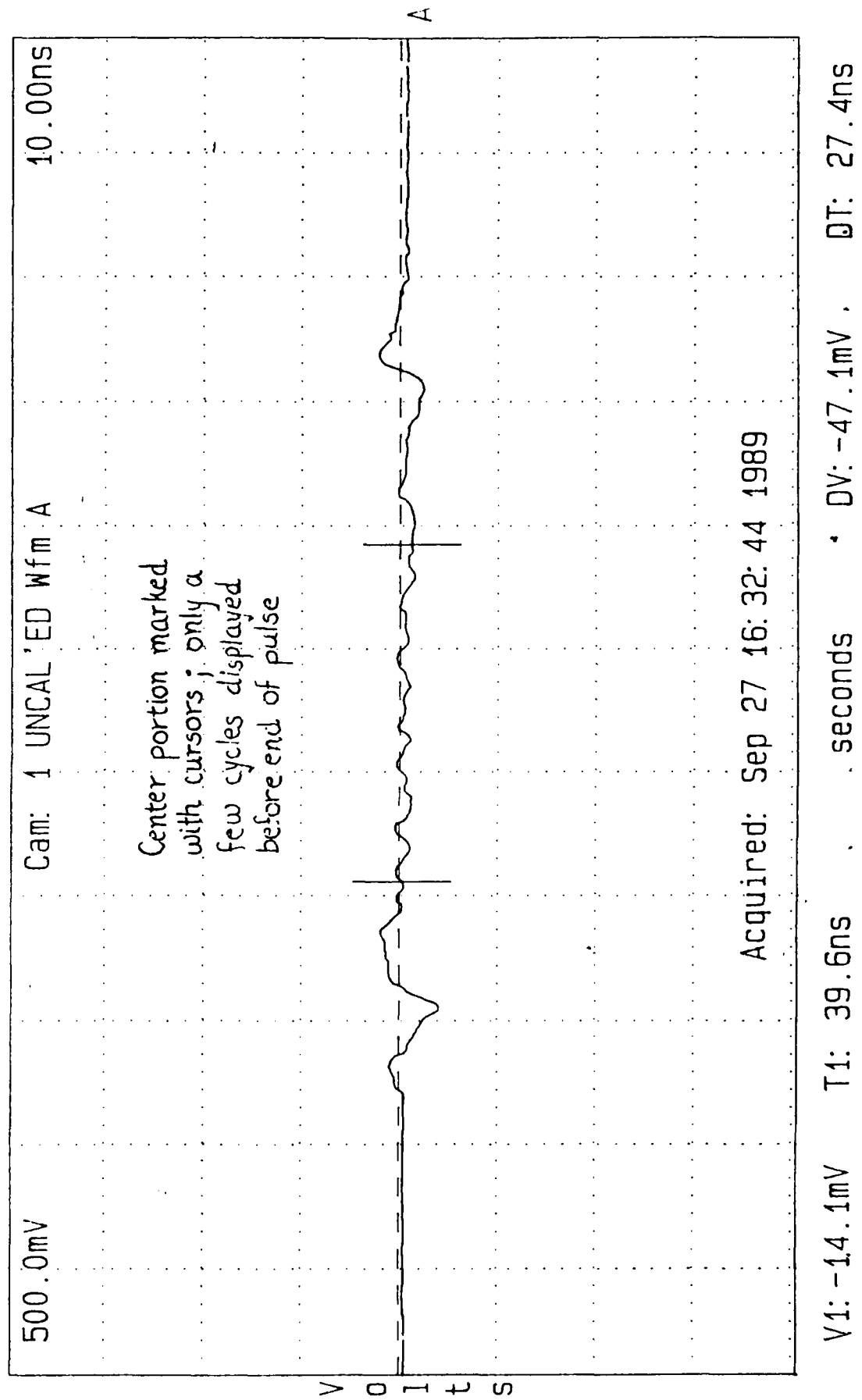


Figure 15. E-W subtracted signal, insufficient center portion length

to-peak), then by the Bottom port (1.33v), then the West port (1.27v), then the Top port (1.20v). For a centered shot on 28 September, the order of strength was different: Bottom (1.35v), then Top (1.37v), then West (1.35v), then East (1.30v). All that can be deduced from data like this is that the beam was not centered, or magnitudes or signals seen by the ports would have been equal; and there was inconsistency in similar shots. In other shots, there was a general increase or decrease in magnitude of a signal seen by a port as the REX pulse rose, maintained constant current, then fell (see Figure 16). This is indicative of the energy dependent directional (spectroscopic) sweeping that a solenoid magnet with residual  $B_x$  and  $B_y$  fields may do to a non-centered and imperfect electron beam pulse: the pulse itself does not have entirely symmetric energy distribution throughout its rise, duration and fall. There is more energy present in general during the first half of the pulse. During this first half of the pulse, the magnet bends it more and more as the energy density increases; with maximum bending occurring when the current of the pulse is maximum and relatively consistent. During the last half and fall of the pulse, the magnet bends the beam less. The result can be directing of a beam in the x and/or y direction. (A beam that enters the center of an ideal solenoidal magnet is guided along its axis which is the

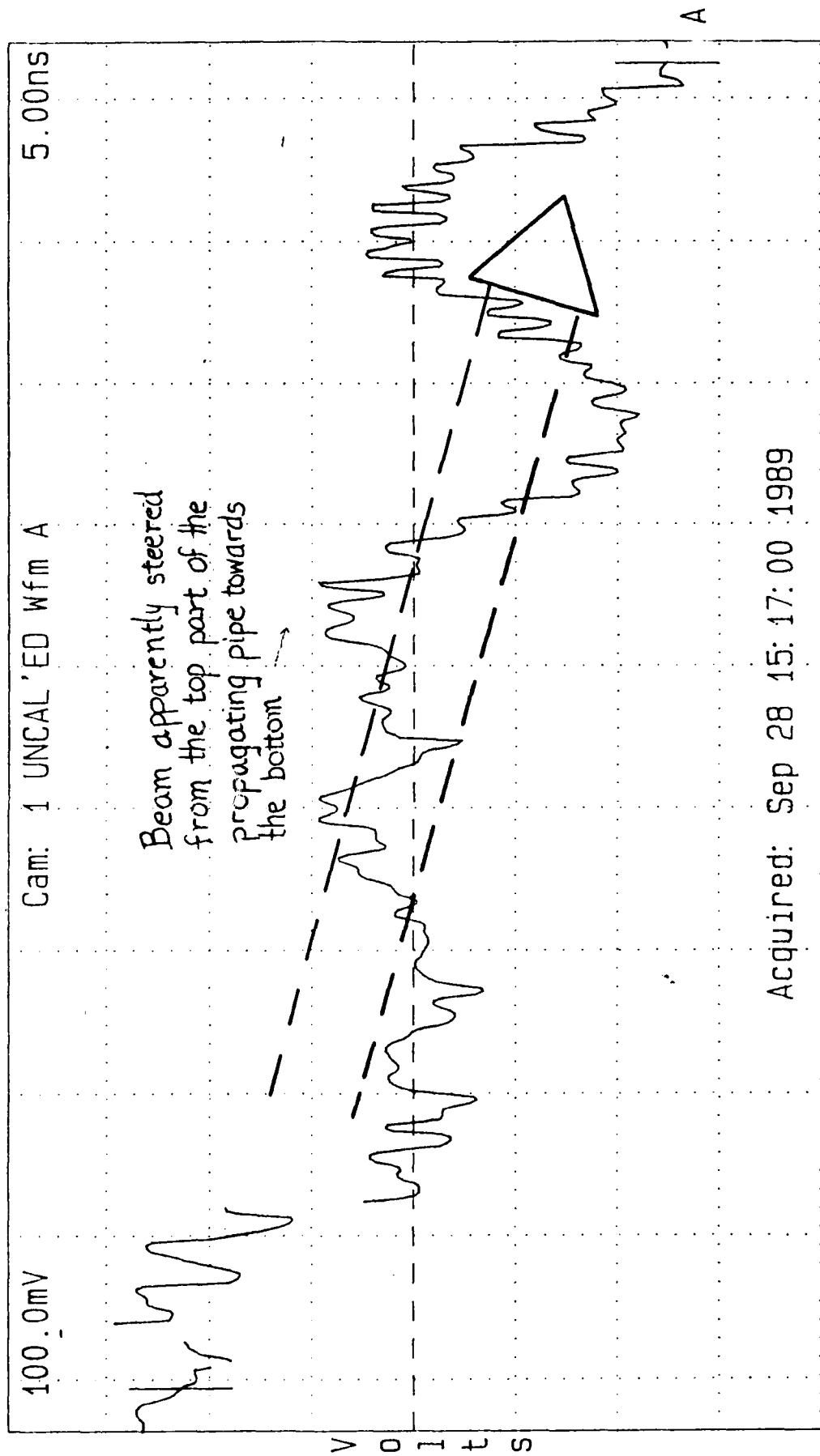
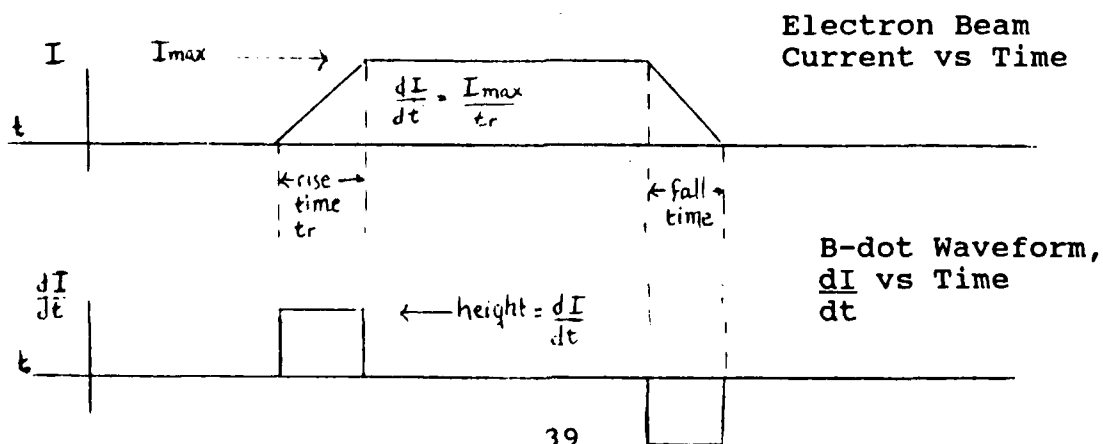


Figure 16. Possible spectroscopic sweeping

z direction of a cartesian coordinate system. The magnet's  $B_x$  and  $B_y$  components have ideally been minimized in its design). A third indication that the beam was not centered was given during a routine inspection of the REX assembly between shots: at the end of the assembly, downstream from the B-dot ring, the "can" housing the mask and scintillator for the streak camera had a crack in the glass endplate (beam stop) where the electron beam terminated. The crack in the circular glass was located 0.4 cm down from its center, and 1.1 cm toward one side. This noncentering of the beam and inconsistent shot-to-shot effects were to be reduced by a new magnet design. The new magnet was to be a bifilar wound solenoidal magnet, designed and manufactured by the M-4 Hydrodynamics group. (Bifilar winding was to cancel  $B_x$  and  $B_y$  fields.)

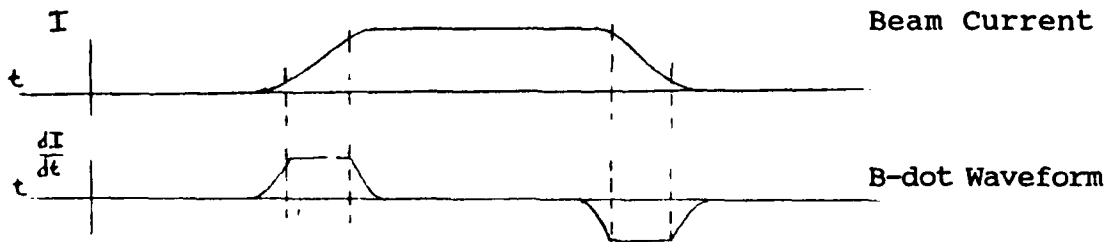
Investigation of factors effecting the shape of a B-dot waveform was begun in the preliminary experiment. Ideally, the waveform shape is a perfect derivative of the electron beam current pulse:

(Drawing C)



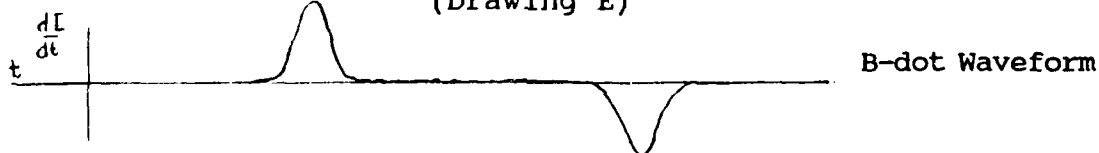
Since the current pulse shape is more rounded, with a portion of the rise and fall of the pulse approximately a straight line, the B-dot waveform shape is more closely pictured as:

(Drawing D)



Finally, since the straight line portion of the current pulse is very short, the edges of the B-dot waveform are rounded, and the shape is Gaussian:

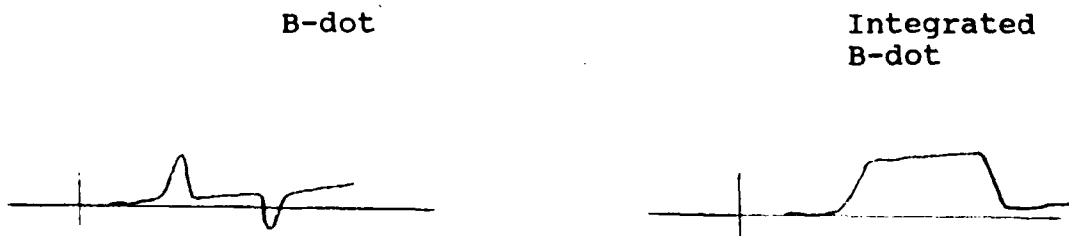
(Drawing E)



The factors identified in the preliminary experiment that modify the shape shown in Drawing E included:

If the oscilloscope graticule is rotated from perfect horizontal-vertical orientation, the DCS camera will copy a baseline that is not perfectly horizontal. In that case, the B-dot waveform base will contain a built-in slope, as shown:

(Drawing F)



This is difficult to entirely eliminate when adjusting the graticule rotation by eye. It can be minimized and, of course, can be recognized in a signal and allowed for as an artifact not created by any electron beam characteristic.

Noise from various sources alters the shape of the B-dot waveform by making it irregular in shape:

(Drawing G)



As might be expected, noise is the most difficult waveform factor to identify and reduce. Noise sources include connectors, cables, imperfect grounding, undesirable port-to-port cross-talk and standing wave reflection, power supplies, digital noise that depends on factors such as numbers of camera pixels, how wide the bright waveform trace on the oscilloscope is, numbers of significant figures and round-off errors; and other general electromagnetic interference noise. In fact, it was impossible to separate noise from signals in the preliminary experiment. The longer duration pulses from precision B-dot sensors that were examined in the calibration experiment were much more conducive to noise-chasing efforts.

The decision was made to use the passive ANZAC adder/dividers in the preliminary experiment to avoid the extra time involved to manually perform digital addition and subtraction of waveforms. How well these devices worked was not determined due to the noise and inconsistent signal



effects described earlier. These and other brand passive devices were re-examined in the calibration, because how well the B-dots performed was affected by how their data is analyzed by the passive or digital methods.

Even though the waveforms resulting from the rough preliminary experiment were not of high enough caliber to be analyzed on detail, a large amount of practical knowledge was produced in the process of obtaining them. The "lessons learned" supplied the directions of exploration for the detailed calibration experiment and placed the goal of the ability to calibrate B-dot sensors within reach.

#### C. EXPERIMENTAL GOALS: CALIBRATION EXPERIMENT

The experimental goals of the calibration experiment were to refine the conclusions of the first experiment, and to calibrate the new B-dot sensors to defined accuracies in detecting electron beam position and movement. Specifically, it was desired to:

- continue to assess the performance of the Tektronix digitizing, visual presentation, and data manipulation system
- determine the precision of a B-dot sensor ring under ideal test stand conditions
- investigate, quantify and reduce sources of experimental error
- compare measured signals with theoretical predictions

- continue to identify the factors that affect B-dot waveform shape
- Fourier analyze the center portion of differenced waveform signals for comparison with known diode made frequencies
- compare the B-dot waveform measurements of beam position and movements of beam position and movement with streak camera imagery for calibration purposes.

The current experiment was performed in two phases: test stand (ideal, static conditions), and dynamic conditions with REX beam oscillating and steered for deliberate static displacement. The procedure, data collection and reduction, and results of each phase will be presented in turn. Overall conclusions will summarize the result and identify areas for further experiment.

#### **D. CALIBRATION EXPERIMENT**

##### **1. Test Stand Phase Procedure**

The test stand configuration shown as Figure 10, was used in both preliminary and calibration experiments. The predominantly used pulse generator for B-dot test stand experiments was the HV 1000 Pulser, with the ~5 ns rise time pulse. (The REX pulse rise has a rise time ~15 ns.) The other pulser used was the Tektronix Type 109 0.25 ns rise time "Fast Pulser". The KEPCO power supply, in combination with the HV 1000 Pulser, input a 300V 5 ns rise CW pulse into the

inner conductor of the test stand for most tests. After traversing through the body of the test stand, the pulse was sent to the Tektronix R7103 Oscilloscope via two 30dB attenuators and displayed on the oscilloscope screen. This screen was monitored by a Tektronix C1002 Digitizing Camera, which converted the visual display to digital data for the software and computer, and by a small Ikegami TV monitor. Thus, the pulse could simultaneously be viewed by the camera and the operator to facilitate graticule scale and other oscilloscope adjustments. The pulse was "captured" upon operator command by the IBM PC AT-286 computer with color monitor and Tektronix version 2.06 Digital Camera System software for manipulation, analysis, and storage. [Ref. 11:pp. 1-10]

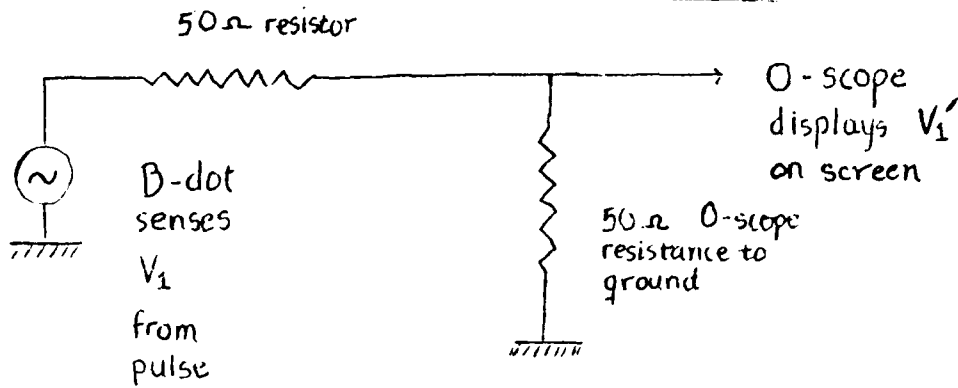
In the center of the test stand cylindrical conductor housing, which was mounted on rollers for easy travel, was a flanged opening where a B-dot ring could be inserted. When the insertion was complete, the cylindrical housing could be shut, and the two halves of the inner conductor would be reconnected. Although it was possible to use standard nuts and bolts to secure the B-dot ring in place, more accurate readings were obtained by using guide pins that barely fit through the bolt holes, and C-clamps around the outside flanges, to eliminate gaps, leaks, and noise.

Heliac one-half inch superflexible foam dielectric coaxial cables and Pomona connectors were used to connect the

B-dot ports to the oscilloscope amplifier module inputs. Other devices that could appear in this circuit were Weinschel model 1506A dividers ("power tees", used to split signal from one B-dot port), MCL and ANZAC voltage dividers (used to subtract two input signals), ANZAC voltage adders (used to add two to four input signals), and Applied Research Inc., model 24931 attenuators. Two simplified circuit diagrams illustrating the B-dot and test stand arrangement are shown in Figure 17.

The general test stand procedure used was to insert a B-dot ring into the flanged housing, select a desired pulse, and attach cables and connectors to the oscilloscope. Then, using the DCS software, appropriate voltage-per-division (Y axis on oscilloscope and computer screens), time-per-division (X axis), amplitude, and other settings for the desired experiment were selected. The resulting B-dot waveforms were recorded on the computer hard drive and floppy disks.

B-dot Test Stand Circuit  
(50 ohm B-dot Port)



$$\text{Loop } V_1 \left( \frac{50}{51+50} \right) = V_1 (0.495) = \text{Screen } V_1' \frac{1}{2} \cong \frac{1}{2} V_1$$

Passive Adder/Divider Circuit

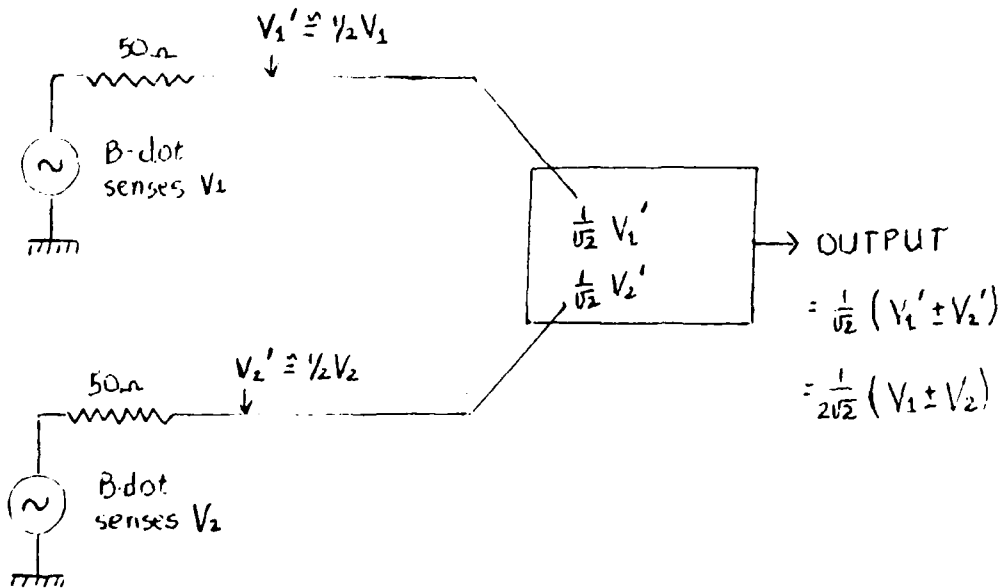


Figure 17. B-dot stand circuit  
(50 ohm B-dot port)

## 2. Test Stand Phase Data Collection, Reduction, and Results

### a. Port-to-Port Differences for B-Dot Rings

Three B-dot rings of the type shown in Figure 3 had been constructed specifically for this experiment, with sensor port the configuration shown in Figure 14. Thus, the Anode B-dot Ring and Aluminum B-dot Rings 1 and 2 (ABR1 and ABR2) possessed two sets of four 90 degree spaced ports. One set had 50 ohm resistors, and the other set did not ("wire" ports), as previously described. To test port-to-port electronic differences, the 5ns rise time 300V pulse was measured on each B-dot ring port. (One cable and connector and one oscilloscope amplifier module was used for all these measurements for uniformity.) The test stand inner conductor pulse was also recorded. The area under the recorded B-dot waveform curve was measured in the same manner for all ports as shown in Figure 18. One set of measurements was taken on

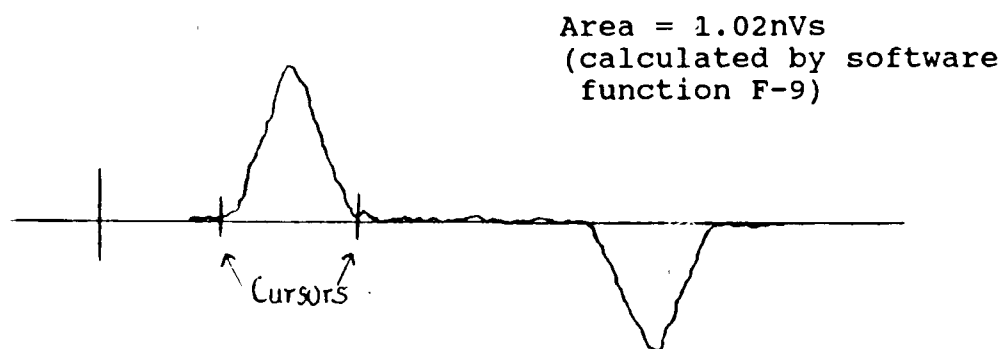


Figure 18. Measurement of 300V 5ns rise pulse by a B-dot port for port-to-port difference assessment

02 March for the B-dot rings to ensure that port differences were on the order of 1-2%. A second set of measurements was made on 20 March for the ABR1 and ABR2 rings for use in quantitative data reduction. These measurements are listed in Table I, Appendix E. An interesting phenomenon was noted: the port-to-port electronic differences increased slightly from the initial values (1 percent or less for all wire ports and 1.5 percent or less for 50 ohm ports). When tested on 20 March, after 130 REX shots, wire B-dot port-to-port differences increased to 1.9 percent or below, and 50 ohm ports differences increased to 2.5 percent or below. Since identical test stand equipment and conditions were used for both set of tests, the reason for the change is not immediately obvious. (The change was not restricted to magnitudes of port differences. In a few ports, the direction of the differences also changed: for instance, ABR2 Wire 1 changed from 0.6 percent above average to 1.2 percent below average. Further experiments involving radiation and thermal monitors, colocated with the B-dots, and monthly test stand measurements may identify the reasons for the port-to-port difference changes).

For the calibration experiment, the 20 March ABR1 and ABR2 measurements (several sets were taken and averaged) were used to derive individual port calibration factors, as described in the next section.

**b. Individual B-Dot Loop Area Dot Measurements**

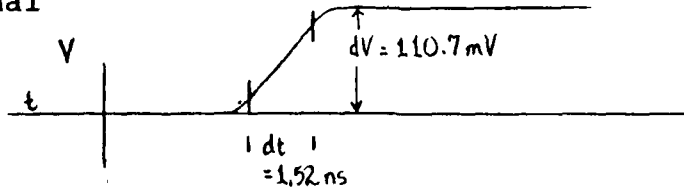
The theoretical approximate physical loop area for a B-dot was shown in Figure 14 as the product of the distance from the inner edge of the pin tab to the ring wall and the distance from the pin down to the pin base. The measurement of these distances for ABR2 and additional test stand B-dot ring was made when the rings were partially assembled, using a small telescoping Starrett gauge and Starrett dial micrometer (accuracy +/- 0.001 inch). (The other B-dot rings were not measured. Quantitative experimental data was taken only from the two rings mentioned above.) Due to the manual difficulty involved in centering the telescoping gauge and reading the gage-measured distances with the same amount of micrometer dial finger pressure, at least two sets of measurements were made for each port. The measurements are given as Table 2 in Appendix E. Individual port loop area differences from average ring loop area were on the order of 1 percent or less. The average theoretical loop area for the test stand B-dot ring was  $0.1584 \text{ in}^2$ ; for ABR2,  $A = 0.1600 \text{ in}^2$  ( $1.032 \text{ cm}^2$ ).

To find the effective B-dot loop area, which might be expected to differ from the theoretical calculation due to manufacturing differences and measurement inaccuracies, a 5ns rise 300V input signal (see Drawing H) was employed.

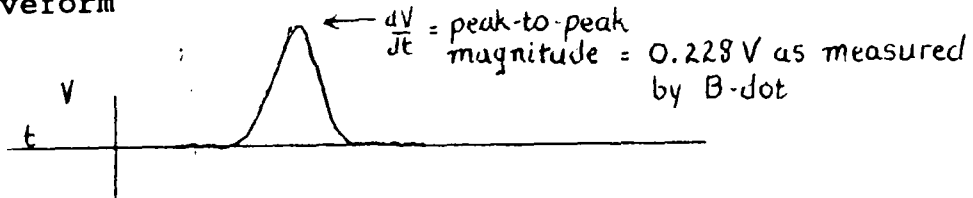


(Drawing H)

Input  
Signal



B-dot  
Waveform



$$\frac{dI}{dt}; \quad \frac{V}{R} = I, \quad \frac{dV}{dt} \frac{1}{R} = \frac{dI}{dt}$$

$$\frac{(110.7 \text{ mV})(1000)}{(1.52 \times 10^{-9} \text{ s})(50 \text{ ohm})} = \frac{dI}{dt}$$

(factor of 1000 from 230 dB attenuators)

$$1.46 \times 10^9 \frac{\text{Amp}}{\text{s}} = \frac{dI}{dt}$$

$$V = -\frac{A\mu}{2\pi R_0} \frac{dI}{dt}$$

$$V = \frac{-(1.032 \text{ cm}^2)(4\pi \times 10^{-9} \text{ H/cm})(1.46 \times 10^9 \text{ A/s})}{2\pi(7.907 \text{ cm})}$$

$$V = 0.3808 \text{ V}$$

= theoretical loop voltage circuit corrections)

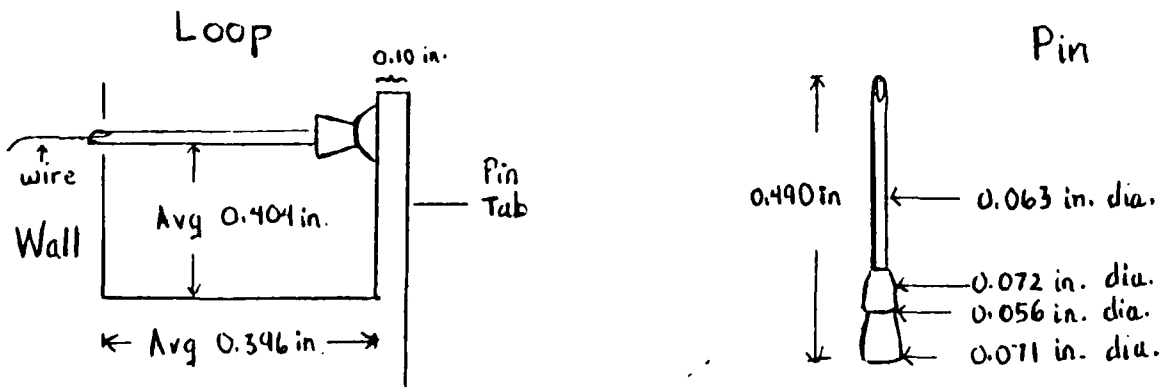
This voltage would theoretically be sensed by the B-dot loop if it was in a simple circuit with no outer resistances. To correct for the effect of the B-dot Test Stand circuit, as shown in Figure 17,

$$V = \begin{array}{l} \text{(theoretical} \\ \text{loop voltage} \\ \text{without circuit} \\ \text{corrections)} \end{array} -0.3808V \begin{array}{l} [0.495] \\ \\ \\ \end{array} = 0.175V \begin{array}{l} \text{predicted} \\ \\ \\ \end{array}$$

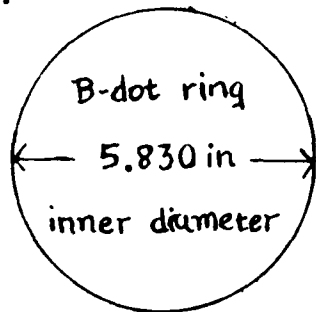
(negative sign removed; 0-scope polarity switch can change voltage signs)

As shown in Drawing H, the B-dot measurement is 0.228V, approximately 30 percent higher than the prediction. The causes of this difference include the fact that the permeability of free space was used instead of that of air and that of the polystyrene test stand inner conductor support, and that simplifying assumptions had been made in measuring both the loop area and  $R_0$ , the radius of B-dot ring (from its center to the middle of the loop.) The fact that the pin had a finite and non-uniform width was neglected. The pin shape is shown in Drawing I:

(Drawing I)



(The pin tab also had a finite width, which was also neglected.) The radius  $R_0$  was taken to be the same for all B-dot rings and was calculated from blueprints (see Appendix D):



(Drawing J)

$$R_0 \text{ (Avg)} = \frac{5.830}{2} + \frac{0.396}{2} = 3.113 \text{ in}$$

$$= 7.907 \text{ cm}$$

The corrective factors for the combination of all port-to-port area differences and all simplifying assumptions were obtained by using Equation 15 with the known voltage signal for each port. For instance, if ABR2 top port measurement was 30.3 percent too high, top port effective loop area was calibrated to be

$$(1.032 \text{ cm}^2)(1 + 0.303) = 1.345 \text{ cm}^2$$

$$= \text{Effective loop area}$$

A table of effective loop area correction factors is given as Table 3 in Appendix E. The average loop area correction factor was computed to be 1.193.

#### c. B-Dot Sensitivity to Static Position

Static displacement of the current-carrying conductor is proportional to the difference in voltage signals of opposed B-dot ports, as given previously by Equation 11; for the x-dimension, using the west and east ports,

$$\Delta X = \frac{R_0}{2} \left[ \frac{\int \Delta V_x dt}{\int \sum V_x dt} \right]$$

$\int \Delta V_x dt$  is the digital voltage difference, integrated to obtain the area under the voltage curves. Use either (Integrated West B-dot) - (Integrated East B-dot) or (Integrated West-East)

$\int \sum V_x dt$  is the integrated digital voltage sum (Integrated West + Integrated East) or (Integrated West + East)

This was demonstrated on the test stand by moving a B-dot ring from side to side with a small dial micrometer driven support table positioned under the ring. The test stand inner conductor could thus become more closely positioned to either the west or east port than before movement. For example, as ABR1 was moved in this manner progressively by 1mm, 2mm, 5mm, 1.0cm, and 1.5cm,  $\Delta X$  followed the predicted linear relationship (see Figure 19).

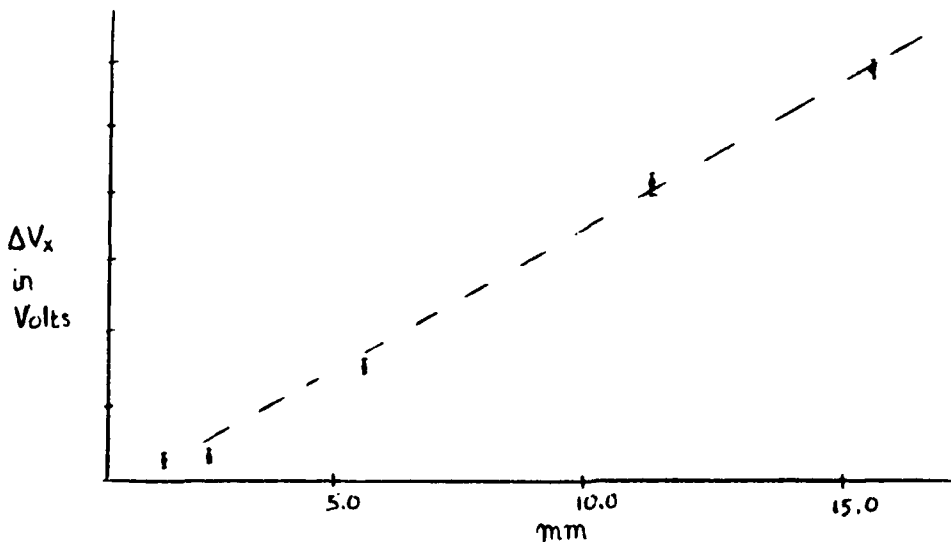


Figure 19. Change in  $\Delta V_x$  with Static Displacement

The limit of sensitivity of measurement of  $\Delta X$  is set by the digital subtraction limit. When the waveforms are very similar ( $\Delta X \ll 1\text{mm}$ ), digital subtraction waveforms too closely resemble noise to give accurate results. A graphic demonstration of digital subtraction "noise" is given by Figure 20. A Systron-Donner 1010 pulse generator was used to synthesize a 1200 mV magnitude Gaussian waveform. This same waveform was acquired ten times, using five DCS camera views for each acquisition. The ten waveforms were subtracted from each other in pairs. Perfect zero results were not achievable; instead, waveforms with an average 1 percent of the original waveform height resulted. This implies that for typical test stand waveform heights of 180mV, a digital difference of 2 mV could not clearly be distinguished from noise. This would limit the resolution of  $\Delta X$  as follows:

$$\Delta X_{\text{digital resolution limit}} = \frac{7.907 \text{ cm}}{2} \left[ \frac{182\text{mV} - 180\text{mV}}{180\text{mV} + 182\text{mV}} \right] = 0.0218 \text{ cm} \cong 0.22\text{mm}$$

Digital noise original waveform

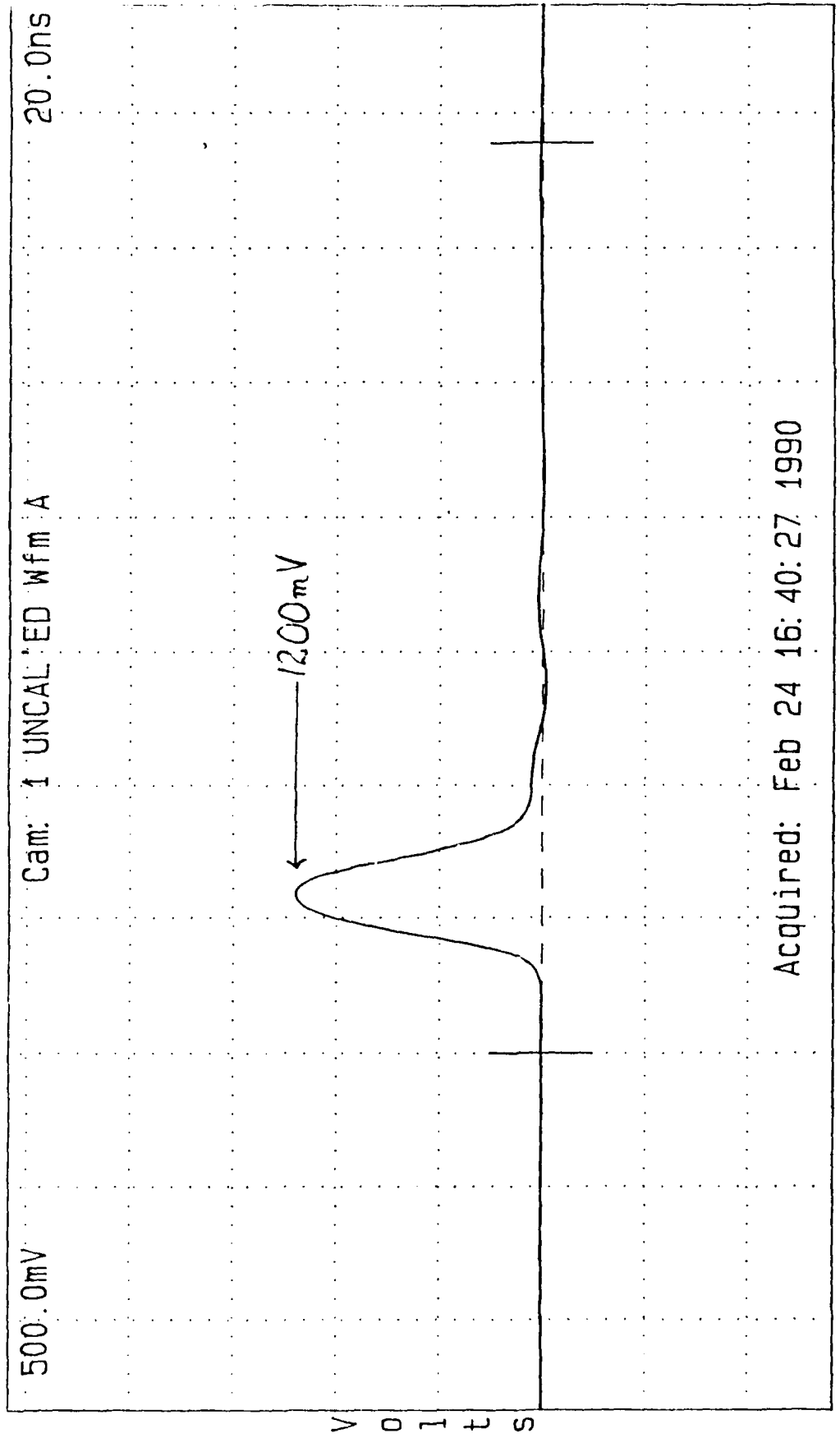
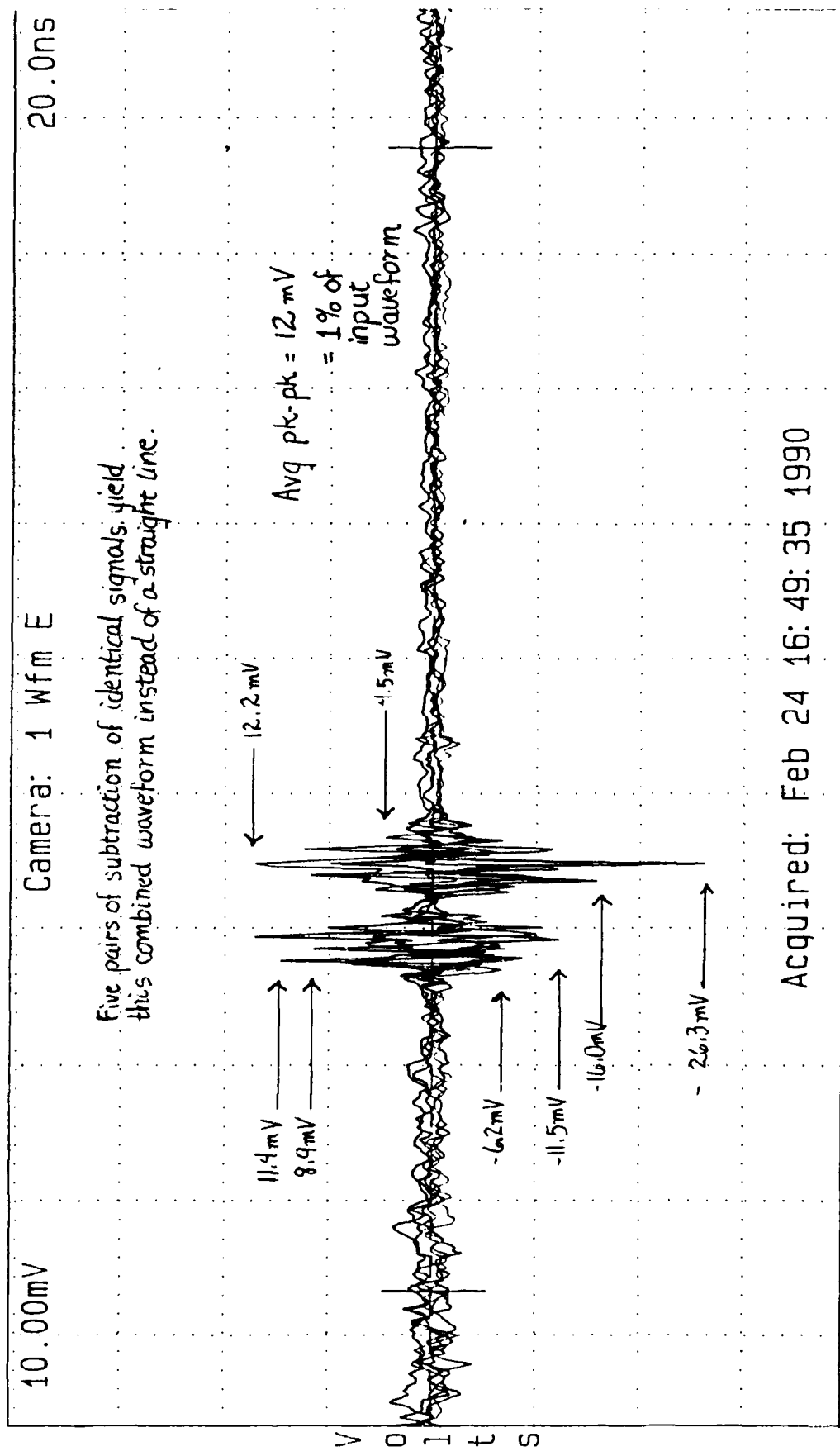


Figure 20(a). Digital noise study input waveform

Digital noise 1/4 mm resolution study



Acquired: Feb 24 16:49:35 1990

V1: -291.7uV T1: 20.0ns seconds DV: -104.2uV DT: 169.1ns

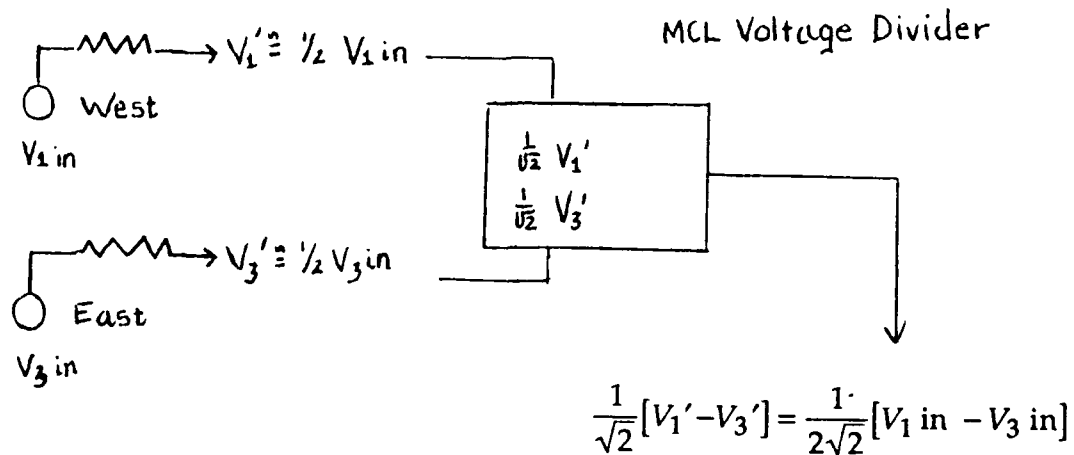
Figure 20(b). Digital noise 1/4 mm resolution study (Five pairs of subtraction of identical signals yield this combined waveform instead of straight line)

A more clearly distinguishable difference waveform for small  $\Delta X$  is obtained if a passive divider (subtractor) is used. The MCL divider is superior to the ANZAC device for this purpose, as it does not introduce artificial droop into the waveforms, and gives a linear response for:

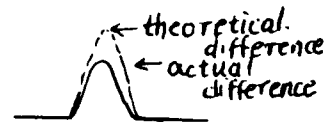
$$\Delta V_x = \frac{1}{2\sqrt{2}} [V_1 - V_3] \quad \text{(Equation derived in Appendix A.)}$$

for voltage inputs up to 300V. (This was tested with a 300V test stand signal and two 50ohm B-dot ports. See Drawing K.)

(Drawing K)  
MCL Divider Performance



when  $V_{in} > 350V$ :



MCL device manufacture specification; maximum port imbalance

= 0.15 dB:  $0.15\text{dB} = 20\log \frac{V_1}{V_3}$ ,  $10^{0.15/20} = \frac{V_1}{V_3} = 1.016$ ,

result: ~ 1.6 percent imbalance error



The MCL subtraction resolution is limited by its internal port-to-port imbalance, which introduces waveform magnitude uncertainties of 1.6 percent:

$$\Delta X_{\text{MCL resolution limit}} = \frac{R_0}{2} \left[ \frac{V - 0.984V}{2V} \right] = 0.03 \text{ cm} \cong 0.3 \text{ mm}$$

This imbalance plus a small amount of port-to-port reflection through the connector cables an MCL device results in a small "standing wave" signal even when the B-dot ring is perfectly centered on the test stand. See Figure 21. When the B-dot ring is moved towards one of the two horizontal ports (east or west) with a dial micrometer, the new resulting MCL subtracted waveform is clearly distinguishable from the "centered" standing wave for movements of 0.25 mm or larger. (Smaller movements are less than MCL uncertainty and should not be relied upon as accurate data.)

Therefore, both passive device and digital subtraction method results yield a B-dot opposed-port low limit sensitivity to static position changes on the order of a quarter of a millimeter for the test stand.

1/4 mm study "DISQ"

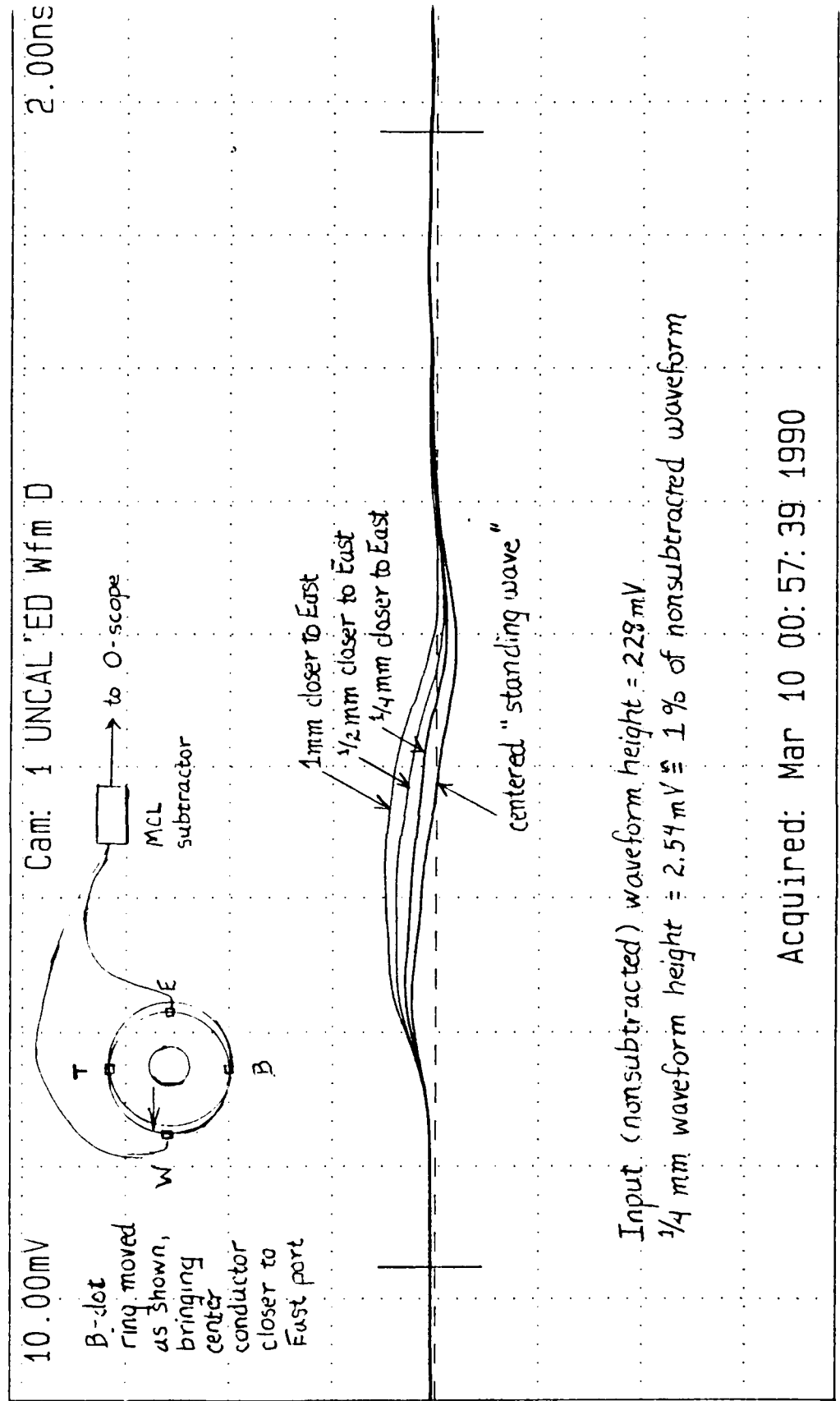


Figure 21(a). 1/4 mm study "DISQ"  
(B-dot ring moved closer to East port)

Expanded view: 1/4 mm resolution study "DISQ"

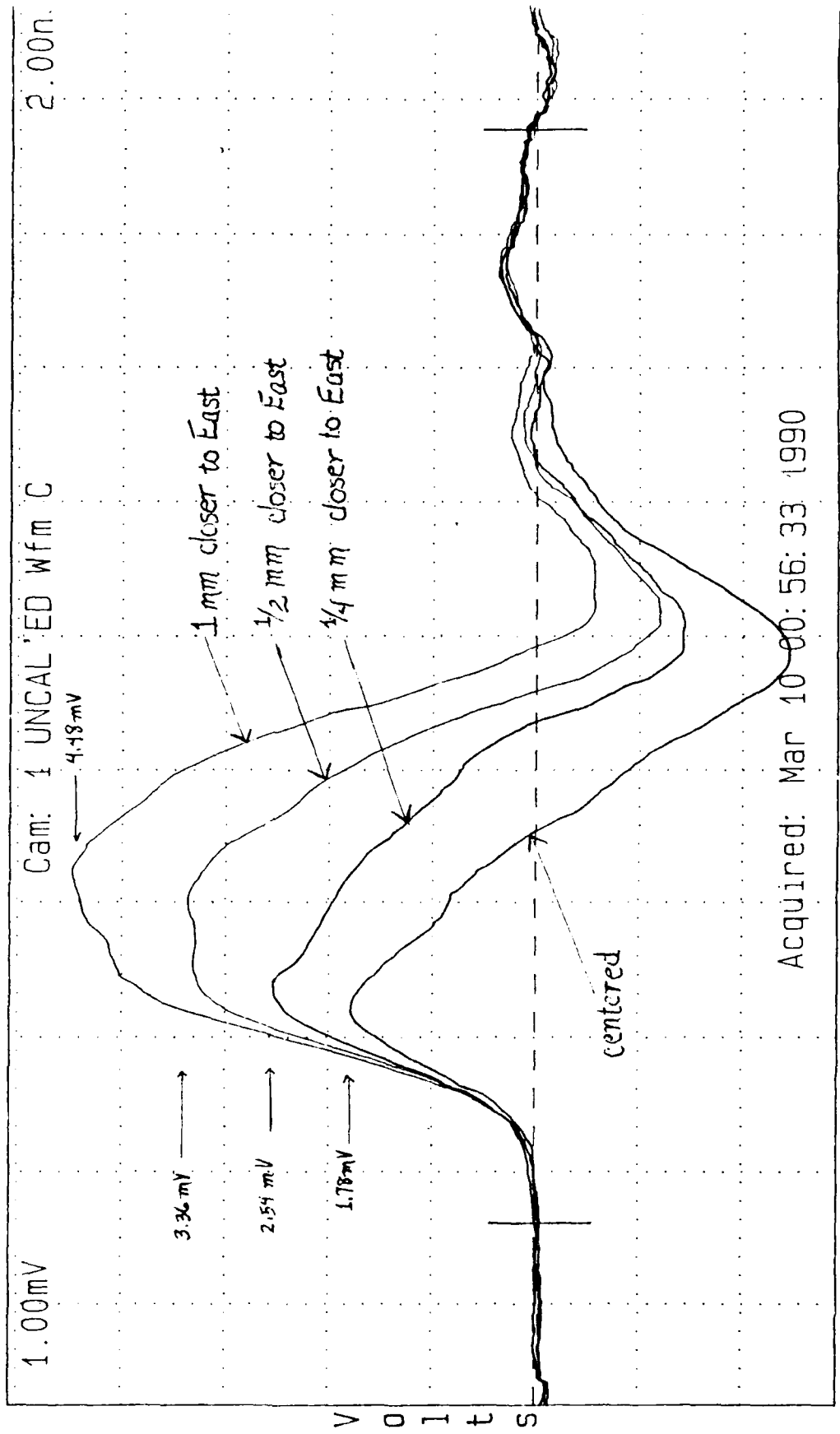


Figure 21(b). Expanded view: 1/4 mm resolution study "DISQ"

1/4 mm resolution study "DISP"

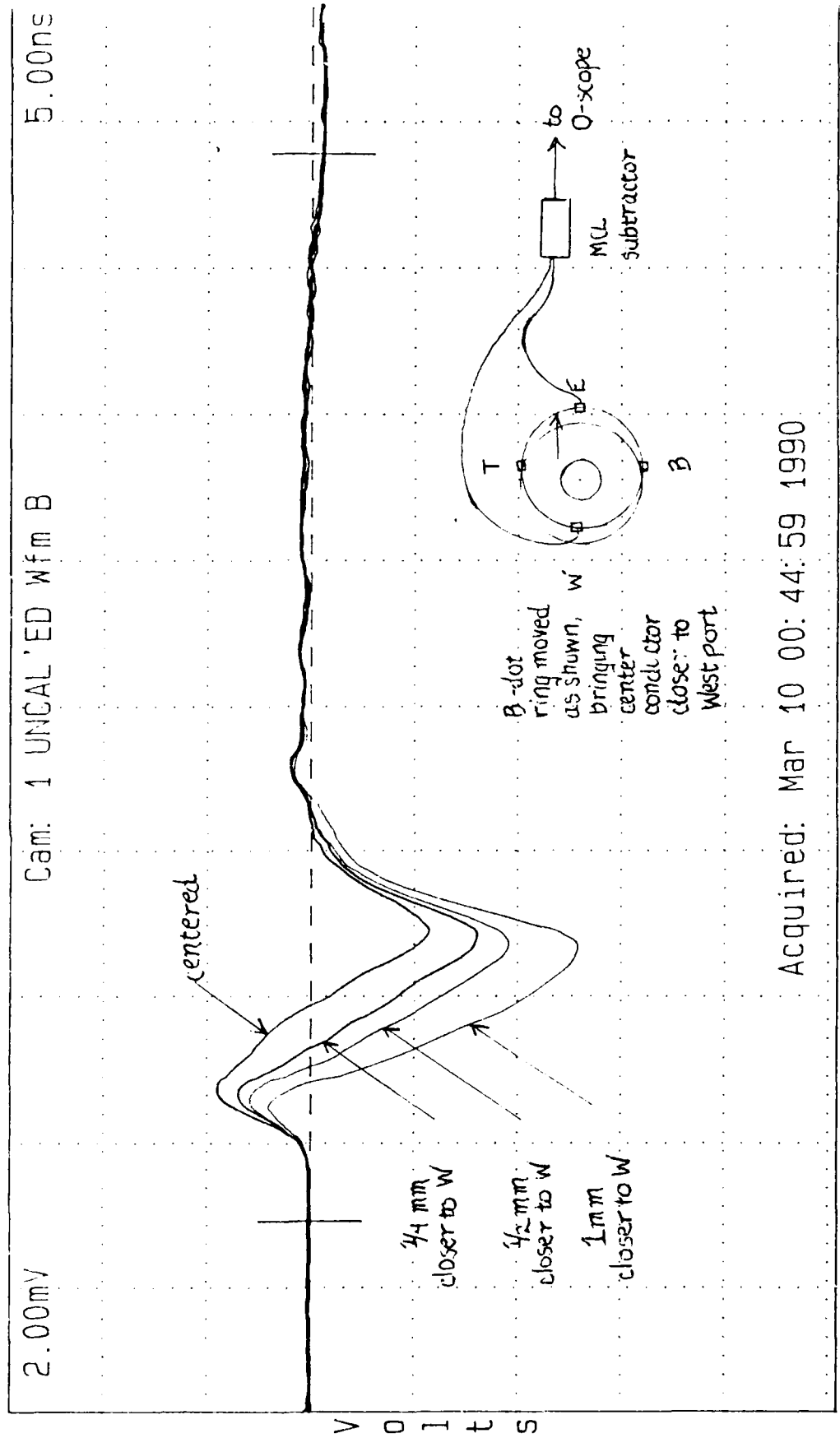
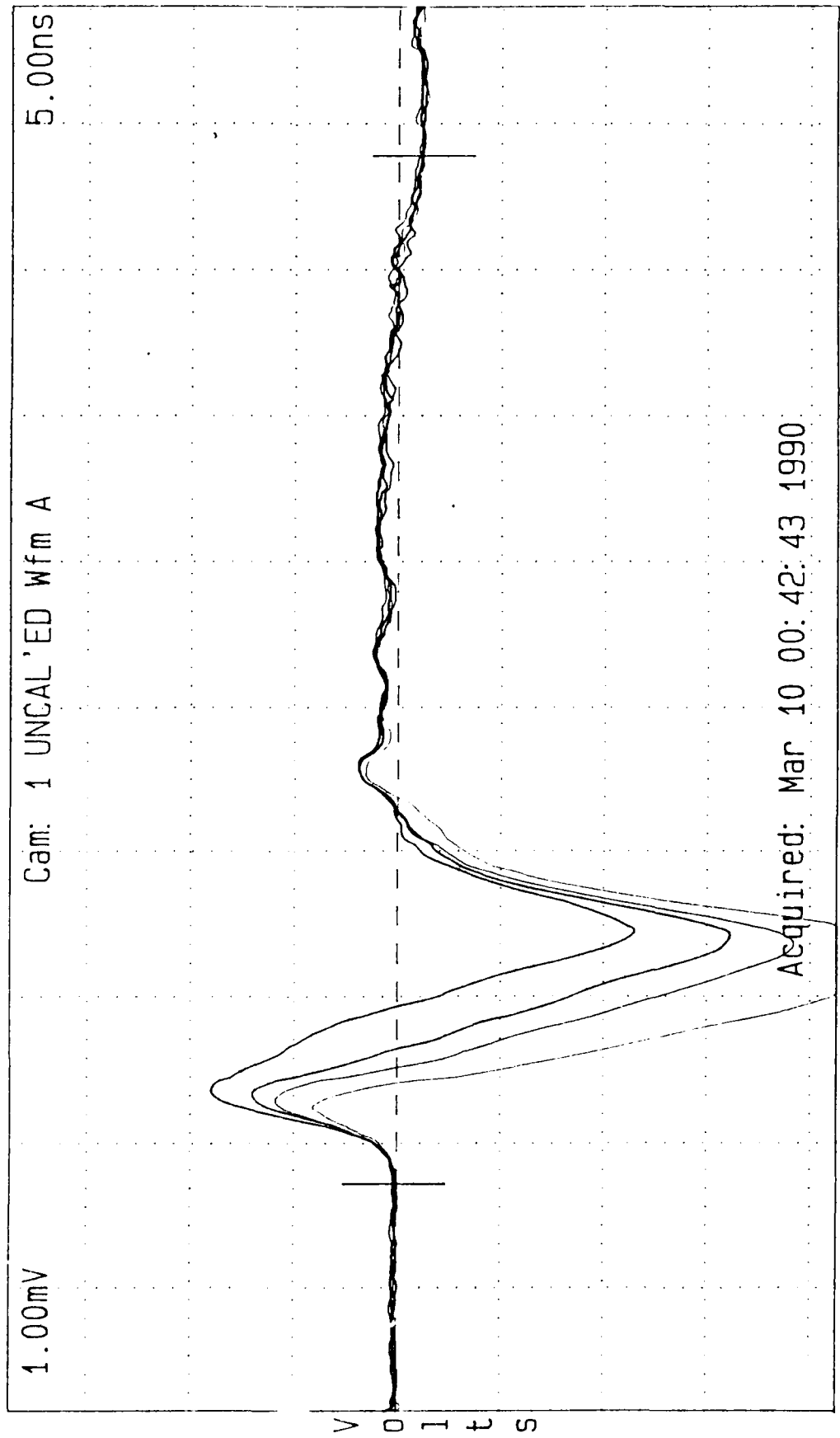


Figure 21(c). 1/4 mm resolution study "DISP"  
(B-dot ring moved closer to West port)

Acquired: Mar 10 00:44:59 1990

Expanded view: 1/4 mm resolution study "DISP"



V1: 24.0uV T1: 7.83ns . seconds DV: -268.8uV .DT: 35.3ns

Figure 21(d). Expanded view: 1/4 mm resolution study "DISP"

d. **Sources of Experimental Error**

The major sources of error for the test stand procedure include the DCS camera calibration, oscilloscope calibration, software processing errors, test stand center conductor misalignment, and cable and connector noise.

The DCS camera calibration procedure selected for the experiment is the "manual camera adjustment" [Ref. 11:p. 338]. An internal calibration square wave (from the R7103 oscilloscope upper panel) is energized and carefully aligned on the oscilloscope screen where the camera is fastened. The Ikegami television monitor is used by the calibrating operator to adjust the screen graticules and amplitude, focus, and width of the square wave. The camera is triggered by the operator to acquire the square wave. The resulting waveform shown on the computer screen is carefully inspected for correct height, width, and stability. The camera possesses fine dial traveling controls, whereby it may be physically moved closer to or further away from the oscilloscope screen. Moving the camera away from the screen will result in the acquired waveform becoming smaller in height and width (amplitude and time dimensions), for instance. Fine adjustments are made in this manner until the acquired waveform matches the calibration square wave as exactly as can be determined by the human eye. The result is a one-to-one match of oscilloscope screen image to computer screen waveform. The listed error for the minimal procedure is given

as 1 percent, except at the extreme outer edges of the screen, where it increases to two percent. (Portions of the waveforms appearing at the screen outer edges are not used for experimental data.)

The same internal calibration waveform is used to adjust the left and right oscilloscope amplifier modules. Oscilloscope amplitude, gain, rotation, and focus controls are manipulated until the waveform shown by both modules is as identical as can be determined by the human eye. This process is limited in accuracy to 1 percent. The amplifier modules are periodically checked to ensure that they are as well adjusted as possible and to ensure that they have not "drifted" away from projecting accurate waveforms.

The computer software processing system is limited by graphics resolution (approximately 0.3%). Graphics resolution includes processing and projection of calculations involving waveforms, processor operator error, round-off error, and the limited number of camera and screen pixels.

In addition, the camera and software acquire a waveform that is the centroid of a never completely stable bright line on the oscilloscope. The centroid location is determined arbitrarily by the line brightness, which is difficult to maintain at a level high enough for a statistically large enough number of pixels to show the waveform, yet low enough so that the line will not be so thick as to blur the centroid. These errors, although not

removable, can be estimated, through requiring the system to acquire a known waveform and perform a mathematical operation. The digital subtraction described previously is an example of this process. The result is an average 1 percent operator-processing error, which is systematically related to the camera error, but also involves the round-off and graphics averaging errors. For the purposes of this experiment, therefore, the computer operator-processing error will be treated as a separate error source.

When a B-dot ring is placed in a centered position on the test stand, the test stand inner conductor supposedly exactly passes through the ring's axis. This is never perfectly true, even when the ring is held in place with tightly fitting pins instead of grooved bolts, and further secured with large C-clamps. The test stand contains manufacturing nonuniformities. The most measurable of these is the position of the inner conductor. The inner conductor comes apart when the stand is rolled apart for insertion of a B-dot ring. The portions that fit together are supported in place by polystyrene bushings, a design to allow the permeability of the interior test stand to match that of air as closely as possible. Small polystyrene shims are inserted in the edges of the bushing where extra space occurs, to require the center conductor to be correctly positioned. Measurement of distances from the center conductor outer edges to the inner edges of the outer conductor reveals that there



is an average of 10 thousandths of an inch error in the position of the center conductor. Over a test stand diameter of approximately 2.9 inches, this represents an error of 0.35 percent.

Other sources of test stand error include cable and connector noise. When a test stand B-dot waveform sent through six feet of solid shield Heliac Superflex cable with two connectors was compared to one sent through forty feet of cable and several connectors, the shape of the waveform was not visibly affected other than by attenuation. For this experiment, the signal strength (on the order of 100V) is ample, and requires more attenuation than the cables provide to prevent oscilloscope damage. Therefore, cable and connector attenuation was assumed to be negligible. The predominantly used passive devices: ANZAC four-way adders and MCL subtractors, more completely described in Appendix C, contributed either a known 5 percent droop that could be allowed for in calculations, or no visible distortion, respectively.

Test stand experimental error, therefore, is assumed to be the combination in quadrature of the following:

$$\begin{aligned}
 \text{Test Stand Error} &= \left[ \begin{array}{cccc} \text{computer} & \text{oscilloscope} & \text{camera} & \text{test} \\ \text{processing} & \text{calibration} & \text{digitization/} & \text{stand} \\ \text{error} & \text{error} & \text{presentation} & \text{error} \\ & & \text{error} & \end{array} \right] \\
 &= \left[ (0.01)^2 + (0.01)^2 + (0.01)^2 + (0.0035)^2 \right]^{\frac{1}{2}} \\
 &= 1.77\% \cong 2\%
 \end{aligned}$$

### 3. Dynamic Phase Procedure

The specific goals of the dynamic phase procedure were to continue to identify factors affecting the B-dot waveform shape, perform Fourier analysis of B-dot signals recorded during REX shots, and to compare the signals with streak camera photographs and data. The equipment configuration used was that depicted earlier in Figure 7. The major differences in the current experiment compared to previous experiments were the use of the new B-dot rings, addition of Lambertson steering coils to purposely displace the electron beam, and the use of the longer pulse (~100 ns). Lower voltage and beam power settings were also employed (~ 4MV, ~ 4KA, versus previous ~5 MV) to reduce stress on the REX machine for the extended numbers of shots. Five DCS cameras and oscilloscopes monitored each shot. Three were normally dedicated to the basic REX monitors:  $V_{PFL}$  (pulse forming line voltage, sensor in water PFL),  $V_{TUBE}$  (pulse voltage at the radial resistor), and  $I_{DIODE}$  (current at the diode). The other two either monitored one B-dot port each or two sets of MCL device subtracted signals from four B-dot ports. By changing cable and connector locations, the beam could be monitored by B-dots either at the anode, just after the focussing magnet, or at the end of the propagation pipe. The streak camera, viewing the beam through the quartz beam top, provided either black and white opaque Polaroid film or transparent ("hard film") pictures of each REX pulse.

#### 4. Dynamic Phase Data Collection, Reduction, and Results

##### a. Factors Affecting Waveform Shape

The first REX shots monitored by the B-dots showed evidence of noise similar to that seen in the previous experiment. See Figure 22. For shot 4178, monitored by the top and bottom B-dots in the ring at the gate valve, noise was visible on the waveform traces even before the pulse commenced. To isolate this noise, the B-dot connector cable to the "Bottom" oscilloscope was disconnected. Ideally, that oscilloscope would show a straight line during a shot, but as shown in Figure 23, the oscilloscope displayed a waveform with two definite frequencies. The first was a low frequency (7 MHz) modulation of some sort, the second was a very definite 250 MHz low amplitude signal. A careful investigation of possible electromagnetic interference sources revealed that collocation of a trigger cable in the back of the oscilloscope equipment rack was resulting in spurious signals from the REX experimental area. See Figure 24. When the trigger cable was relocated, the two frequencies visible in the waveforms displayed by the oscilloscope with no inputs disappeared.

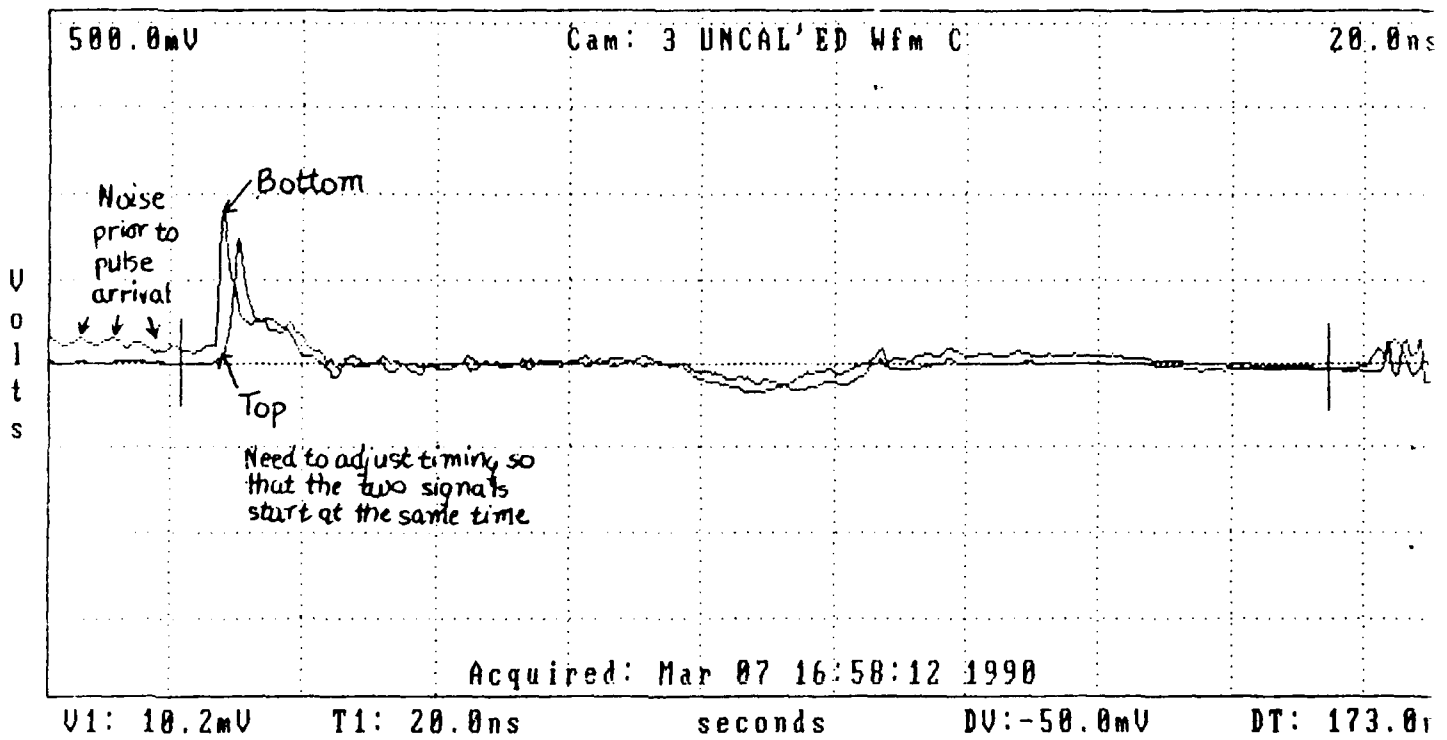
Further analysis of Figure 24 revealed that the 250 MHz frequency could be correlated to an event visible in the streak camera Polaroid picture for that shot. The beam was being sent through a vertical metal slit located in the mask "can" at the end of the propagation pipe (as described in Appendix C). The resulting vertical section of the beam

showed very definite oscillations in the top envelope of approximately 250 MHz. This event was evidently of sufficient strength and regularity to be sent to the control room on many connector cables, including the trigger cable.

The streak camera photograph (reproduced as a sketch on Figure 24) also demonstrated that the beam was being swept towards the bottom of the propagation pipe during the time of the pulse. This phenomenon was seen in most of the REX shots of the experiment and could be correlated with the spectroscopic sweeping seen in the previous experiment. Although not quantified in detail, the amount of spectroscopic sweeping present should roughly be proportional to the strength of the beam and the amount that the beam is displaced from axial center as it exits the diode and enters the focussing magnet. Specific studies of this phenomenon were not carried out for this experiment, but it was noted that the steering of the beam towards the bottom of the propagation pipe was markedly reduced when the apparatus was physically manipulated to center the beam during later shots.

The other factors affecting the B-dot waveform shape were the proximity of the beam to a specific B-dot and dynamic events occurring in the beam. Figure 22 shows both effects. The amplitude of the bottom B-dot waveform is greater than that of the top, including the closer proximity of the beam. Both B-dot signals show a regular oscillation in the center of the signal.

4178: C=Top, D=Bottom  
ABR1 (Gate Valve B-dot Ring)




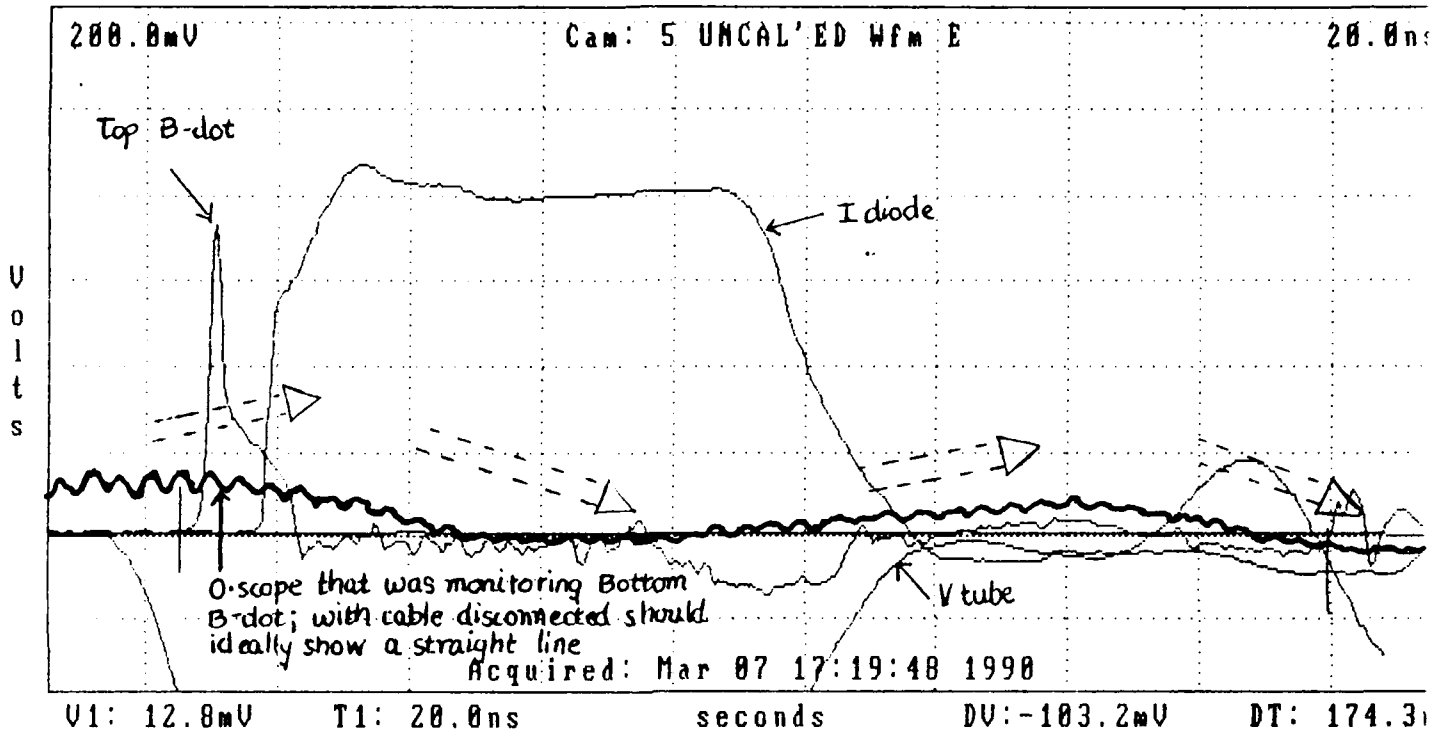
- Unknown noise
- possible low freq modulation 
- beam appears to be closer to bottom of propagation pipe

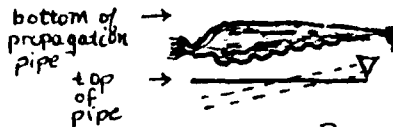
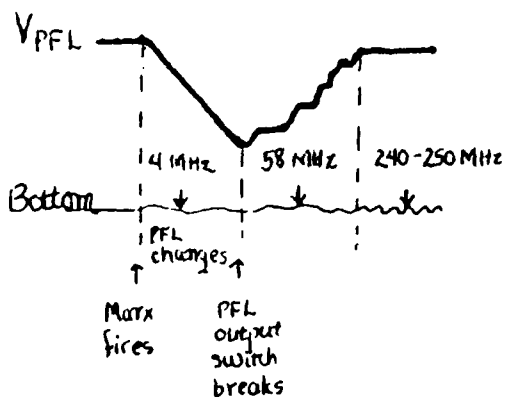
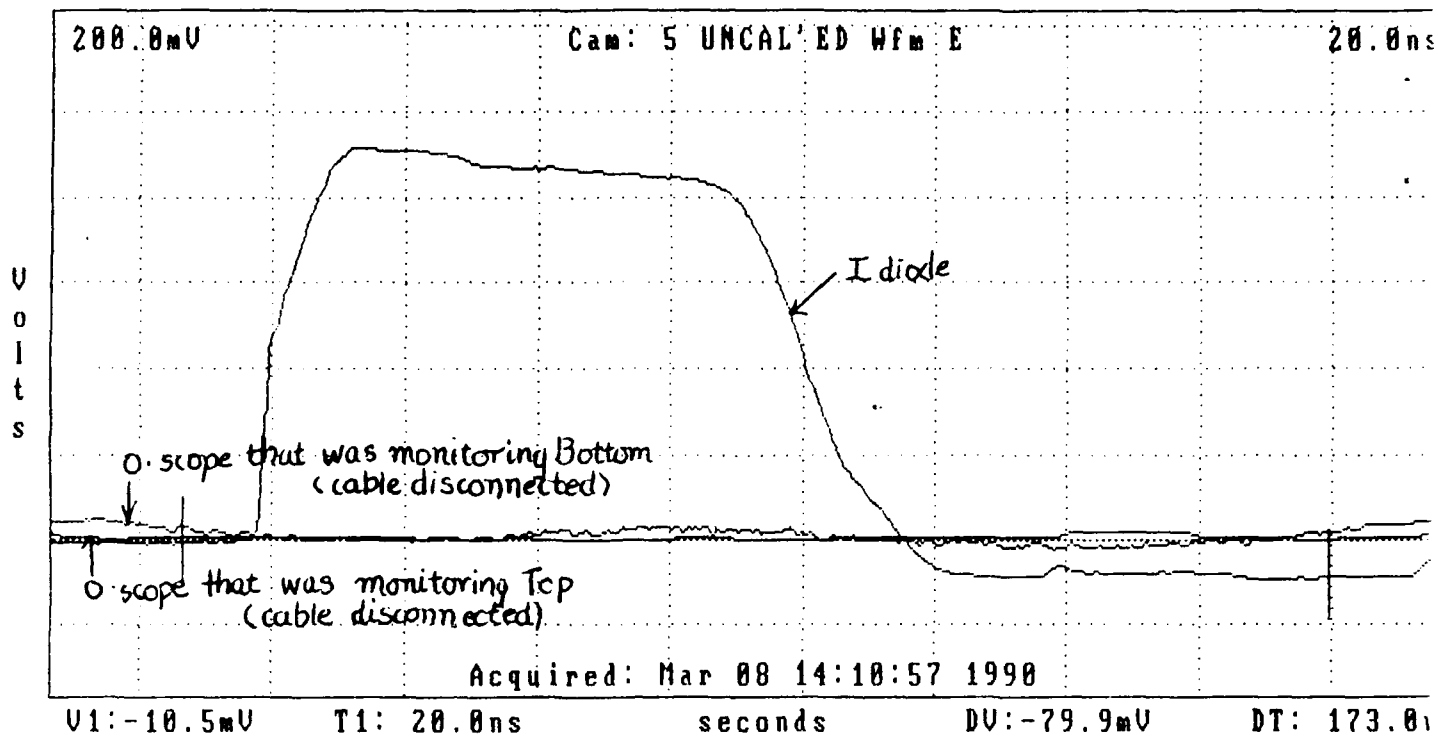
Figure 22. Noisy shot

4181: C=Top, D=no input to O-scope  
 (ABR1, Gate Valve)



- Definite low freq noise, approx.  $7 \times 20\text{ns} = 140\text{ns}$  period  
 $= 7\text{MHz}$
- Higher freq noise, period  $\approx 4\text{ns}$ , freq  $\approx 250\text{MHz}$

Figure 23. Bottom B-dot O-scope with cable disconnected



Sketch of streak camera photo

- Beam being steered or swept toward bottom of pipe throughout time of pulse

- Magnification of streak camera =  $9.3 \approx 10$ ; rough measurement of scalloping of top edge, using  $2\text{ns/mm}$ , shows oscillation at freq  $\approx 250\text{ MHz}$

- Noise shown here eliminated by relocating HV trigger cable from back of control panel and removing other EMI sources

Figure 24. Both top, bottom B-dot cables disconnected from O-scopes

b. **Fourier Analysis**

The Tektronix DCS software contains the capability of computing the frequency of an oscillating waveform. The software counts the number of oscillations in a time period and thus completes a simple frequency calculation, for the dominant oscillation in a waveform located between cursor positions selected by the operator. For nearly all of the REX shots, the software frequency analysis revealed the presence of a 240-250 MHz frequency. The software is not able, however, to discern the presence of multiple frequencies. Therefore, several representative REX B-dot signals were converted from the normal BINARY recorded form to ASC form and transferred from floppy disc to a VAX machine via a personal computer. The signals were analyzed with the Fast Fourier Transform IDL program given in Appendix E. The data are given in Table 4-1.

TABLE 4-1  
FOURIER ANALYSIS

FREQUENCY (MHZ)	# OF SHOTS IN WHICH THIS FREQ IS PRESENT	RELATIVE STRENGTH (% COMPARED TO DOMINANT FREQ PRESENT)
80	1	40%
100	1	30%
120	2	10%
125	3	20%
130	1	30%
165	1	10%
210	2	20%
240	12	(Dominant)
242	6	(Dominant)
248	12	(Dominant)
250	15	(Dominant)
440	2	25%



Figure 25 is an example FFT analysis result. It clearly shows the dominant 250 MHz frequency and two to three secondary frequencies. Over the range of shots analyzed, however, only the 240-250 MHz dominant frequency was clearly reproducible. Secondary frequencies were not produced on sequential REX shots fired using the same power parameters. The conclusion is that the REX shots of this experiment definitely demonstrate only the 240-250 MHz oscillation. A computer simulation of REX diode dipole modes (using the wavefield code ANDY, a shock excitation of the diode cavity with a dipole charge, and Fourier Analysis, carried out by Mission Research Corporation and Los Alamos Group (M-4) previously identified cavity resonances at 250 MHz, corresponding approximately to the lowest dipole transverse electric and transverse magnetic modes of the diode cavity. It is very likely, therefore, that the 240-250 MHz oscillation is a diode cavity resonance mode. [Ref. 6:pp. D-10,D-11]

**c. Comparison of B-dot Signals to Streak Camera Data**

The Lambertson steering coils were used to displace the beam in the vertical direction. According to calculations for the magnets [Ref. 12:pp. 1-2] (See Appendix A), an average displacement of 0.17 cm per ampere of current applied was expected. See Figures 26-28. Figure 26 was a non-steered (zero current supplied to Lambertson steering magnets) signal. Static displacement of the beam, calculated from Equation 11 was 0.15 cm above pipe center. Figure 27 was

a top-steered shot using a +10 Amps current; the calculation resulted in the beam's being located 1.77 cm above pipe center; +10 Amps current, therefore, displaced the beam a net 1.62 cm. Similarly, Figure 28 was a bottom-steered shot using -10 Amps current, displaced 1.33 cm below pipe axis; net displacement from the non-steered position was 1.48 cm. These displacements are slightly less than the predicted 1.7 cm for 10 Amps steering magnet current, but the prediction was based on average beam energy and simplified geometry and can only predict approximate displacement. There is, therefore, reasonable agreement of actual beam displacements with theoretical predictions.

The streak camera photographs shown have been magnified from the original Polaroid photo size. A standard mm ruler was placed on each photograph aligned with the top marker (an extra hole in the mask above the vertical beam slit, described in Appendix C). (Note: Due to the camera geometry, the top of the beam envelope is at the bottom of the streak camera picture. The start of the beam pulse,  $t = 0$ , is shown as the bright blob at the left of the pictures; the end of the pulse is on the right side of the pictures, at  $t = 80 - 90$  ns.) A rough streak camera static displacement relative to the marker can be carried out. For example, in Figures 26(b) and 27(b), the position of the beam centroid relative to the marker was measured, and the beam centroid in Figure 27(b) is approximately 1.14 cm closer to

the marker than the non-steered beam. This is in agreement (for order of magnitude) with the 1.62 cm displacement measured by the B-dots, but it is not possible to calibrate the B-dot with the streak camera to the 0.25 mm test stand standard. The best REX/streak camera B-dot calibration for transverse static displacement is 0.5 mm, a conservative estimate of the streak camera resolution.

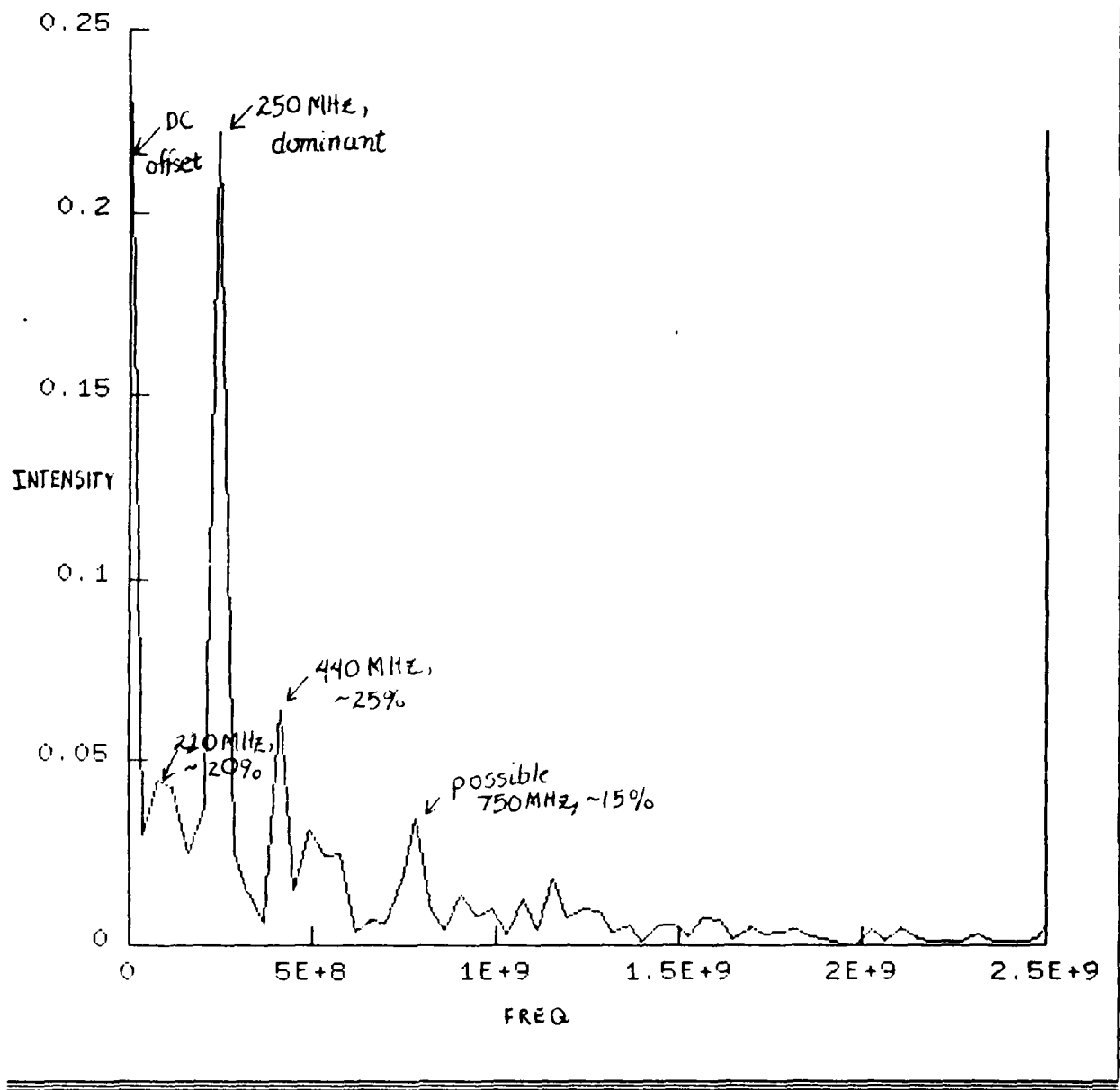


Figure 25(a). FFT of shot 4253, all frequencies

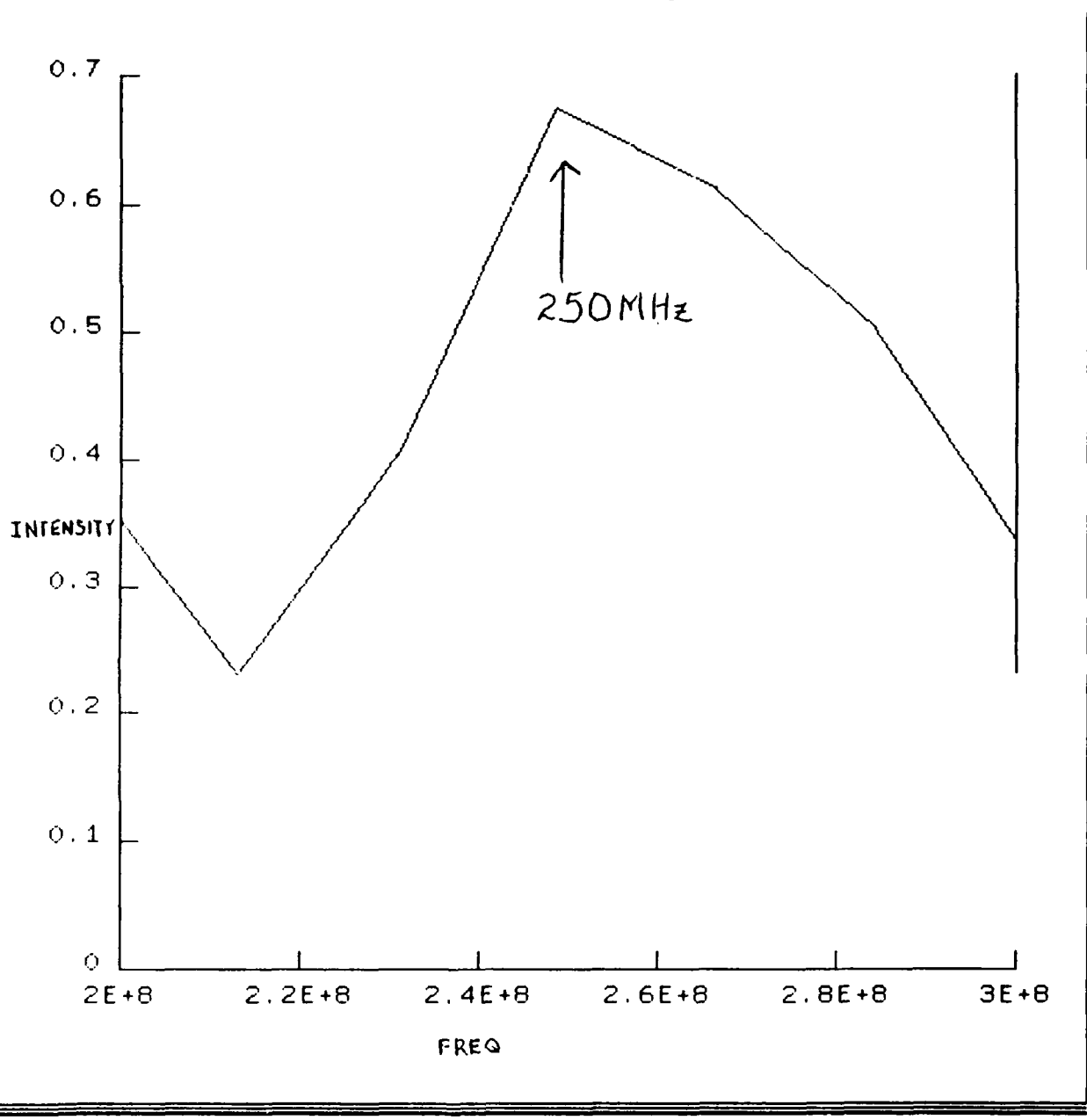
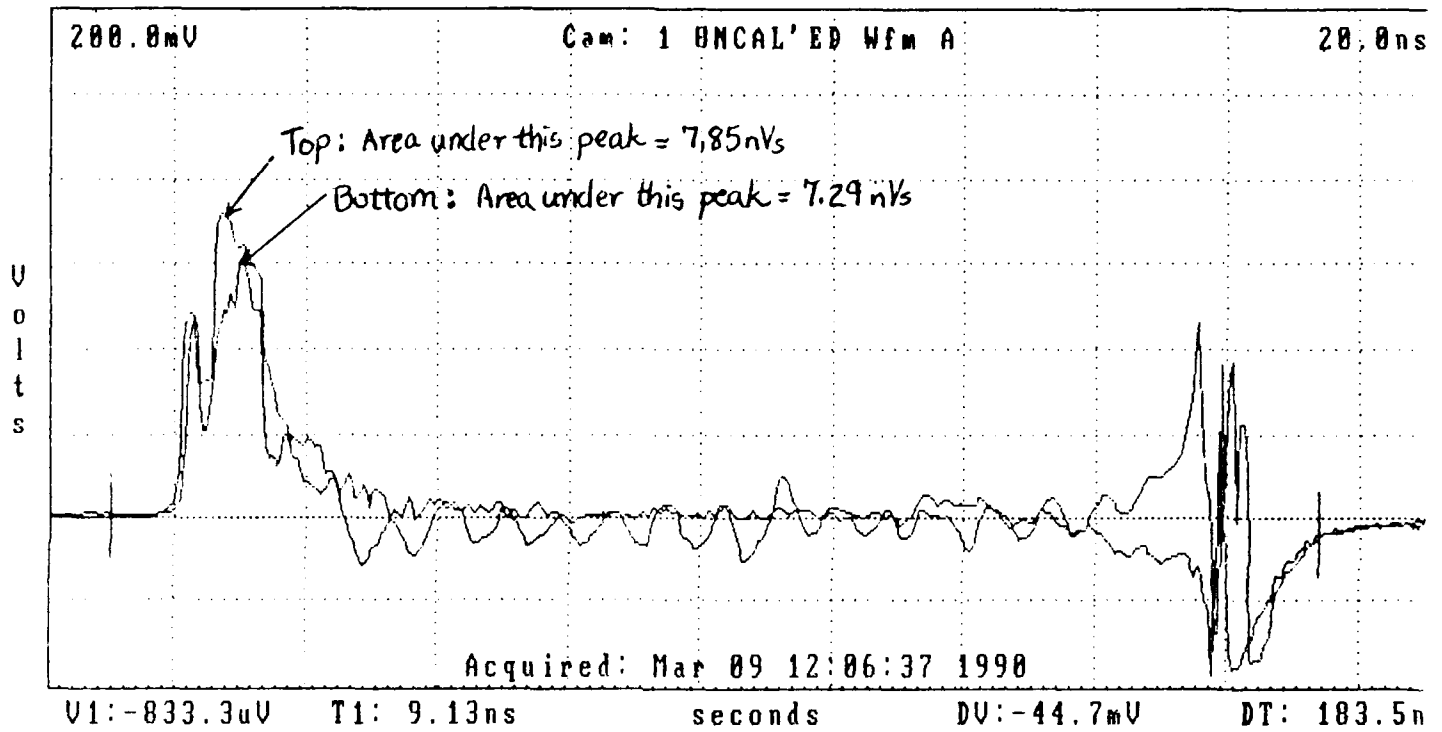


Figure 25(b). FFT of shot 4253, frequencies 200-300 MHz range

Non-steered ABR2 t, b ("A"=top, "B"=bottom)



$$\Delta y = \frac{R_0}{2} \left[ \frac{\int \Delta V_y}{\int \epsilon V_y} \right] = \frac{7.9 \text{ cm}}{2} \left[ \frac{(7.85 - 7.29) \text{ nVs}}{(7.85 + 7.29) \text{ nVs}} \right] = 0.15 \text{ cm}$$

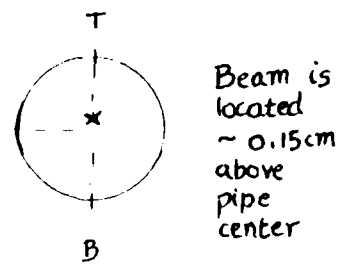
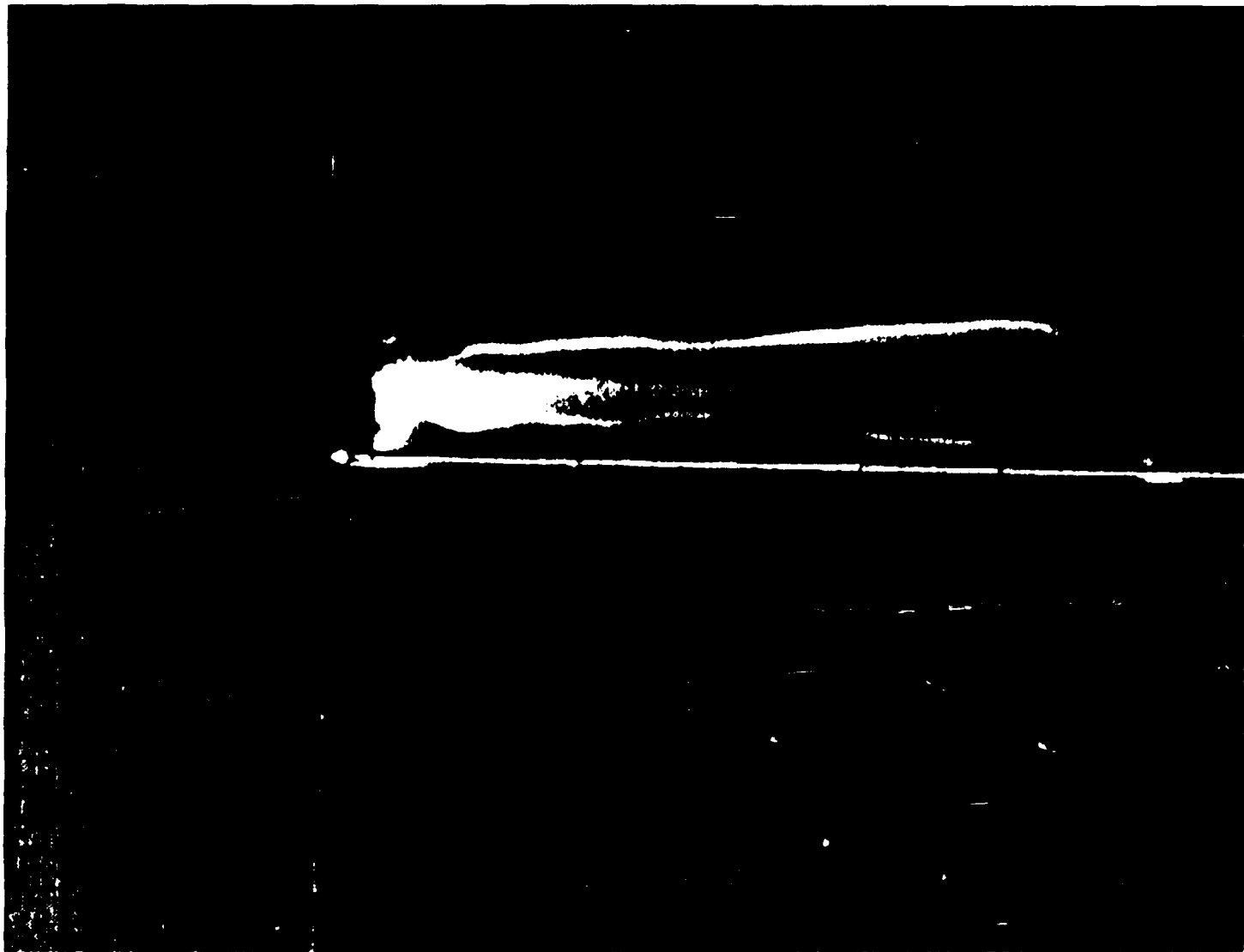


Figure 26(a). Nonsteered signal B-dot waveforms



4232 Nonsteering

At start, beam centroid is  $3.4\text{mm} \times 9.3\text{mag} \cong 3.2\text{ cm}$  above marker  
At end, beam centroid is  $4.0\text{mm} \times 9.3\text{mag} \cong 3.8\text{cm}$  above marker

Figure 26(b). Nonsteered signal streak camera photo

4234: A=Bottom, B=Top

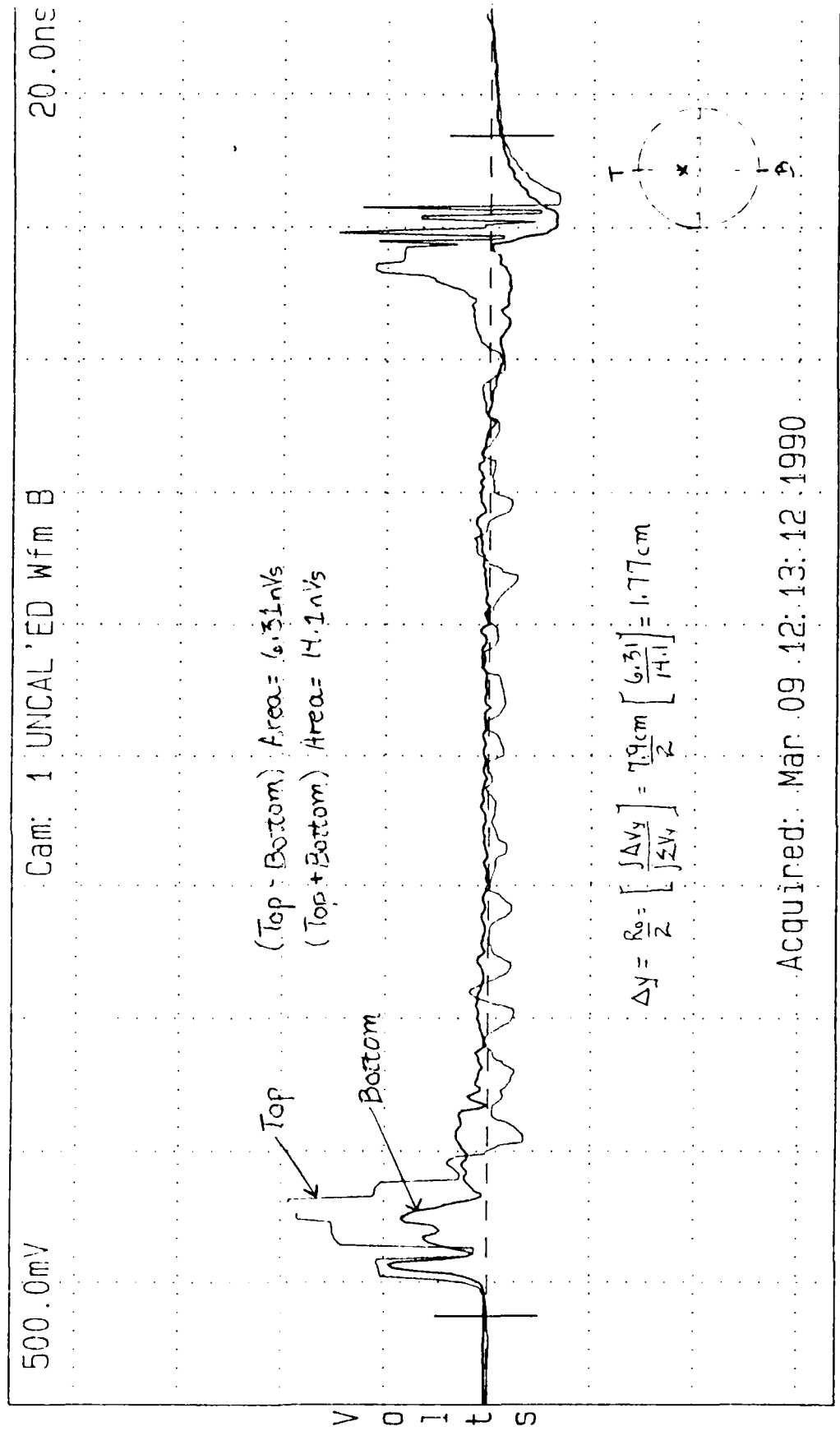
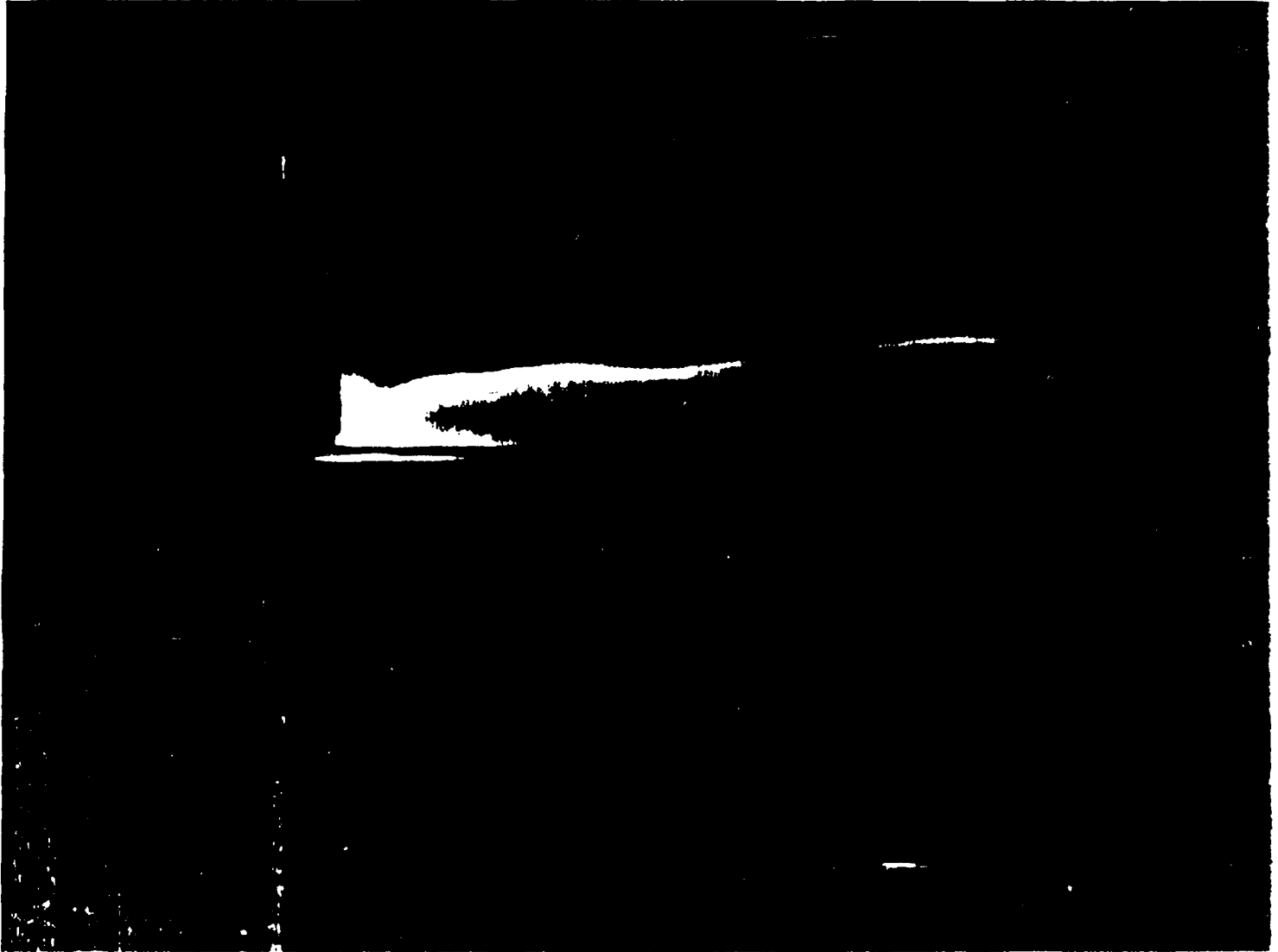


Figure 27(a). Top steered signal B-dot waveforms





4237 Steered toward top (+10A)

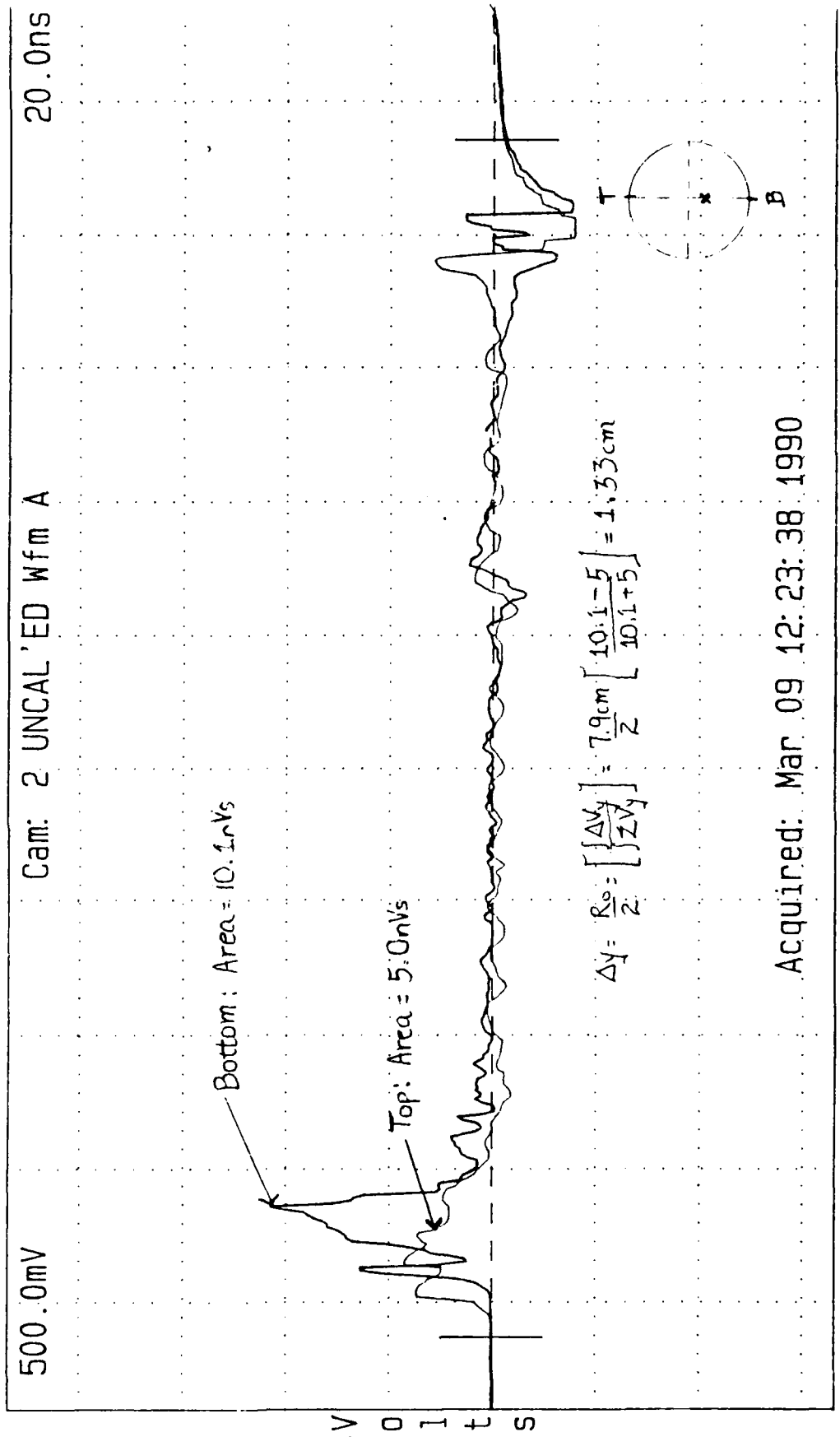
At start, beam centroid is  $2.0 \text{ mm} \times 9.3 \text{ mag} \approx 1.9 \text{ cm}$  above marker

At end, beam centroid is  $3.0 \text{ mm} \times 9.3 \text{ mag} \approx 2.8 \text{ cm}$  above marker

Avg movement during pulse =  $1.14 \text{ cm}$   
(comparing with shot 4232)

Figure 27(b). Top steered signal streak camera photo

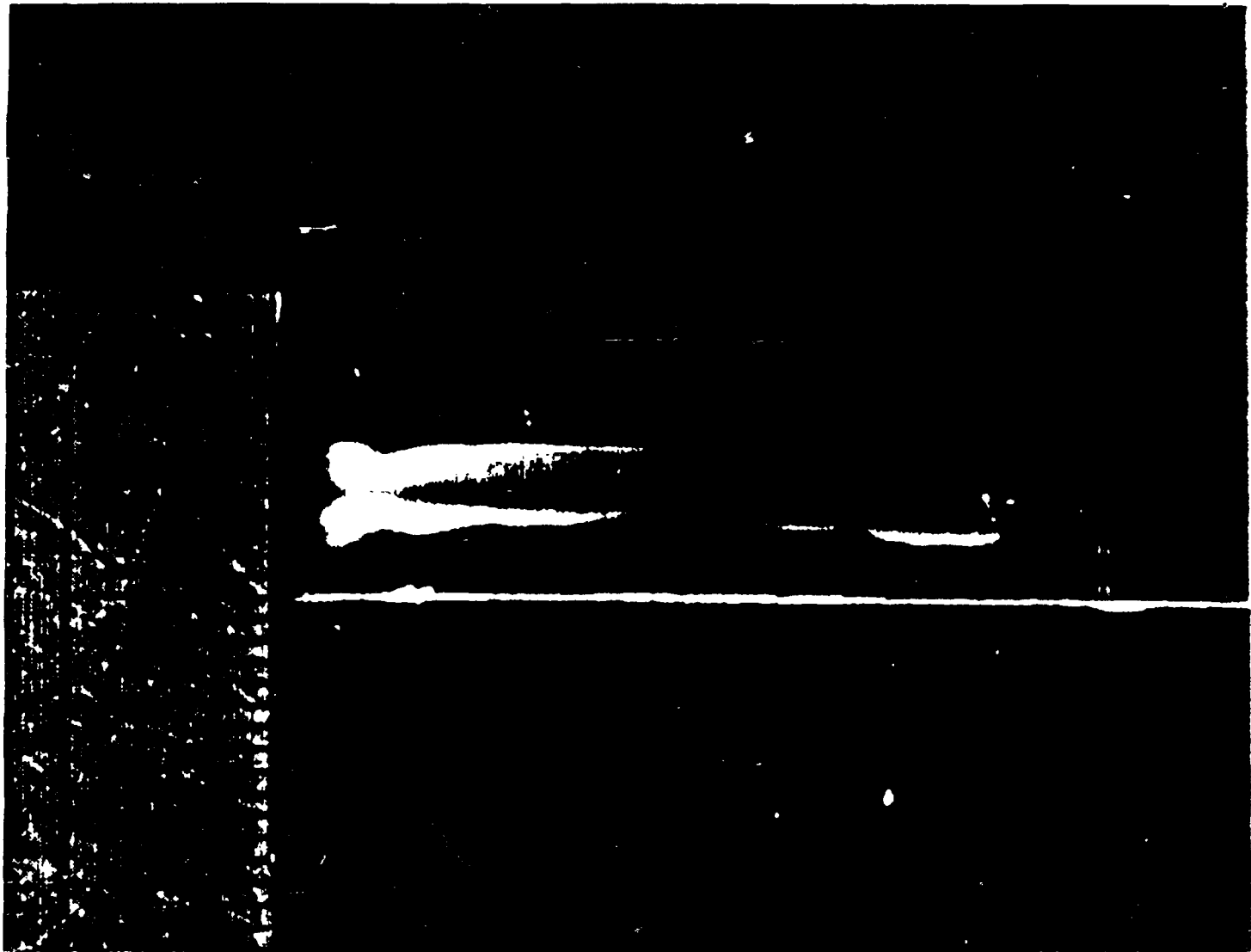
4238: A=Bottom. B=Top



Acquired: Mar 09 12:23:38 1990

V1: 2.49uV T1: 10.9ns seconds DV: -61.4mV DT: 179.6ns

Figure 28(a). Bottom steered signal B-dot waveforms



4238 Steered toward bottom (-10A)

Figure 28(b). Bottom steered signal streak camera photo

Streak camera photographs can provide quantitative information to  $\pm 5\%$  accuracy in frequency [Ref. 2:p. 1]. When B-dot oscillation frequencies are compared to streak camera/densitometer scan frequencies, the agreement is very good. See Table 4-2.

TABLE 4-2  
COMPARISON OF B-DOT AND STREAK CAMERA OSCILLATION FREQUENCIES

SHOT	B-DOT FREQ (MHZ)	STREAK CAMERA FREQ (MHZ)
4323	247.0	250
4253	246.0	250
4251	242.0	246

Figure 29(a) shows both the streak camera photograph of a shot and the B-dot waveforms. Figure 29(b) shows the microdensitometer analysis of the photograph, using VAX signal analysis and LOTUS plotting programs. The top and bottom beam envelopes are shown, plus exaggerated sum-difference curves that accentuate the magnitude of the beam oscillations. Figure 30 is a particularly well-aligned centered shot (4266) which very clearly shows the nature of the oscillations. In Figure 30(a), the streak camera photograph oscillations are barely visible; the B-dots show oscillations at the 240 MHz frequency, with one B-dot out of phase with respect to the other. Figure 30(b) is an expanded view of the oscillations.

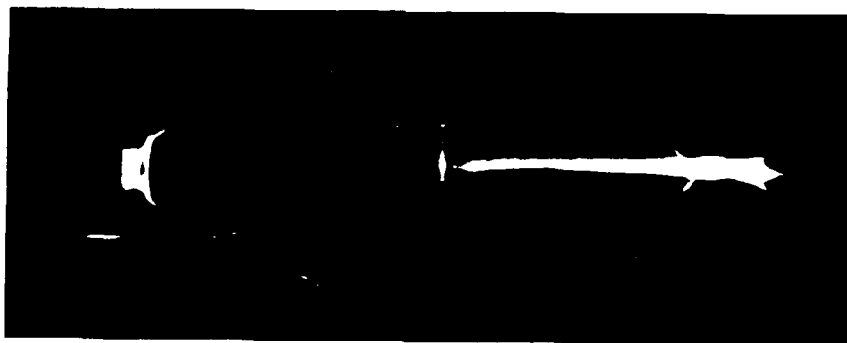
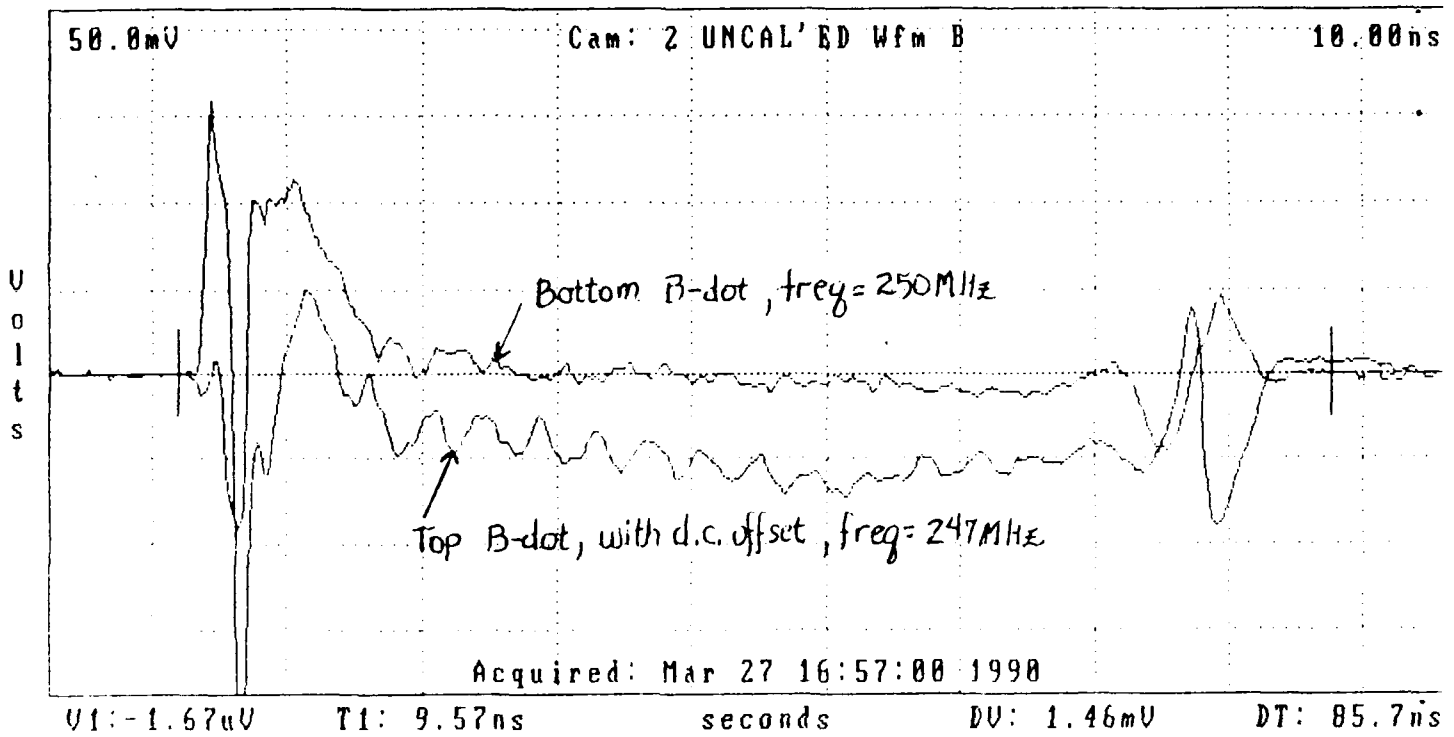


Figure 29(a). Shot 4323 streak camera photograph and B-dot waveforms

# 4323 Edges vs Time

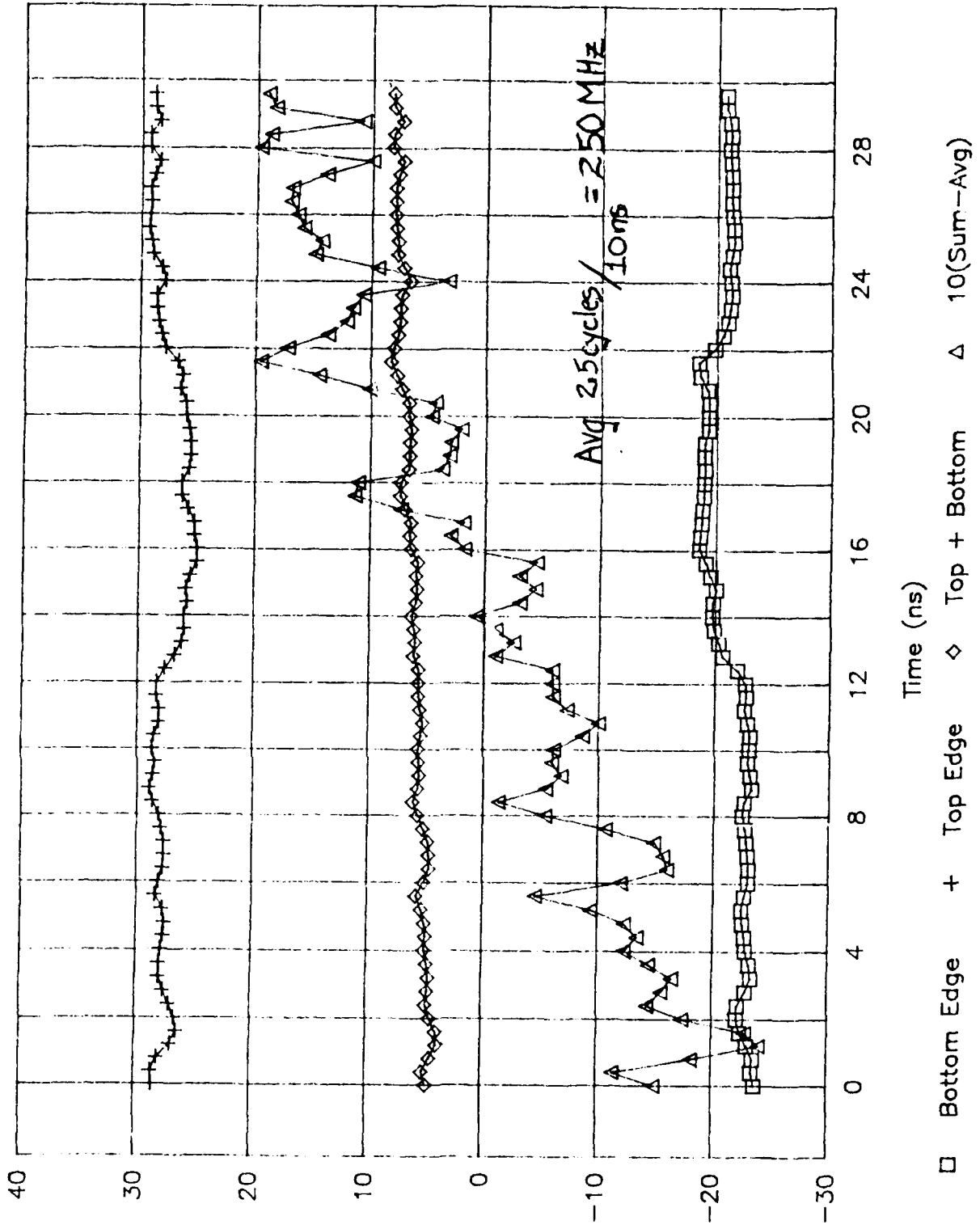


Figure 29(b). Shot 4323 microdensitometer analysis

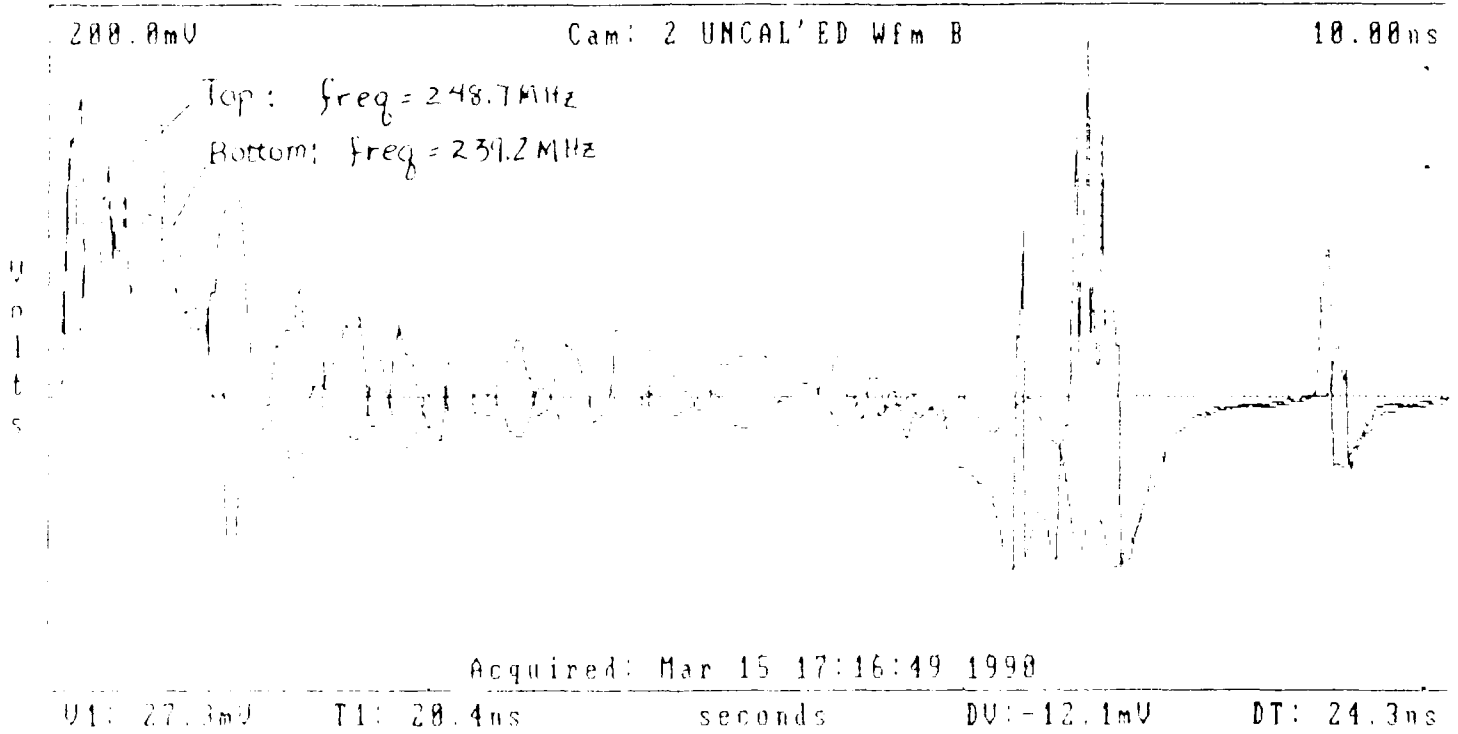
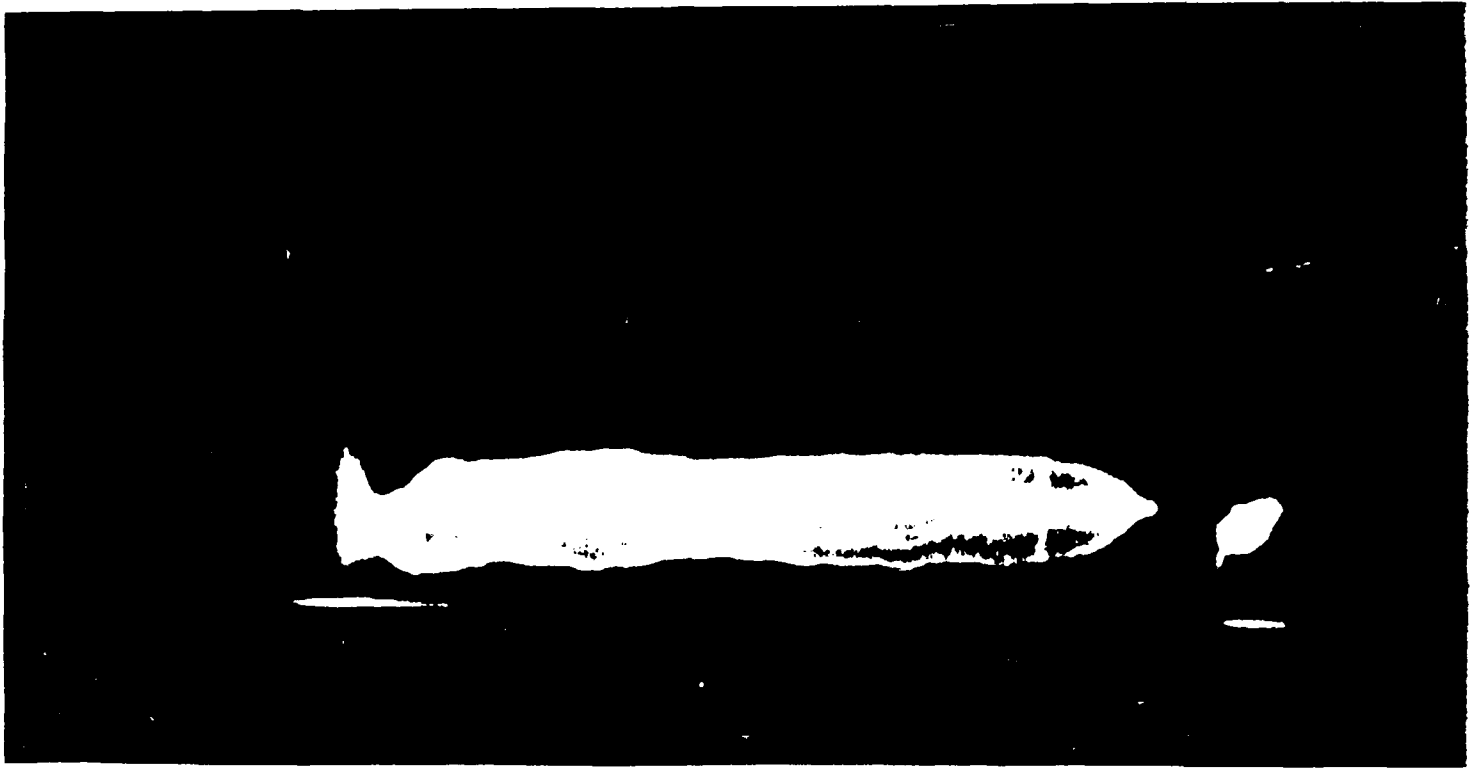


Figure (30a). Shot 4266 streak camera photograph and B-dot waveforms

4266 Expanded B-dots

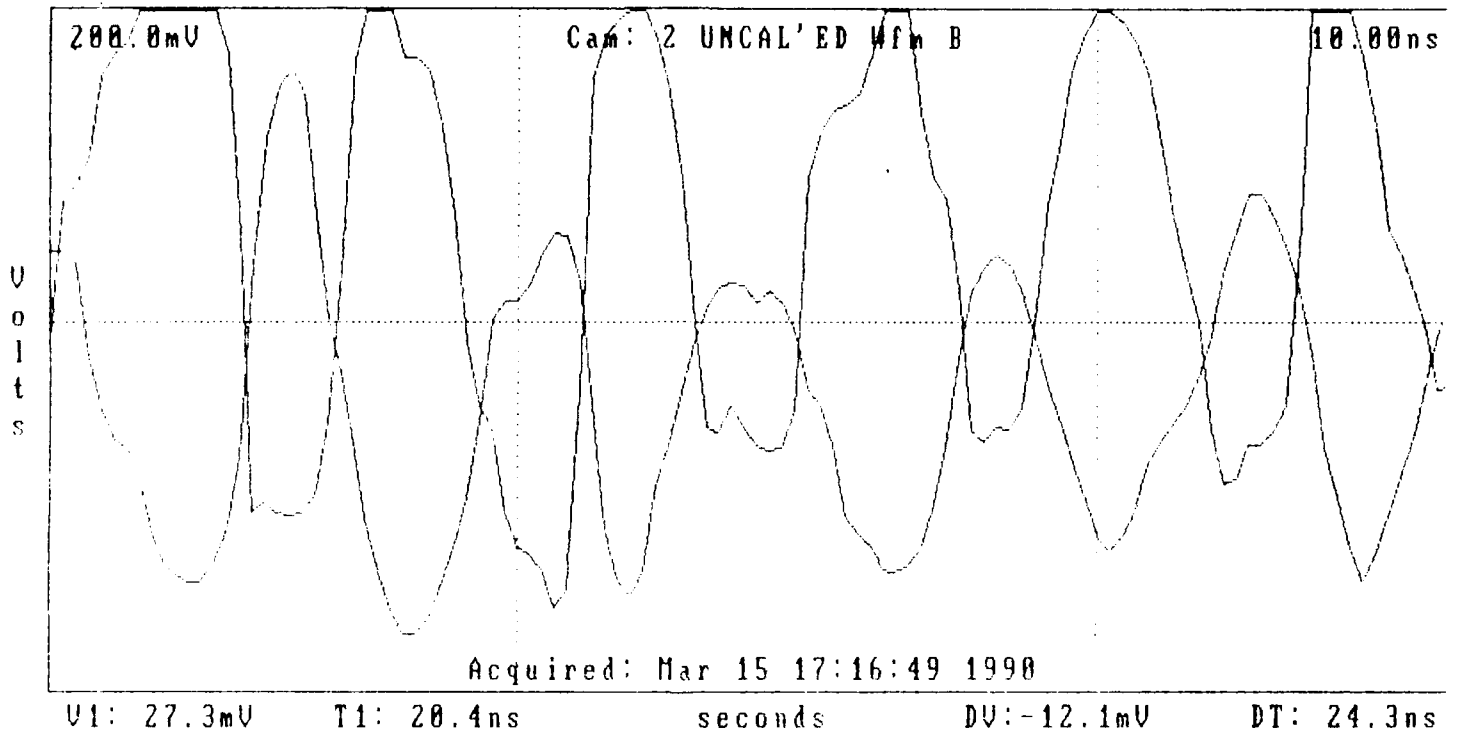
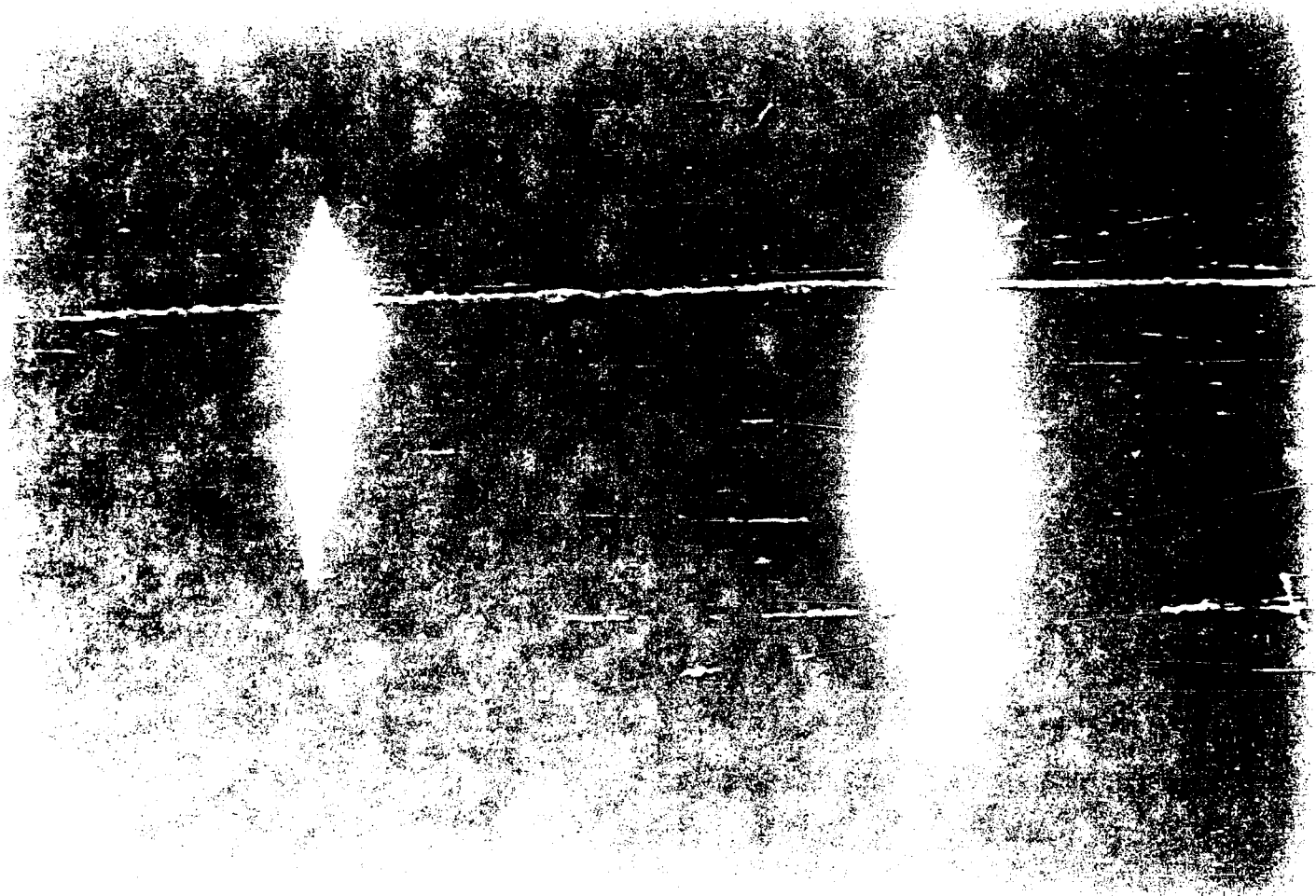


Figure 30(b). Expanded view of B-dot waveforms



This oscillation pattern corresponds to transverse beam oscillation, which is often produced by excited cavity dipole TE/TM modes [Ref. 6:p. D-10]. A possible reason for excitation of the cavity resonance modes is shown in Figure 31. This is a Polaroid photograph taken by a camera located at the left side of the REX diode, with a view of the cathode area (on the right) and anode area. No scintillator is present, so ideally, no light should be emitted during a shot. As the figure shows, however, light is being generated. The exact cause is unknown, but one possible reason is that the wide beam generated at lower (4 MV, 4 KA) power settings than used in previous experiments [Ref. 1:p. 3] is impacting the front surface and sides of the anode and anode channel (3 inches in diameter), causing plasma generation and emission of light. Should these emissions reflect back to the cathode area, causing more emissions, the result would be destabilization of the electron beam generated on the velvet cathode surface, possibly at periodicities related to cavity TE/TM modes.

The final calculation to be completed concerned the magnitude of beam oscillations. Equation 12 was used to compute oscillations for earlier shots, when the beam was not well-centered, and for the last several shots in the experiment, where the steering magnets and physical manipulation of the apparatus were used to center the beam as



much as possible. As shown in Table 4-3, the amplitude of oscillations was smaller for centered shots. (Oscillations were never completely eliminated during the time of the experiment, although previous higher beam power experiments had accomplished this [Ref. 6:p. D-1].)

TABLE 4-3  
MAGNITUDES OF TRANSVERSE BEAM OSCILLATIONS

SHOT	OSCILLATING AMPLITUDE (mm)
4232	1.6
4239	3.9
4238	3.5
4253	0.9
4266	0.2

Experimental error for the dynamic phase of the experiment was calculated by combination in quadrature of the following sources of error:

Computer software error	1%
Oscilloscope calibration error	1%
Camera digitization error	1%
B-dot port-to-port difference	1.28%
ANZAC four way adders	1%
MCL subtractors	1%
Streak camera	5%
Integrators	5%
REX experimental error	7.5%

## V. CONCLUSIONS

The B-dot sensor calibration experiments performed at Los Alamos National Laboratory in the summer of 1989 and the spring of 1990 were largely successful. They were designed to finalize the new B-dot sensor design requirements and to test the resulting sensor's performance on the REX electron beam using a streak camera as the independent sensor.

The preliminary experiment tested the Tektronix DCS B-dot signal collection and analysis software and certified it for use in the final experiment. The experiment determined that older B-dot sensor designs had an undesirably large port-to-port variation (~8 percent) and guided the design requirements for the new B-dot ring. As a result, the new ring contained ports with uniformly machined wire loops constructed of pin tabs, pins, wire, and 50 ohm resistors, with port-to-port variations on the order of 1.5 percent. It was determined that the beam pulse time required an increase to ~100 ns to enhance signal analysis. The preliminary experiment also began to identify factors that modified the shape of a B-dot signal and explored digital and mechanical methods of adding and subtracting signals. The final selection of computer digital data operations and passive adder-subtractor devices to be used in the calibration experiment was made with these results. The B-dot signals from this experiment were analyzed only

qualitatively, due to the large uncertainties and noise sources present.

The calibration experiment, also called the "current experiment," confirmed the excellent performance of the Tektronix DCS Version 2.06 software. The software's interface with Tektronix digitation cameras, oscilloscopes, and IBM personal computers, its ability to manipulate the data, and its visual data presentation options exceeded the requirements of the experiment. Passive voltage adder/divider devices were examined and their effects were calculated so they could be included in signal analysis. The new B-dot sensor ring was successfully calibrated on the test stand using the software to be able to accurately detect static transverse beam displacement (beam position) to a resolution of 0.25 millimeters within 2 percent experimental error. Port-to-port variations were found to be ~1 percent. The sources of experimental error, both for the test stand and the REX experimental area, were identified and quantified. The major individual sources of error for the test stand were oscilloscope calibration and camera digitization errors (both ~1 percent). The major sources of error for the dynamic (REX) phase included these plus the following errors: passive voltage devices (both 1 percent for each), B-dot port-to-port difference (~1 percent), streak camera (~5 percent), and integrators (~5 percent). Measured B-dot signals were compared to theoretical calculations to calculate B-dot loop area geometry correction factors for each port. The average loop area correction factor was 1.193.

In the dynamic (REX) phase of the calibration experiment, which was conducted with the REX beam experiencing both small amplitude transverse oscillations and beam centering displacement, the B-dots were found to provide oscillation and displacement data in good agreement with theoretical calculations and streak camera data. Noise sources were identified and eliminated. The beam centering (transverse static displacement) information provided by the B-dots for REX could be calibrated only to the resolution of the streak camera (0.5 millimeters), within a 7.5 percent experimental error. The small amplitude transverse beam oscillation frequencies detected by the B-dots were in excellent agreement with the streak camera data. This was true for both rough software calculations and more detailed Fourier analysis of the B-dot waveforms. Ability of the B-dots to detect the small amplitude oscillations and determine their frequency was calculated to be within 0.5 millimeters amplitude, and accurate in frequency, to within 7.5 percent experimental error. (The frequency range seen in the experiment, 240-250 MHz, was determined to be one of the REX diode cavity TE/TM dipole modes.)

The reason that the experiment was determined to be "largely successful" instead of "completely successful" is that the B-dot sensor is capable of finer resolution, particularly in determining the amplitude of small transverse beam oscillations, than that demonstrated in the experiment. However, the calibration standard (the streak camera) limited the determination of the absolute B-dot resolution. Beam oscillations with amplitudes on the order of

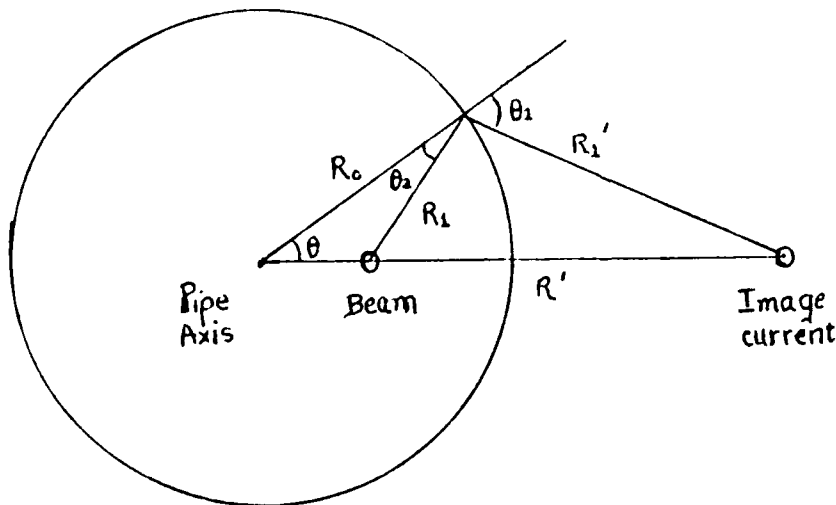
a millimeter were easily seen by both streak camera and the B-dots in the initial dynamic shots. In later shots, the beam was more correctly centered in the propagation pipe, and the oscillation amplitudes were reduced to a few tenths of a millimeter. The B-dots could still easily detect these, whereas the streak camera was at the limit of its resolving capability. What would have been highly desirable in the experiment would have been further reduction of the oscillation amplitudes to the point where they could no longer be detected by the streak camera, and then further reductions, until they could no longer be detected by the B-dots. In that manner, it would be possible to find out what the small amplitude beam oscillation detection ability of the B-dot really is, to within the experimental error determined by the experiment. (The beam oscillations were not reduced to less than a few tenths millimeters during the time of this experiment.)

Further experiments suggested include this systematic reduction of the REX beam transverse small amplitude oscillations, as well as periodic retesting of the B-dot sensors on the test stand to ensure long-term stability. It is also suggested that the effect which the small amount of radiation present during each REX shot has on the B-dot sensors (specifically the resistors) over large numbers of shots, be studied.

APPENDIX A  
EQUATIONS USED IN DATA ANALYSIS

I. ANALYSIS OF B-DOT LOOP PROBES

B-dot loop probes are used to monitor electron beam current, position, and stability for many machines using electron beams. They are non-intrusive to the propagating beam and are capable of making the required nanoseconds time frame beam measurements. The derivation summary presented here results in an expression for the magnetic field induced in a B-dot loop by an electron beam pulsing nearly through the axis of a cylindrical metal walled drift tube, including the contribution to the field of the return current in the wall of the conductive drift tube. See Figure A-1. [Ref. 8:pp. 1-5]



$$B_0 = \frac{\mu_0 I}{2\pi R_0}$$

$R_0$  = the radius

$\Delta R$  = displacement

$$\rho = \frac{\Delta R}{R_0}$$

$$R_1^2 = \bar{R}_1 \cdot \bar{R}_1$$

$$= (\bar{R}_0 - \Delta \bar{R}) \cdot (\bar{R}_0 - \Delta \bar{R})$$

$$= R_0^2 + \Delta R^2 - 2R_0 \Delta R \cos \theta$$

$$= R_0^2 \left( 1 + \frac{\Delta R^2}{R_0^2} - \frac{2\Delta R \cos \theta}{R_0} \right)$$

$$R_1^2 = R_0^2 \cdot (1 + \rho^2 - 2\rho \cos \theta)$$

Figure A-1.

Similarly,

$$97 \quad (R_1')^2 = (R')^2 (1 + \rho^2 - 2\rho \cos \theta)$$



The image current is placed in a position ( at  $R' = \frac{R_0^2}{\Delta R}$  ) that will satisfy the boundary condition  $B_{\text{perp}} = 0$  on the surface of the cylindrical drift tube. It is equal to and opposite to the net beam current. The result is that normal components of B from the net beam current and the image current cancel. Only the tangential magnetic field components will, therefore, be calculated. (Primed quantities denote contributions from the image current.)

$$\begin{aligned} B' \text{ tang} &= \cos \theta_1 \frac{B_0 R_0}{R_1'} \\ &= \frac{B_0 R_0^2}{R_1^2} (\rho \cos \theta - \rho^2) \end{aligned} \quad (\text{A-1})$$

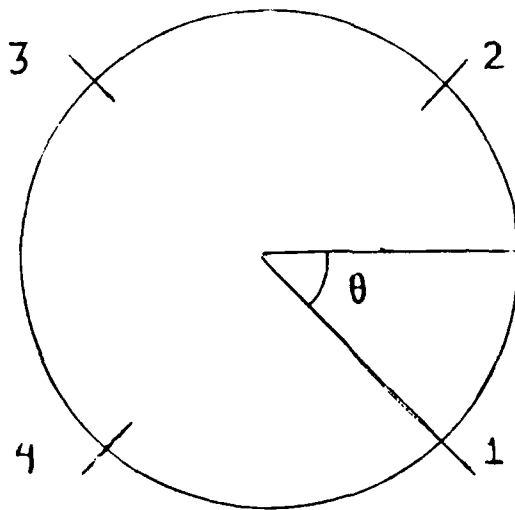
$$\begin{aligned} B \text{ tang} &= \cos \theta_2 \frac{B_0 R_0}{R_1} \\ &= \frac{B_0 R_0^2}{R_1^2} (1 - \rho \cos \theta) \end{aligned} \quad (\text{A-2})$$

$$\begin{aligned} B = B \text{ tang} + B \text{ tang}' &= \frac{B_0 R_0^2 (\rho \cos \theta - \rho^2) + B_0 R_0^2 (1 - \rho \cos \theta)}{R_1^2} \\ &= \frac{B_0 R_0^2 (\rho \cos \theta - \rho^2 + 1 - \rho \cos \theta)}{R_0^2 (1 + \rho^2 - 2\rho \cos \theta)} \\ B &= \frac{B_0 (1 - \rho^2)}{(1 + \rho^2 - 2\rho \cos \theta)} \end{aligned} \quad (\text{A-3})$$

Approximation to first order in  $\rho$  :

$$B \cong B_0 (1 + \rho \cos \theta + \dots) \quad (\text{A-4})$$

Using the Equation 4 result, four B-dot loops are positioned as shown in Figure A-2:



Loop	Angle
1	$\theta$
2	$\pi/2 - \theta$
3	$\pi - \theta$
4	$\pi/2 + \theta$

Fig. A-2

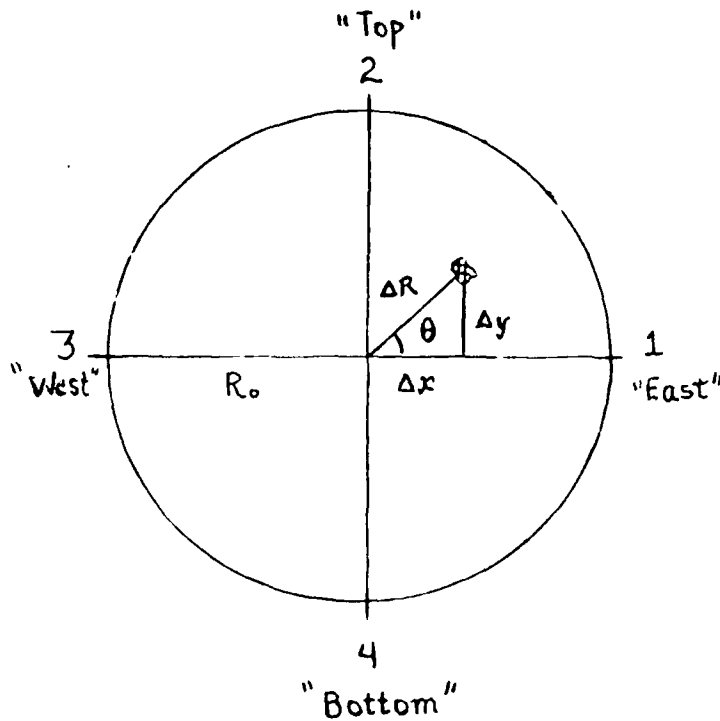
$$B_1 \cong B_0(1 + 2\rho \cos \theta) \quad (\text{A-5})$$

$$B_2 \cong B_0(1 + 2\rho \sin \theta) \quad (\text{A-6})$$

$$B_3 \cong B_0(1 - 2\rho \cos \theta) \quad (\text{A-7})$$

$$B_4 \cong B_0(1 - 2\rho \sin \theta) \quad (\text{A-8})$$

II. ANALYSIS OF ELECTRON BEAM DISPLACEMENT, CURRENT, AND OSCILLATION (STABILITY) USING B-DOT LOOP PROBES



$$\rho = \frac{\Delta R}{R_0}$$

$$\Delta R \cos \theta = \Delta x, \Delta R \sin \theta = \Delta y$$

$A = \text{loop area}$

$$B_1 = \frac{\mu I}{2\pi R_0} (1 + 2\rho \cos \theta) = B_0 \left( 1 + 2 \frac{\Delta x}{R_0} \right)$$

$$B_2 = \frac{\mu I}{2\pi R_0} (1 + 2\rho \sin \theta) = B_0 \left( 1 + 2 \frac{\Delta y}{R_0} \right)$$

$$B_3 = \frac{\mu I}{2\pi R_0} (1 - 2\rho \cos \theta) = B_0 \left( 1 - 2 \frac{\Delta x}{R_0} \right)$$

$$B_4 = \frac{\mu I}{2\pi R_0} (1 - 2\rho \sin \theta) = B_0 \left( 1 - 2 \frac{\Delta y}{R_0} \right)$$

$$B_0 = \frac{\mu I}{2\pi R_0} \quad (\text{from Ampere's Law})$$

$$V_{\text{TOT}} = V_1 + V_2 + V_3 + V_4$$

### A. SUMMED SIGNAL EXPRESSIONS

First, a sum of two or more probe signals will yield the beam current: if probes 1 through 4 are summed:

$$\sum_1^4 B = B_0[1+2\rho\cos\theta+1-2\rho\cos\theta+1+2\rho\sin\theta+1-2\rho\sin\theta] = 4B_0 \quad (\text{A-9})$$

Now, using Faraday's Law; EMF induced during a pulse (per unit length)  $= dV = \frac{-\partial\Phi}{\partial t}$

$$= \frac{-\partial(BA)}{\partial t}; \quad A = \text{area} \quad \frac{dV}{A} \equiv -dB, \quad \int_0^V \frac{dV}{A} = -\int_0^B dB, \quad V = \frac{-A\mu}{2\pi R_0} \frac{dI}{dt}$$

the above expression (A-9) for the sum of B fields can be converted to an expression for the sum of voltages, which are now measured quantities:

$$V_1 = \frac{-\mu I A}{2\pi R_0} (1+2\rho\cos\theta) \text{ from probe 1}$$

$$V_{TOT} = \sum_1^4 V = \frac{-4\mu A}{2\pi R_0} \frac{dI}{dt} \text{ from all four probes; } \quad \frac{dI}{dt} = \frac{-2\pi R_0}{4A\mu} V_{TOT}$$

Since both I and V change during the time of the pulse,

$$I(t) = \frac{-2\pi R_0}{4\mu A} \int \sum V_{TOT}(t) dt \quad (\text{A-10})$$

To obtain an expression for I(t) that averages out all probe variations, the voltage signals for all four probes are used in the sum expression. However, it is possible to derive an expression for the current sensed by two opposed probes which is particularly useful for the test stand. If probes 1 and 3 are summed:

$$\sum V_x = \frac{-\mu A}{2\pi R_0} \frac{dI}{dt} \left[ 1 + \frac{2\Delta X}{R_0} + \frac{(1-2\Delta X)}{R_0} \right]$$

$$= \frac{-\mu A}{2\pi R_0} \frac{dI}{dt} (2) = \frac{-\mu A}{2\pi R_0} \frac{dI}{dt}$$

$$dI = \frac{-\pi R_0}{\mu A} \sum V_x dt$$

$$I = \frac{-\pi R_0}{\mu A} \int \sum V_x dt \quad \text{current from two B-dots}$$

(The oscilloscope readouts that comprise  $\Sigma V_x$  and other voltage expressions can be made negative or positive as desired by flipping an "inversion" switch on the appropriate oscilloscope amplifier module. This is why the negative signs may not appear in the portions of this paper where B-dot signals are mathematically analyzed.)

The current senses by only B-dot probe (again, a useful expression for measuring B-dot responses on the test stand)

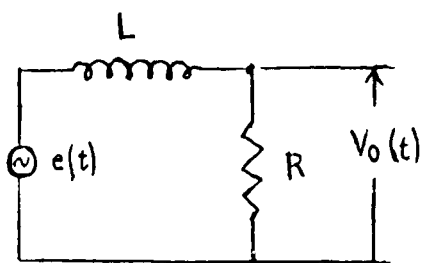
is:

$$V_1 \text{ or } V_3 = \frac{-A\mu}{2\pi R_0} \frac{dI}{dt} \left( 1 \pm \frac{2\Delta X}{R_0} \right) \quad \text{current from one B-dot}$$

If the B-dot ring is centered as closely as possible on the test stand, then  $\Delta x$  is the centering measuring error, 0.01 inch, and  $R_0$  is the radius out to the middle of the loop area from the center of the test stand, 3.111 inch; and the last equation becomes:

$$V_1 \text{ or } V_3 = \frac{-A\mu}{2\pi R_0} \frac{dl}{dt} \left( 1 \pm \frac{(2)(.01)''}{3.111''} \right) = \frac{-\mu A}{2\pi R_0} \frac{dl}{dt} (1 \pm 0.0064) \quad (\text{A-11})$$

The B-dots used in the  $V_{\text{tube}}$  probes are equipped with passive integrators which contain inductors. The expression for voltage in these B-dots is derived from the circuit differential equation as shown (calculation by R. Carlson of LANL):



$$e(t) = \frac{L di(t)}{dt} + V_0(t)$$

$$i(t) = \frac{V_0(t)}{R}$$

$$e(t) = \frac{L}{R} \frac{dV_0(t)}{dt} + V_0(t)$$

$$e(t) = \frac{-d}{dt} [\text{BA}] = \frac{-\mu A}{2\pi R} \frac{dl}{dt}$$

$$\frac{L}{R} = \tau$$

$$\frac{dV_0(t)}{dt} = \frac{e(t)}{\tau} - \frac{1}{\tau} V_0(t)$$

$$V_0(t) = \frac{1}{\tau} \int e(t) dt - \frac{1}{\tau} \int V_0(t) dt$$

$$V_0(t) = \frac{1}{\tau} \frac{\mu_0 A}{2\pi R} I(t) - \frac{1}{\tau} \int V_0(t) dt \quad (\text{A-12})$$

An excellent and accurate calculation of beam current can be calculated using the experimentally verified non-linear dependence of diode current on the voltage across the diode gap. This dependence closely follows the Child-Langmuir Law, which is:

$$I_{\text{diode}} = \text{Perveance} \times V_{\text{diode}}^{3/2}$$

where the perveance ( $\mu$  pervs) is a constant of the diode geometry. For the 2.5 inch diameter velvet cathode and REX parameters [Ref. 1:pp. 59-61]:

$$I = 0.514V_d^{\frac{3}{2}} \quad (\text{A-13})$$

#### B. DIFFERENCED SIGNALS EXPRESSIONS

Second, expressions for the position of the beam can be derived from the difference of measurements of two or more probes: specifically for the x-direction, if probes 1 and 3 are differenced,

$$\Delta B_x = B_0[1 + 2\rho \cos \theta - (1 - 2\rho \cos \theta)]$$

$$= B_0[4\rho \cos \theta] = 4B_0 \frac{\Delta R \cos \theta}{R_0}$$

$$\Delta B_x = 4B_0 \frac{\Delta x}{R_0}$$

$$\Delta B_x = \frac{4\mu I}{2\pi R_0} \left( \frac{\Delta x}{R_0} \right)$$

$$\Delta V_x = \frac{-4A\mu}{2\pi R_0} \left( \frac{\Delta x}{R_0} \right) \left( \frac{2\pi R_0 V_{TOT}}{4A\mu} \right) = \frac{\Delta X V_{TOT}}{R_0}$$

$$\Delta x = \frac{R_0 \Delta V_x}{V_{TOT}} = R_0 \left( \frac{V_1 - V_3}{V_{TOT}} \right)$$

Similar, for the y direction:

$$\Delta y = \frac{R_0(V_2 - V_4)}{V_{TOT}}$$

(static displacement expressions for  $\Delta x$  and  $\Delta y$  using sum of voltages of all four probes)

For a two-probe difference using the sum of voltages only for those two probes:

$$\Delta V_x = \frac{-\mu A}{2\pi R_0} \frac{dl}{dt} \left[ 1 + \frac{2\Delta x}{R_0} - \left( 1 - \frac{2\Delta x}{R_0} \right) \right] = \frac{-\mu A}{2\pi R_0} \frac{dl}{dt} \frac{4\Delta x}{R_0}$$

$$\Delta V_x = \frac{-\mu A}{2\pi R_0} \left( \frac{4}{R_0} \right) \frac{dl}{dt} [I\Delta X]$$

If  $\Delta x$  is a constant, as on the test stand, the last equation becomes:

$$\Delta V_x = \frac{-\mu A}{2\pi R_0} \left( \frac{4}{R} \right) \Delta x \frac{dl}{dt} \quad (\text{A-14})$$

An expression to substitute for  $\frac{dl}{dt}$  is obtained: from the

equation:  $dl = \frac{-\pi R_0}{\mu A} \sum V_x dt,$

$$\sum V_x = \frac{-\mu A}{2\pi R_0} \frac{dl}{dt}, \frac{dl}{dt} = \frac{-\pi R_0}{\mu A} \sum V_x$$

Equation A-14 becomes:

$$\int \Delta V_x = \frac{-\mu A}{2\pi R_0} \left( \frac{4}{R_0} \right) \Delta x \left( \frac{-\pi R_0}{\mu A} \int \sum V_x \right)$$

$$\int \Delta V_x = \frac{2}{R_0} \Delta x \int \sum V_x$$

$$\Delta x = \frac{R_0}{2} \frac{\int \Delta V_x dt}{\int \sum V_x dt} \quad (\text{A-15})$$

(static displacement in x-direction using information from 2 probes)



Equation A-15 can also be expressed in terms of an increment in voltage seen by a probe if the beam, or the test stand current line is moved closer to one probe. With  $E =$  increment in voltage,

$$\begin{aligned}\Delta x &= \frac{R_0}{2} \frac{\int \Delta V_x}{\int \sum V_x} = \frac{R_0}{2} \int \left[ \frac{V(1+\epsilon) - V(1-\epsilon)}{V(1+\epsilon) + V(1-\epsilon)} \right] \\ &= \frac{R_0}{2} \int \frac{2V\epsilon}{2V} \\ \Delta x &= \frac{R_0}{2} \epsilon\end{aligned}\tag{A-16}$$

Thus far, it has been assumed that there are no error contributions from cables, connectors, oscilloscopes or other electronic devices; and a passive adder/divider has not been considered for placement in the circuit. These factors can be considered as follows:

In manufacturer's catalogs, the passive adder/divider port-to-port imbalance, or difference in voltage out from one port compared to the voltage out of another port is listed in dB. This can be converted to a convenient expression in terms of the port voltages.

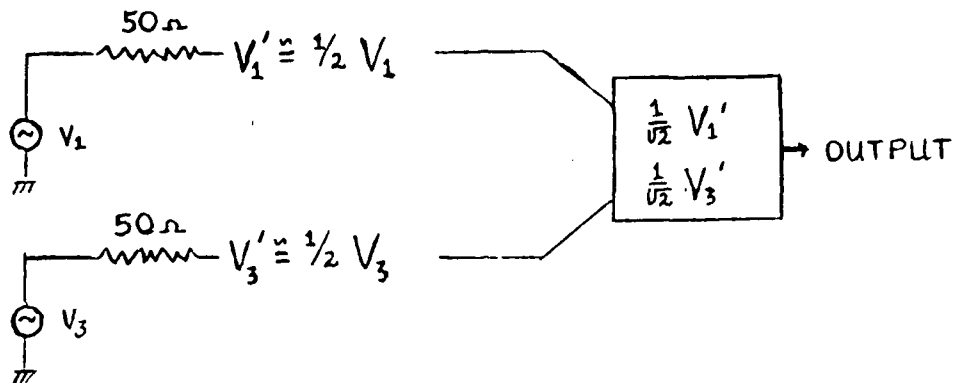
Catalog listing for MCL device imbalance = 0.1dB

$$0.1\text{dB} = 20 \log_{10} \left( \frac{V'}{V} \right), \quad \frac{0.1}{20} = \log_{10} \left( \frac{V'}{V} \right) \quad \begin{array}{l} v' \text{ is voltage out of one} \\ \text{port, } V \text{ is voltage out of} \\ \text{other port} \end{array}$$

$$10^{\frac{0.1}{20}} = \frac{V'}{V} = 1.0116$$

$$\text{Imbalance error} = \frac{1}{2}(0.0116) \approx 0.006.$$

A simplified circuit drawing of a passive adder/divider with two input ports is shown:



OUTPUT for divider from two 50 ohm B-dots:

$$\begin{aligned} \Delta V_x &= \frac{1}{\sqrt{2}}(V_1^1 - V_3^1) = \frac{1}{\sqrt{2}} \left[ \frac{1}{2} V_1 - \frac{1}{2} V_3 \right] \\ &= \frac{1}{2\sqrt{2}} [V_1 - V_3] \end{aligned} \quad (\text{A-17})$$

OUTPUT for adder from two 50 ohm B-dots:

$$\sum V_x = \frac{1}{2\sqrt{2}} (V_1 + V_3) \quad (\text{A-18})$$

OUTPUT for four-way adder from four 50 ohm B-dots:

$$\sum V_{TOT} = \frac{1}{4} [V_1 + V_2 + V_3 + V_4]$$

OUTPUT for four-way adder from four wire B-dots:

$$\sum V_{TOT} = \frac{1}{2} [V_1 + V_2 + V_3 + V_4]$$

If the B-dots are pure wires with no resistors; there is no halving of their voltage by the 50 ohm, and these equations become:

OUTPUT for divider from two wire B-dots:

$$\Delta V_x = \frac{1}{\sqrt{2}}[V_1 - V_3]$$

OUTPUT for adder from two wire B-dots:

$$\sum V_x = \frac{1}{\sqrt{2}}[V_1 + V_3]$$

OUTPUT for four-way adder with wire B-dots:

$$\sum V_{TOT} = \frac{1}{\sqrt{2}}[V_1 + V_2 + V_3 + V_4]$$

Similarly, if passive adder/divider devices are used, many previous expressions incorporating  $\Delta V$  and  $\Sigma V$  must be modified. Two such expressions are shown:

$$\frac{dI}{dt} = \frac{-\pi R_0}{\mu A} \sum V_x \quad \text{becomes}$$

$$\frac{dI}{dt} = \frac{-\pi R_0}{\mu A} \frac{1}{2\sqrt{2}}(V_1 + V_3)$$

$$V_1 + V_3 = \frac{-2\sqrt{2}\mu A}{\pi R_0} \frac{dI}{dt}$$

if integrate to obtain I,

$$I = \frac{\pi R}{2\sqrt{2}\mu A} \int (V_1 + V_3) dt \quad \text{current from 2 50 ohm B-dots using a passive adder}$$

Equation A-10 becomes:

current from four 50 ohm B-dots with 4-way adder:

$$I(t) = \frac{-2\pi R_0}{4\mu A} \left[ \frac{1}{2\sqrt{2}} \int (V_1 + V_2 + V_3 + V_4) dt \right] = \frac{-\pi R_0}{4\sqrt{2}\mu A} \int (V_1 + V_2 + V_3 + V_4) dt \quad (\text{A-19})$$

### C. OSCILLATING BEAM EXPRESSIONS

Expressions for transverse oscillation of the beam are derived through Equation A-20.

$$\Delta V_x = \frac{-\mu A}{2\pi R_0} \frac{4}{R_0} \frac{d}{dt} [I\Delta x] \quad (\text{A-20})$$

Past experiments with the streak camera have shown that transverse oscillation is sinusoidal. A series of assumptions using cosine functions lead to the following expressions:

If  $\Delta X = \text{sinusoidal} = \Delta X_0 \cos \omega t$ , movement with a single frequency, and  $I = \text{constant}$ , (20) becomes

$$\Delta V_x = \frac{-\mu A}{2\pi R_0} \frac{4}{R_0} \frac{d}{dt} [\Delta X_0 \cos \omega t] = \frac{\mu A 4 I \omega \Delta X_0 \sin \omega t}{2\pi R_0^2}$$

$$|\Delta V_x| = \frac{\mu A 4 I \omega \Delta X_0}{2\pi R_0^2}$$

$$\Delta X_0 = \frac{2\pi R_0^2}{4\mu A I \omega} |\Delta V_x| = \frac{2\pi R_0^2}{4\mu A I (2\pi f)} |\Delta V_x|$$

$$\Delta X_0 = \frac{R_0^2}{4\mu A I f} |\Delta V_x| \quad (\text{A-21})$$

Equation A-21 can be stated in terms of  $\Delta R_0$  instead of  $\Delta X_0$  or  $\Delta Y_0$ :

$$\Delta R_0 = d = \sqrt{\Delta X_0^2 + \Delta Y_0^2}$$

$$d = \frac{R_0^2}{4\mu A I f} \left[ |\Delta V_x|^2 + |\Delta V_y|^2 \right]^{\frac{1}{2}} \quad (\text{A-22})$$

Passive adder/divider versions of these expressions are:

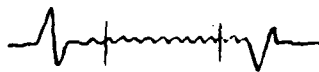
$$\Delta X_0 = \frac{R_0^2}{4\mu A I f} \frac{1}{2\sqrt{2}} |(V_1 - V_3)|$$

(magnitude of sinusoidal movement in x direction using two 50 ohm B-dots with passive divider)

$$d = \frac{R_0^2 \left[ |V_1 - V_3|^2 + |V_2 - V_4|^2 \right]^{\frac{1}{2}}}{4\mu A I f 2\sqrt{2}}$$

(magnitude of radial sinusoidal movement using two sets of two 50 ohm B-dots with two passive divider)

Equation A-21 contained the assumption that beam motion (transverse dipole oscillation) occurs at a single frequency. For more accuracy, the assumption should instead be made that the oscillation frequency is the superposition of several different frequencies. Indeed, the diode cavity has several predominant resonant dipole frequencies for a selected pulse width. For a typical voltage difference signal, with appearance;



the center portion of the signal contains the beam dipole oscillation information. Taking the power spectrum of the digitized center portion of the signal is done using the short VAX IDL program included in Appendix E. Selection of the predominant oscillation frequencies, and weighting each as indicated by the power spectrum will result in a more accurate version of Equation 21:

$$\delta = \frac{R_0^2}{4A\mu I} \left[ |\Delta V_x|^2 + |\Delta V_y|^2 \right]^{\frac{1}{2}} \sum_{i=1}^n \frac{1}{a_i f_i} \quad (\text{A-23})$$

where I = total current of the  
 electron beam for  
 that pulse  
 = radial displacement  
 of the beam from the  
 propagation axis  
 $R_0$  = radius of the B-dot  
 ring  
 A = effective area of the  
 B-dot loop  
 $\Delta V_x, \Delta V_y$  = differenced signals  
 ( $V_1 - V_3$ ), ( $V_2 - V_4$ )  
 $a_i$  = weighting factor for  
 a specific frequency  
 $f_i$  = specific component  
 frequencies of the  
 transverse beam  
 motion

### III. CALCULATIONS FOR REX LAMBERTSON STEERING MAGNETS

This calculation was performed on 9 March 1990 by M. Burns of Los Alamos Group M-4 [Ref. 12:pp. 1-2].

Beam energy 3.2 MeV

Distance from magnet to streak camera scintillator = 100cm

Beam rigidity: 
$$B\rho = \frac{3.3356}{q} \left[ 2m_0c^2E + E^2 \right]^{\frac{1}{2}} \quad (\text{kG}\cdot\text{cm})$$

$$= 3.3356 \left[ 2(0.51\text{MeV})(3.2\text{MeV}) + (3.2\text{MeV})^2 \right]^{\frac{1}{2}} = 12.26 \text{ kG}\cdot\text{cm}$$

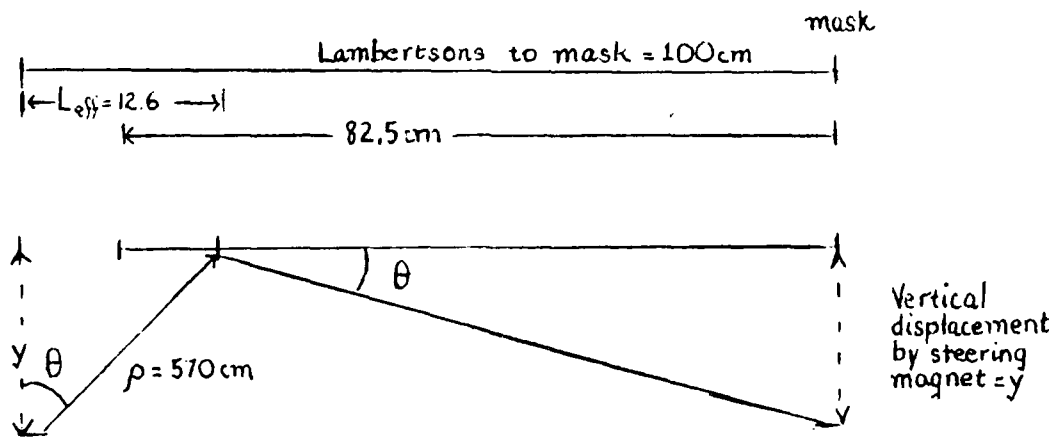
Peak field on axis, from Lambertson magnetic measurements:

$$B_{\text{max}} = 2.15\text{G}$$

Effective length:

$$L_{\text{eff}} = \frac{\int \vec{B} \cdot d\vec{l}}{B_{\text{max}}} = \frac{270\text{G}\cdot\text{cm}}{21.56} \quad (\text{Measurement})$$

$$= 12.6\text{cm}$$



$$\rho = \frac{B\rho}{B_{\text{max}}} = \frac{12.26\text{kG}\cdot\text{cm}}{0.0215\text{kG}} = 570\text{cm}$$

$$\theta = \sin^{-1}\left(\frac{L_{\text{eff}}}{\rho}\right) = \sin^{-1}\left(\frac{12.6\text{cm}}{570\text{cm}}\right) = 1.26^\circ$$

$$y = (82.5\text{cm})(\tan \theta) = 1.8\text{cm}$$

$$\frac{\text{offset}}{\text{current}} = \frac{1.8\text{cm}}{11} = 0.165\text{cm/amp}$$

An approximate amount of beam displacement per ampere of current supplied to the Lambertson steering coils is 0.17cm per amp.



## APPENDIX B DESCRIPTION OF REX

A general description of the Relativistic Electron Experiment (REX) equipment and an overview of its location was given in the Introduction. This Appendix will give more complete descriptions of the major REX machinery groups.

### I. THE MARX GENERATOR

The Marx generator, manufactured by Maxwell Laboratories of San Diego, California, contains  $62\frac{1}{2}$  stages, 125  $0.32 \mu\text{F}$  capacitors with 160 nF capacitance per stage, and can contain 100 kV maximum charge voltage per stage. Its open circuit peak output voltage is 6.2 MV, output capacitance is 2.56nF, with a stored energy of 49.2kJ. It was designed to drive a 100 ohm load. Its inductance overall is  $9.2\mu\text{H}$ , its resistance is 15 ohms. Its charging time, from a primary power supply of 208Vac, 3 phase, 60Hz, is 50 seconds, and it can deliver a pulse every 5 minutes. To date, it has fired well over 4000 pulses. The Marx generator is housed in a 23.75 feet long, 7 feet wide, and 9.5 feet high 8700 gallon tank filled with mineral oil to prevent flash-over.

The generator internally consists of two 31 stage series connected units. Each stage has two 320nF capacitors, a triggered mid-plane spark-gap switch, and charging and trigger resistors. The first unit also contains the "half-stage," a

single capacitor with a spark gap. Adjacent to the first unit is the internal high voltage power supply assembly, two identical (except for polarity) 60kV units. The power supply assembly is isolated from the Marx units during firing by open contacts. During a Marx charging cycle before firing, constant current is maintained, but current demand decreases, allowing primary voltage to rise. Upon signal from the control room or from a local operator control panel, the 100kV trigger generator next to the Marx tank triggers (fires) both the "half stage" and first "full stage" of the generator, and the capacitors rapidly discharge in series to the final Marx stage, where an 8 turn,  $10\mu\text{H}$   $3/8$ " copper inductor transfers the Marx pulse energy to the water Pulse Forming Line. In the event of a Marx pre-fire, a liquid type retractable resistor ("crowbar") in parallel with the Marx output damps the voltage transferred to the PFL. The "crowbar" may also be used for dummy load test shots. [Ref. 1:pp. 3-9]

## II. PULSE FORMING LINE AND OUTPUT SWITCH

The water-dielectric PFL contains an 11-inch diameter aluminum inner conductor, constantly circulated and deionized water, and a strong outer conductor and housing. It is connected to the Marx output via an oil-water-Lucite diaphragm. Its peak charging voltage is 2.50MV, with 14.4 KJ stored energy. The time it requires to transfer an energy pulse to the next section downstream is 450ns. Its characteristic impedance is 8.0 ohm, equivalent capacitance is 4.6nF, transfer voltage gains is 0.58, and its electrical length is 34.7ns. The water PFL is discharged by a peaker/field shaper and an output switch. The switch self breaks at a setting selected before pulse firing. (The Output Switch is a 60-180 psig pressurized sulfur hexafluoride epoxy-cast device, with 185nH inductance and 30pF capacitance.) To add in peaking the leading edge of the pulse and to maintain field uniformity, the PFL inner conductor is tapered. The pulse exits the PFL via LC filter 1. This filter uses the switch 185nH inductance and has a 150pF capacitance on the glycol side. [Ref. 1:pp. 13-15]

### III. GLYCOL LINE NUMBER ONE

Glycol line number one (GLY1) receives the PFL pulse and provides an impedance match between the PFL and the following section, OL2. Its peak voltage is 1.8MV. Its impedance is 19.2 ohms and its one-way electrical length is 37.6ns. It transfers 73% of the PFL energy (transfer voltage gain 0.73) to the following section, Oil Line 2 (OL2). GLY1 contains no switches. It terminates in a polyurethane diaphragm. The second of two LC filters (LC2) follows the glycol section, with 1.15nH inductance and 75pF capacitance. (The two LC filters aid in the shaping of the pulse. Ideally, the pulse has a "1-cosine" shape, with a 20ns rise/fall, and a 25MHz characteristic frequency. The specific filter designs can be modified to change the pulse rise time and its shape.)

#### IV. OIL LINE NUMBER TWO

OL2 is a 2.7MV peak voltage, oil dielectric section. It is the first section downstream of the Marx to step up pulse voltage; its transfer voltage gain is 1.47. It has a characteristic impedance of 53.3 ohms and a one-way electrical length of 35.6ns. The output of OL2 is tapered to the large diameter of the radial liquid resistor of the output section.

[Ref. 1:pp. 15-16]

## V. OUTPUT SECTION

The output section must receive the OL2 delivered pulse, radially distribute its energy for uniform delivery to the cylindrical cathode stalk, isolate the oil-filled section region from the vacuum environment of the cathode-anode (diode), eliminate cathode surface magnetic fields, and provide an optimum environment for the formation of electrons at the cathode. It must provide a channel for the electrons to exit in the form of a thick stream towards the focusing magnet. Many design trade-offs are made to accomplish all these tasks, and the result may be some residual diode chamber asymmetries. These possible asymmetries are thought to contribute to the excitation of diode resonant modes, which have limited the capacity and power of numerous electron injectors [Ref. 10]. In the case of REX, an asymmetry arises when the OL2 delivered pulse impacts as output, which is a Lucite diaphragm with oil on one side, and a resistive sodium-thiosulfate radial-wedge region on the other side. The sodium-thiosulfate solution matches load impedance and delivers distributed equipotential lines away from an input side coaxial center, forming the eventual linear field lines for the aluminum cathode stalk, and results in a voltage transfer factor of 1.48; but the wedge is possibly slightly thicker at its bottom than at its top due to hydrostatic pressure. (The asymmetry is conducive to dipole mode resonance excitation, and will be corrected in future designs,

but remains a factor to be considered in present REX experiments.) The aluminum cathode stalk is anodized and coated with glyptal paint to prevent emission from its surface. The cathode surface is 2.5 inch diameter velvet, designed for field-emission of electrons. The cathode-anode gap is 15cm, with an accelerating voltage drop of up to 5MV. The anode emission channel diameter is 3 inches. The output section peak voltage is 5.0MV, although 4MV peak voltage and 4kA current is more frequently used. The radial resistor impedance is 175 ohms, the diode load impedance is 1000 ohms, and the electrical length is 5 ns. The current output pulse width is 80-90ns with rise/fall times (10-90%/90-10%) of 15-20ns. [Ref. 1:pp. 16-17]

## VI. SUPPORT SYSTEMS AND DIAGNOSTICS

The support systems circulate fluids, maintain vacuum, and provide controls and diagnostics. The support systems include:

a. A water purification subsystem which deionizes and circulates the water dielectric in the PFL;

b. an oil transfer subsystem with a 12000 gallon storage tank and piping to the Marx tank and transmission line sections with heaters, flow control valves, and purification filters;

c. a cryogenic high vacuum pump and valves for maintaining diode vessel vacuum;

d. synthetic air and sulphur hexafluoride gas pressure control subsystem, with dryers, gauges, and filters (increasing PFL output switch pressure increases its voltage break-down limit and results in a higher voltage pulse);

e. a glycol purification and circulation system;

f. electronic interlocks and safety switches which include the HV power supply, trigger pulse amplifier, gas supply pressures, oil levels in the Marx tank and transmission lines, vacuum pressure, water resistivity, and building access doors;

g. and a diagnostic system with several voltage/current probes (See Figures B-1 thru B-3). Normally,  $V_{PFL}$ ,  $V_{TUBE}$ , and  $I_{DIODE}$  ( $I_{ANODE}$ ) are monitored in the control room for every shot. [Ref. 1:pp. 18-22] For this experiment, two individual B-



dots, such as Top and Bottom, or east and west, or passive divider differenced signals [(T-B) and (E-W)] were also monitored in the control room. Other types of monitors besides B-dots are used; a similar probe measuring the time rate of change of the electric field called an E-dot is one type. The B-dot loop in the Marx trigger generator confirms that the Marx fired on time as required by the output switch gas pressure. An unintegrated E-dot probe in the PFL provides the signal that triggers the oscilloscope traces and streak camera. The  $V_{TUBE}$  and  $I_{TUBE}$  traces monitor the radial resistor region, divertor switch, and pre-pulse switch; if there is a deviation from standard traces, the cause is investigated before continuing to fire the REX assembly [Ref. 2:p. 18].

Figure B-3 is a plot of  $I_{DIODE}$  readings in MV, versus diode current. The 2.5 inch cathode diameter used in the current experiment is shown as the lowest of the three curves. [Ref. 6:p. D-17].

<u>SIGNAL</u>	<u>REX MACHINE</u>	<u>MONITOR</u>
V <sub>PFL</sub>	PFL (E-dot)	80' superflex cable — R7103 scope monitored every shot
Diagnostic Trigger	(E-dot)	80' superflex cable — 26dB Attenuator — Triggerbox 8-way divider — scope triggers
V <sub>GLY1A</sub>	GLY1 (E-dot)	80' superflex cable — R7103 scope
V <sub>GLY1B</sub>	(E-dot)	80' superflex cable — R7103 scope
V <sub>OL2A</sub>	OL2 (E-dot)	80' superflex cable — R7103 scope
V <sub>OL2B</sub>	(E-dot)	80' superflex cable — R7103 scope
V <sub>TUBE</sub>	OL2 End (E-dot)	40' superflex cable — integ — R7103 scope
I <sub>TUBE</sub>	(B-dot)	40' superflex cable — integ — R7103 scope
V <sub>DIODE</sub>	Vacuum Vessel (E-dot)	40' superflex cable — integ — R7103 scope
I <sub>DIODE</sub>	Anode End (4 B-dots)	40' superflex cable — integ — R7103 scope
I <sub>GATE VALVE</sub>	Propagation Pipe (4 B-dots)	40' superflex cable — (integ or subtractor optional) — R7103 scope
I <sub>TRANSPORTED</sub>	(4 B-dots)	40' superflex cable — (integ or subtractor optional) — R7103 scope
STREAK CAMERA PHOTO	Scintillatory Mask Chamber ("can")	Polaroid BW film inspected or hard film every shot

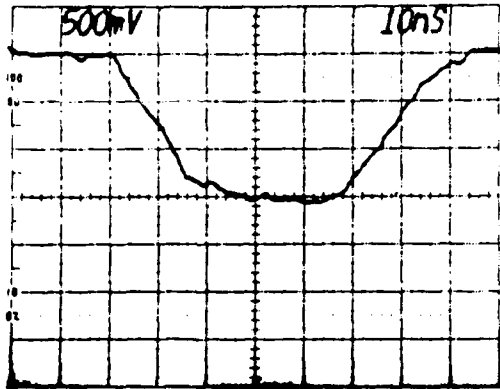
used in troubleshooting

usually monitored every shot

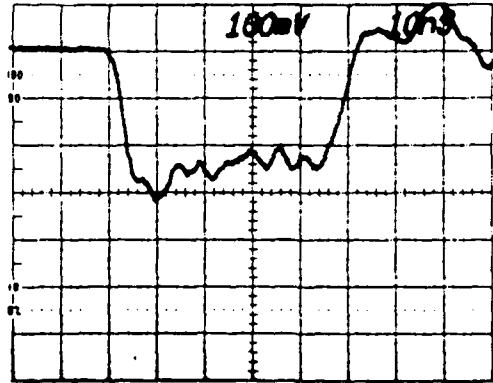
optional monitors

one or more monitored every shot

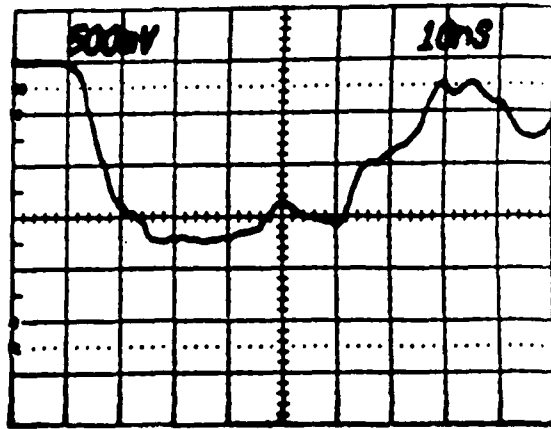
Figure B-1. REX Diagnostic Monitoring



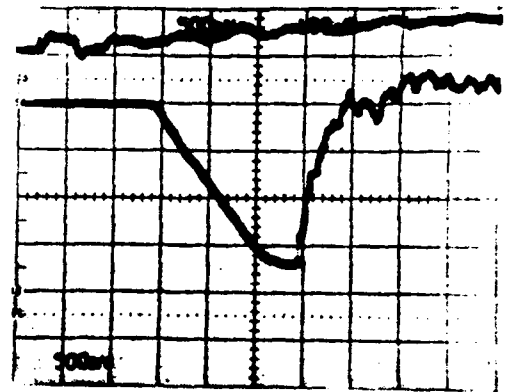
Vtube Monitor  
500 mV/div, 10 ns/div



Itube Monitor  
100 mV/div, 10 ns/div



OL2 Monitor  
0.82 MV/div, 10 ns/div



Top trace: Max Trigger  
Bottom trace: PFL Monitor  
500 mV/div, 100 ns/div

Figure B-2. REX Monitor Waveforms  
[Ref. 1: p 2]

# Diode Current vs Diode Voltage for Several Cathode Diameters

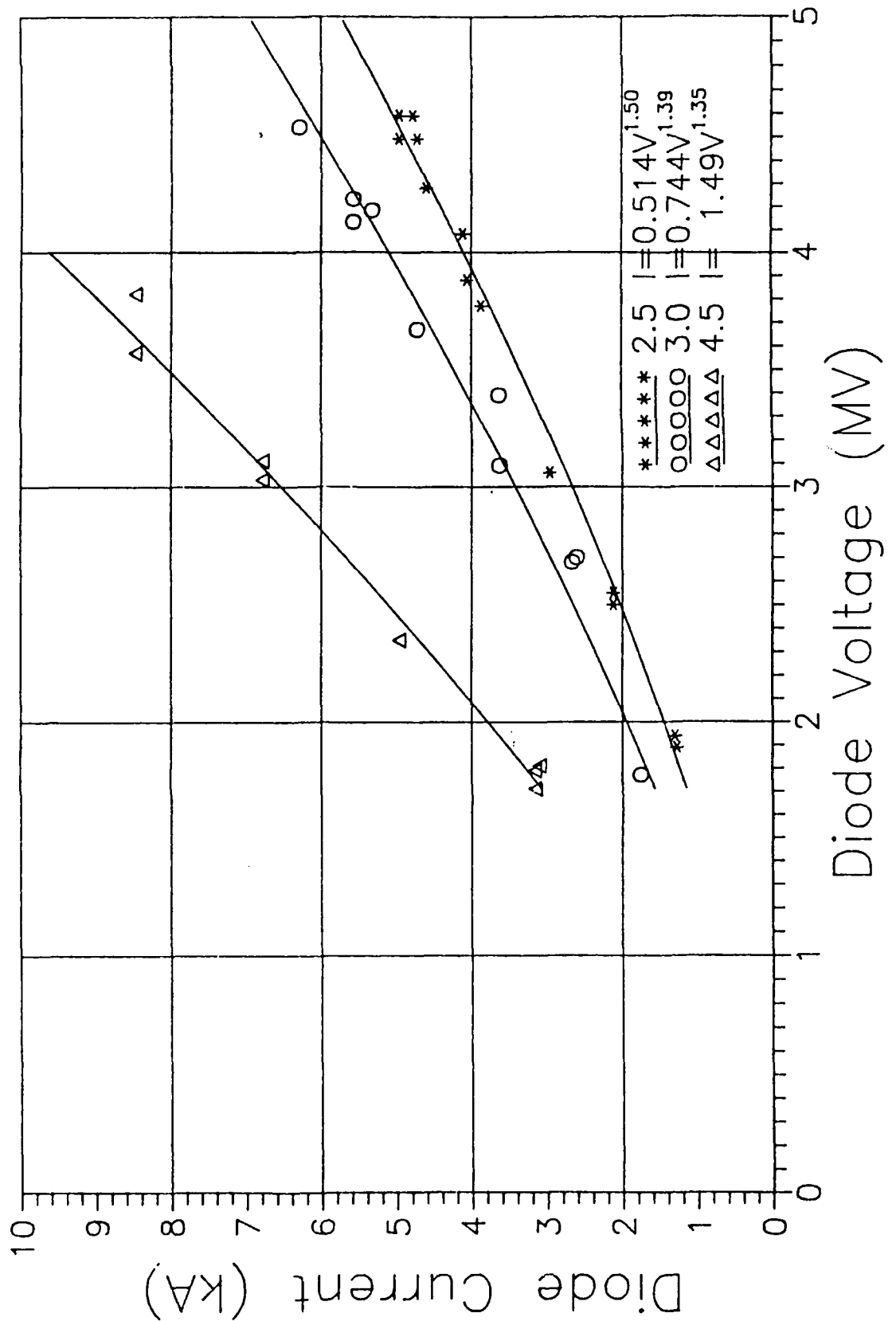


Figure B-3. Diode Current vs Diode Voltage  
for Several Cathode Diameters  
[Ref. 6:p. D-17]

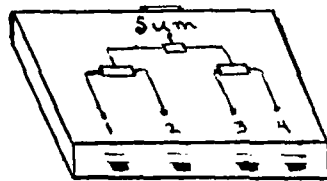
APPENDIX C  
EQUIPMENT

I. PASSIVE MULTIPOINT POWER DIVIDERS/SUMMERS

Passive devices useful in circuits containing B-dots include:

- A. ANZAC MODEL DS-4-4 BROADBAND FOUR WAY POWER ADDER, 2-2000 MHz

This device is most frequently used to sum four B-dot input signals for monitoring electron beam current. See Figure C-1.



ANZAC 4-WAY  
Power Adder

Figure C-1. ANZAC 4-Way Power Adder

Specifications: Amplitude imbalance (port-to-port difference) is 1.0dB in the 1000-2000 MHz range, insertion loss is 2.0dB, phase imbalance is 1.9 to 1, and impedance is 50 ohms. The device performs well in the REX circuits; insertion loss of 2.0dB is not significant with the ample signal available. The port-to-port imbalance results in signal error on the order of 1 percent, an error of the same magnitude as the other equipment sources of error (digitizing camera, oscilloscope,

etc.). The major drawback in this device is the "artificial droop" effect mentioned earlier. See Figure C-2. This effect was noted when the new B-dot rings were used for the first time. The 50 ohm B-dot ports were summed by the ANZAC four-way adder, then the sum signal was integrated by a passive integrator before display on the oscilloscope. The result was the signal shown as Figure C-2(a). At the end of the pulse, the current did not fall off and return to zero (baseline); it fell below the baseline, with a negative amplitude of 5 percent of the current amplitude. To verify that the cause was the new B-dot resistance, the cables were disconnected from the four 50 ohm ports on the B-dot ring, then connected to the four plain-wire B-dot ports. The resulting current pulse is shown as Figure C-2(b). The current returned to baseline, as it should. After some deliberation, it was decided that this systematic error could be noted and accounted for in calculations; it was not necessary to eliminate the use of the ANZAC four-way adder. Its other good qualities -- broad bandwidth, very low self-resonance, low cost, and low imbalance, far outweighed the disadvantage of a five percent current correction factor.

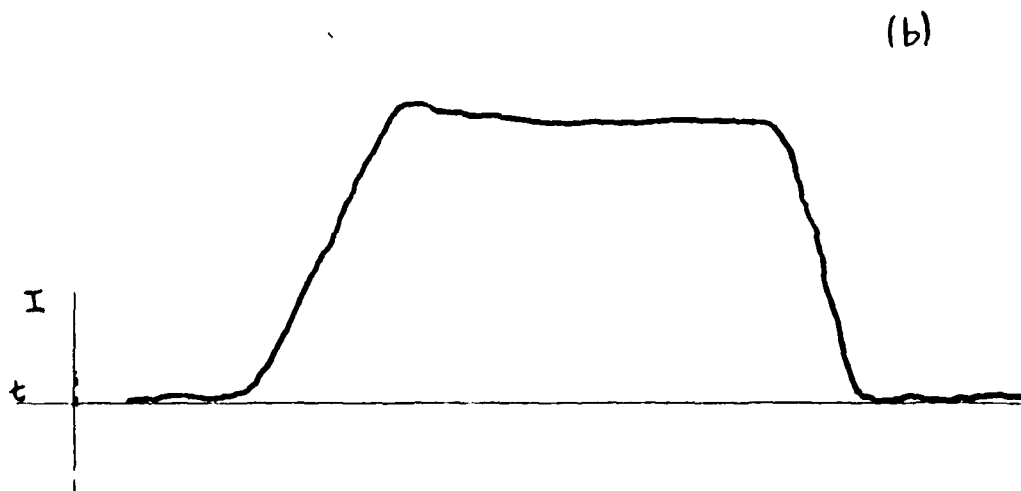


Figure C-2. ANZAC "Artificial Droop" Effect

B. MINI-CIRCUITS MCL ZF SCJ-2 TWO-WAY 180° POWER SPLITTER,  
1MHz - 500 MHz

This device is most frequently used to subtract two B-dot signals. The device adds one input signal 180 degrees out of phase with the other input signal, resulting in a net subtracted output sum. See Figure C-3.

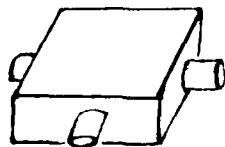


Figure C-3. MCL Two-Way Subtractor

Specifications: Amplitude imbalance is 0.1dB, insertion loss is 0.9dB, VSWR is 1.6 to 1, and impedance is 50 ohms. Nonlinear responses are obtained if input signal voltage exceeds 250v. On the test stand, signals with voltages less than this amount experienced no visible distortion.



## II. E-DOTS (RESISTIVE MONITORS)

Resistive monitors exploit the phenomenon of return current flowing in the conductive walls of the propagation pipe in the presence of an electron beam pulse in the pipe's axis. The basic design is shown in Figure C-4.

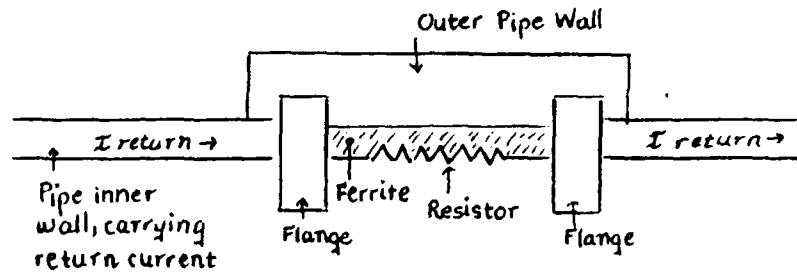


Figure C-4. E-Dot

The current drop across the E-dot's resistor yields the voltage, which is proportional to the electron beam voltage. The E-dot pulse has the actual signal shape; rather than the signal derivative (B-dot). The ferrite prevents signal leakage to the outside. The outer stainless steel coating maintains pipe wall continuity, and has inductor properties, as well; the current flowing through the inner pipe wall is forced to flow through the resistor until the outer wall's time constant ( $T=L/R$ ,  $L$ -inductance,  $R$ =resistance) is reached, then current flows through the stainless steel pipe coating as well. This introduces droop in the signal (See Figure C-5).

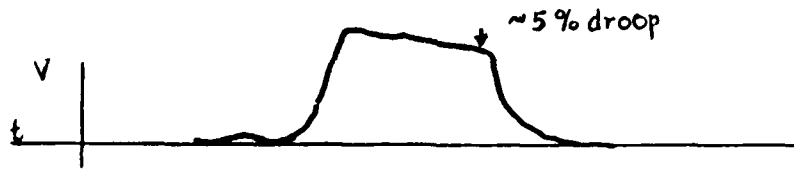


Figure C-5. E-Dot Signal

The ferrite material's permeability changes behavior with frequency, resulting in different E-dot behaviors. This makes the E-dot sensor difficult to use over a broad frequency range. The main use of E-dot monitors in REX is in the water pulse forming line and in the vacuum vessel:  $V_{PFL}$  and  $V_{TUBE}$  are both E-dot signals. E-dot monitors are calibrated with magnetic spectrometers.

### III. STREAK CAMERA

Measurements of one dimension of an electron beam versus time are performed by an Imacon 500 streak camera equipped with a Questar telescope. (Emittance, effective cathode temperature, and current density may also be measured). The REX streak camera is located outside the cement block experimental area shielding, through which a camera viewport passes. See Figures C-6 and C-7. To measure the variation in the vertical (y) dimension of the beam with time, the beam is sent through a brass mask (See Figure C-8) and a strip of Bicron 422 scintillator, or alternatively, through a strip of quartz. In either the scintillator or the quartz, enough light is produced to image on the photocathode of the streak camera. The light is sent to the camera by two tuning mirrors, and is gathered by the 3.5 inch diameter Questar telescope. The camera is triggered from the  $V_{PFL}$  sensor, hence it is temporarily synchronized with the electron beam, and a streak camera image may be obtained on every REX pulse. An example of the resulting image is shown as Figure C-9. (Alternatively, a mask with a vertical array of 17 1mm holes each separated by a 10mm distance, can be used to form the light into a set of parallel beamlets. This type of streak camera image was pictured in the Introduction section of this paper. [Ref. 2:pp. 1-14])

# REX EXPERIMENTAL ARRANGEMENT WITH STREAK CAMERA

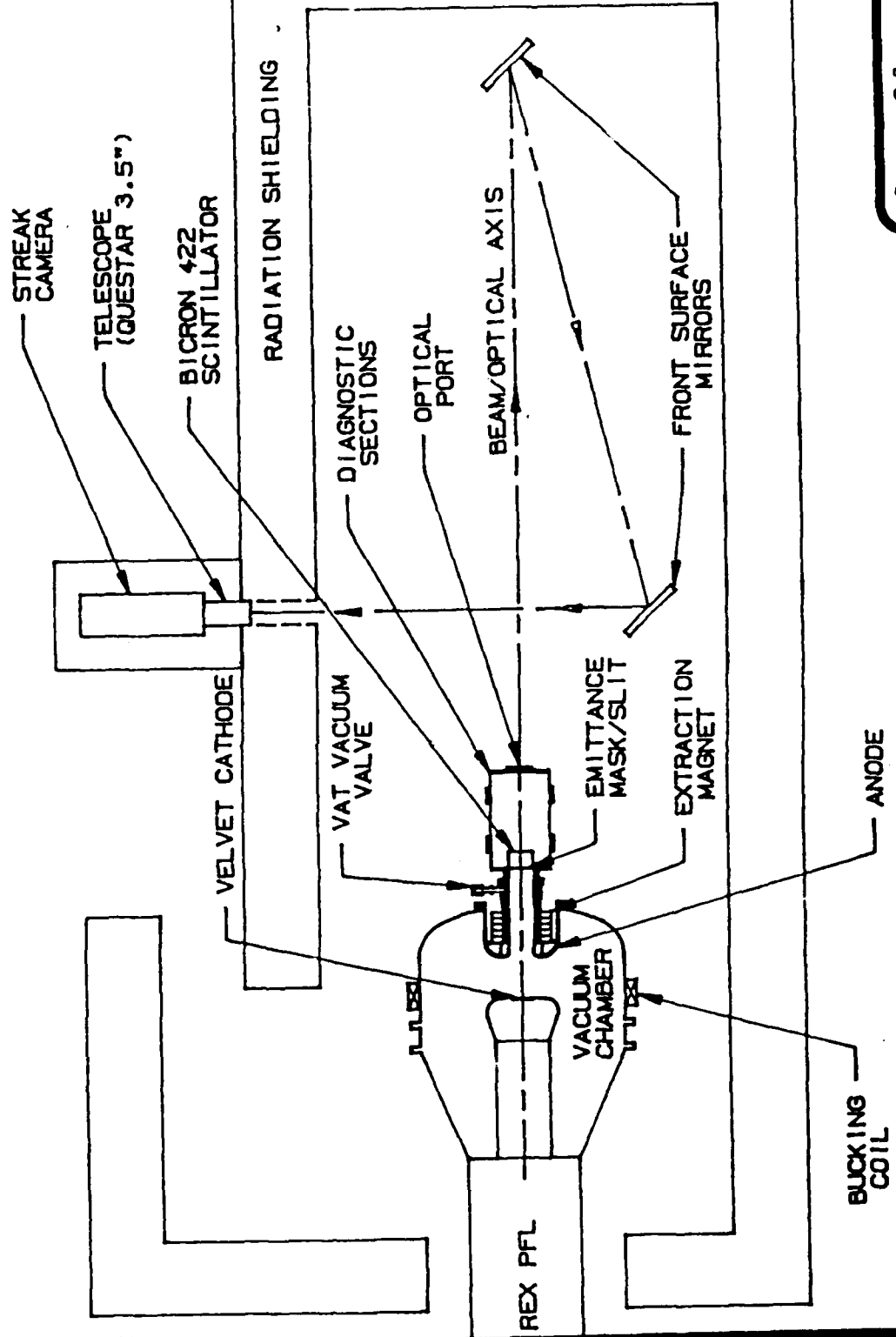


Figure C-6. REX Experimental Arrangement with Streak Camera [Ref. 2:p. 4]

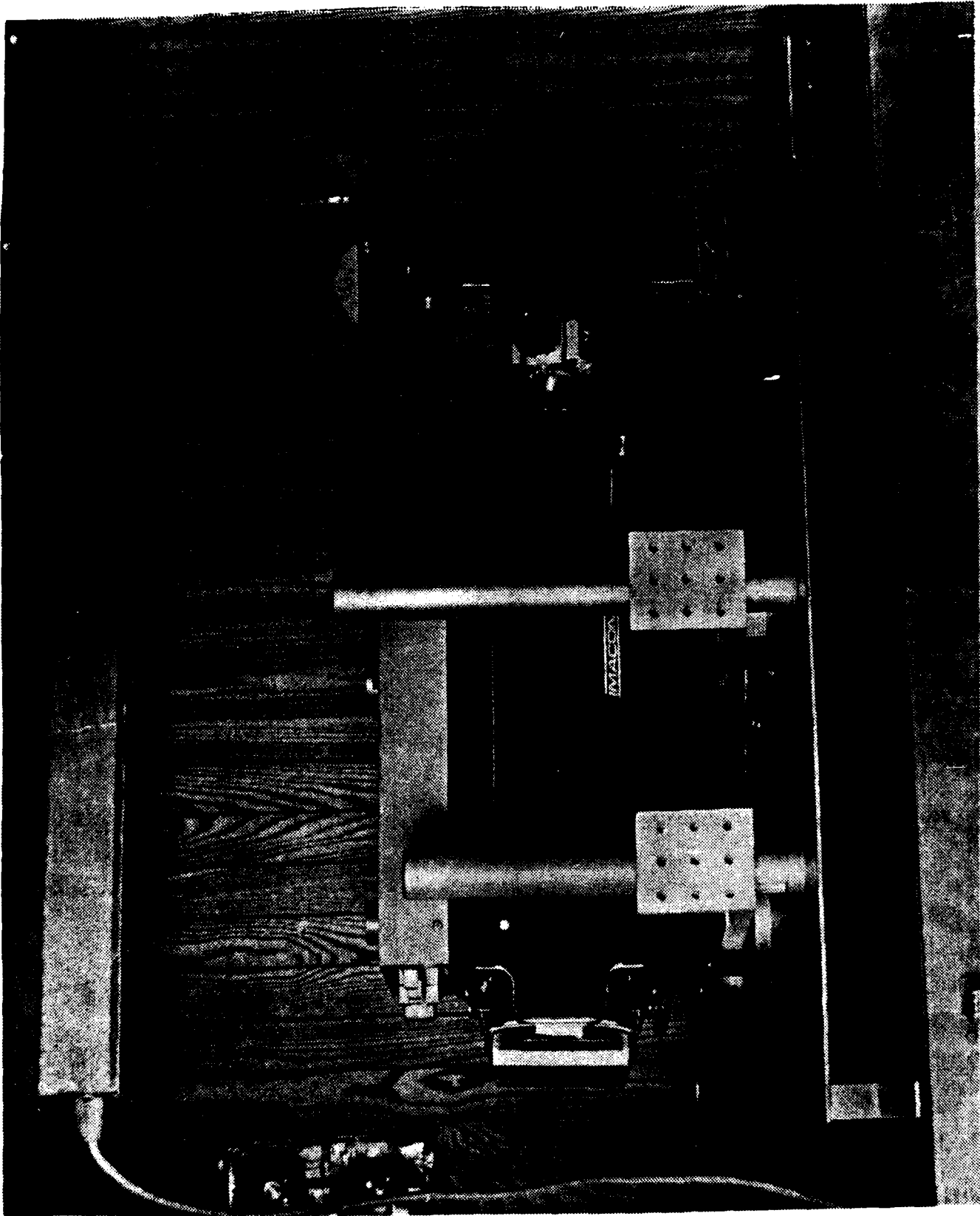
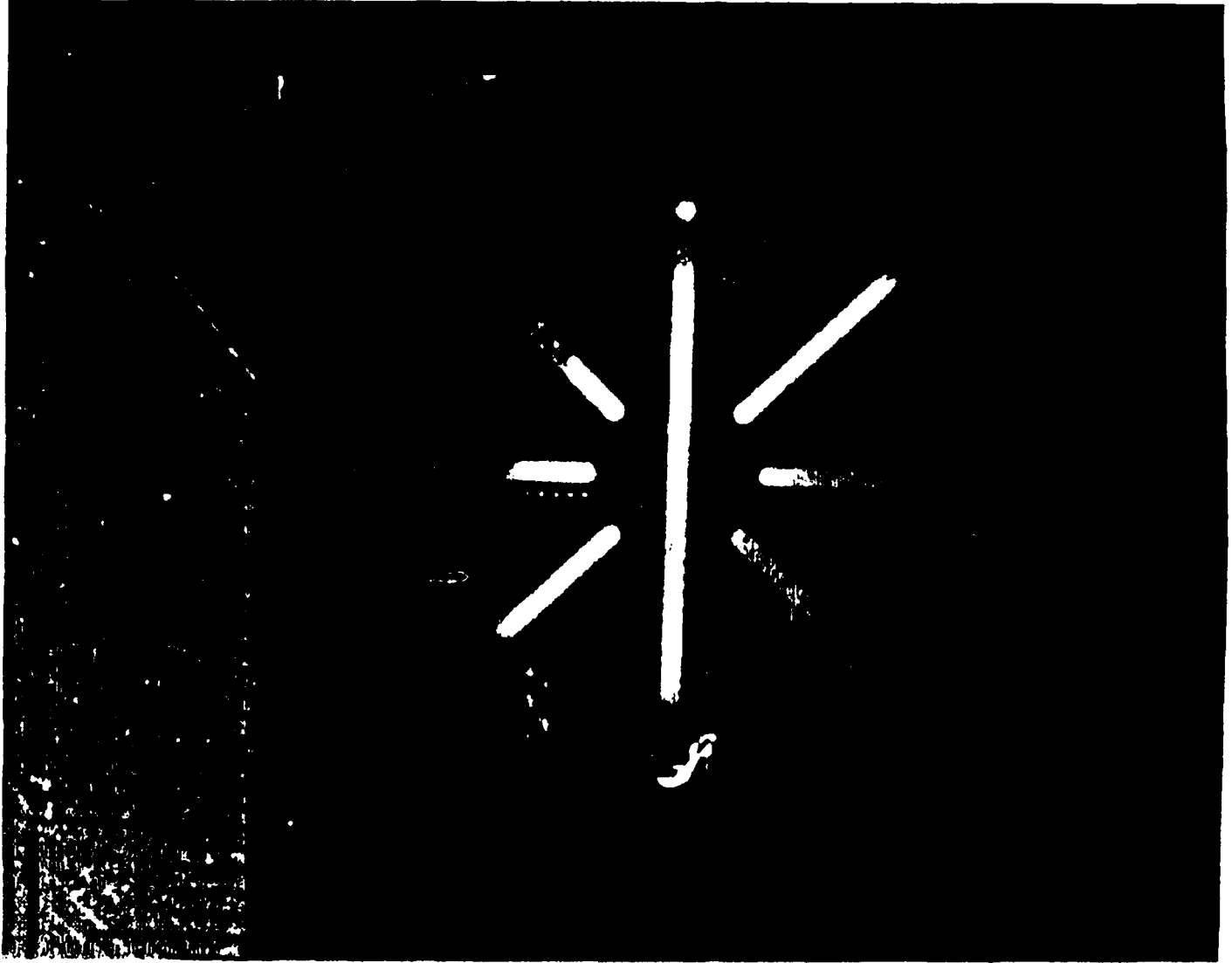
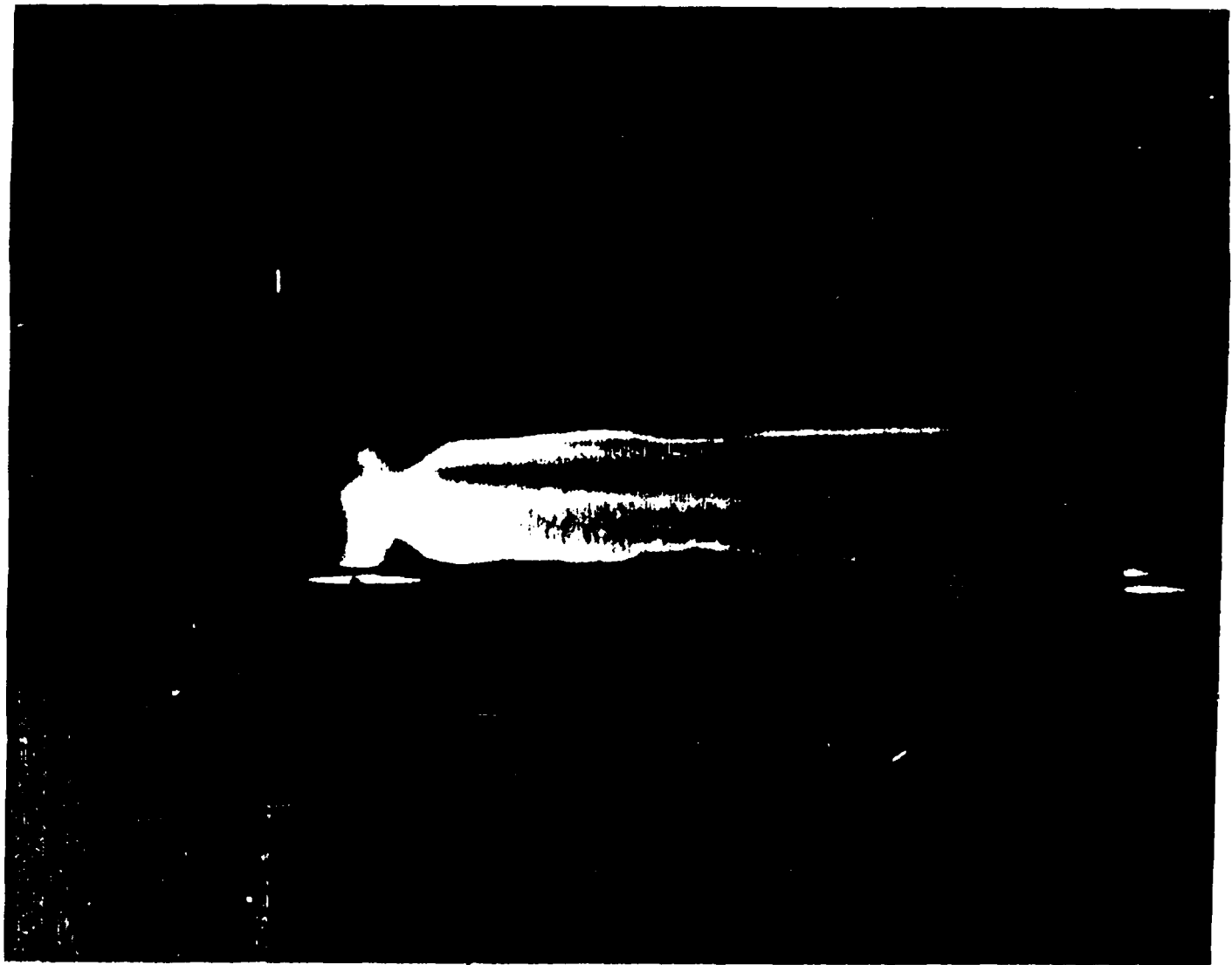


Figure C-7. Streak Camera  
[photo by Mark Martínez]



4226

Figure C-8. Brass Mask



4226

↑  
time  
 $t=0$

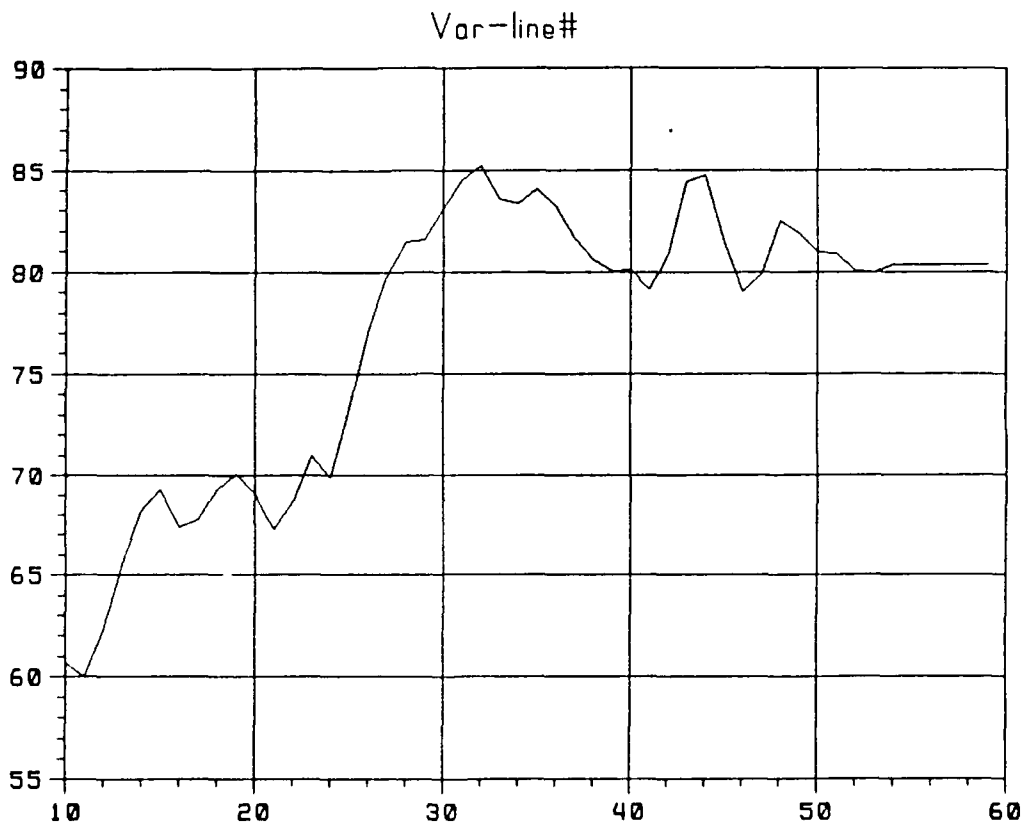
marker indicating  
top of the beam

↑  
time  
 $t=80-90ns$

Figure C-9. Streak Camera Photo

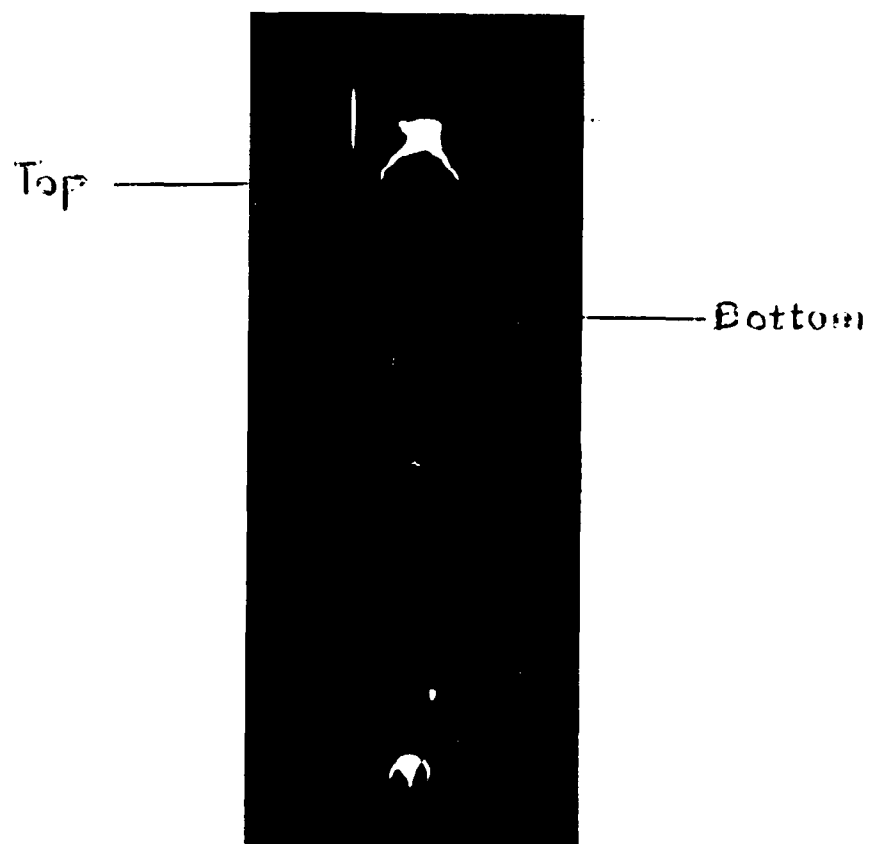
For general analysis, Polaroid film is used in the camera, but for quantitative analysis, Kodak RXP film is used. The resulting Kodak transparent film is scanned with a Perkin-Elmer model 20x20 microdensitometer. Resolution is 400 pixels in the vertical dimension and 600 pixels in the horizontal (time) dimension. The microdensitometer scan in digitized form is stored on a VAX 785 computer for analysis. During the image analysis, corrections for nonlinearities in the camera and film are applied. An example VAX analysis of a beam image is shown as Figure C-10. A close inspection of the beam envelope closest to the marker indicating the beam top reveals peaks and valleys matching the VAX image profile as shown in part (b) of the figure. The analysis and plotting routine used to produce this profile employs integration and smoothing techniques. The average resolution of beam envelope motion for images of the type shown in this figure is 0.5mm (peak-to-peak); for the 1 mm diameter beamlet, beam motion of 100 um can be resolved. [Ref. 2:pp. 1-14]





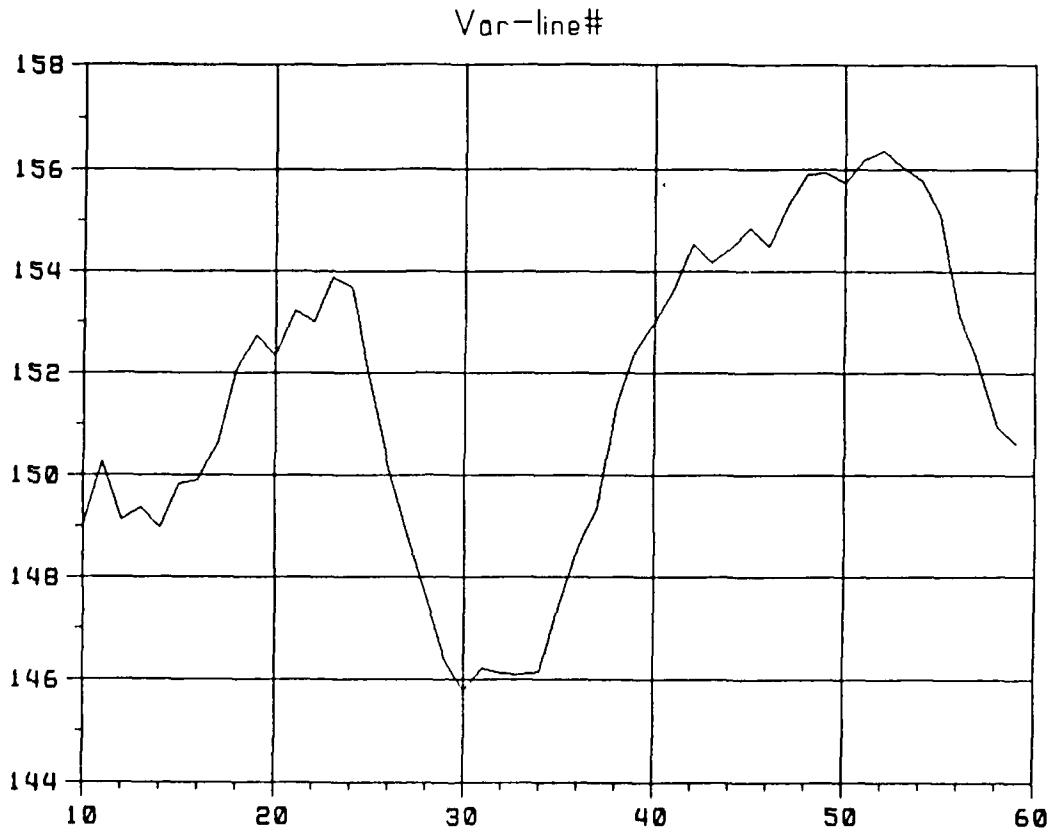
4251 Top edge , freq  $\approx$  246 MHz

Figure C-10(a). VAX/microdensitometer image (shot 4251 top)



4251

Figure C-10(b). Streak Camera Photograph (shot 4251)



File: 111.dat

Var: X center

4251 Bottom edge, freq ≈ 457 MHz

Figure C-10(c). VAX/microdensitometer image (shot 4251, bottom)

#### IV. MISCELLANEOUS EQUIPMENT

##### A. TRANSMISSION CABLES

Heliac 1/2 inch superflexible (solid shield) foam dielectric cable was chosen for the REX experiment. Type FSJ4-50B cable is operable through 10 GHz, has a low VSWR 1.1 to 1, a characteristic impedance of 50 ohms, 82.7 pF/m capacitance, 0.205 uH/m inductance, attenuation of 1.4dB for the 40ft length used, and a 2500v DC breakdown limit. Test stand trials of longer and shorter lengths of this cable showed no visible signal distortion.

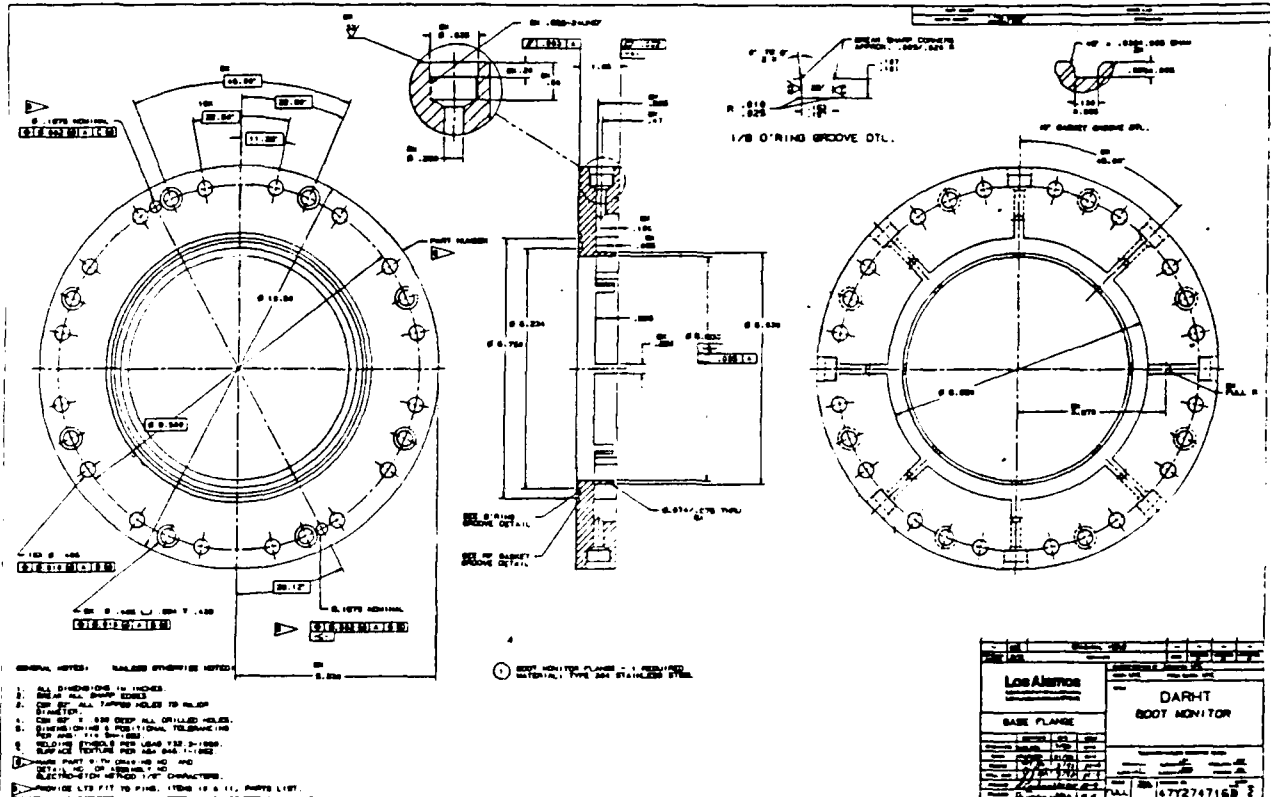
##### B. ATTENUATORS AND INTEGRATORS

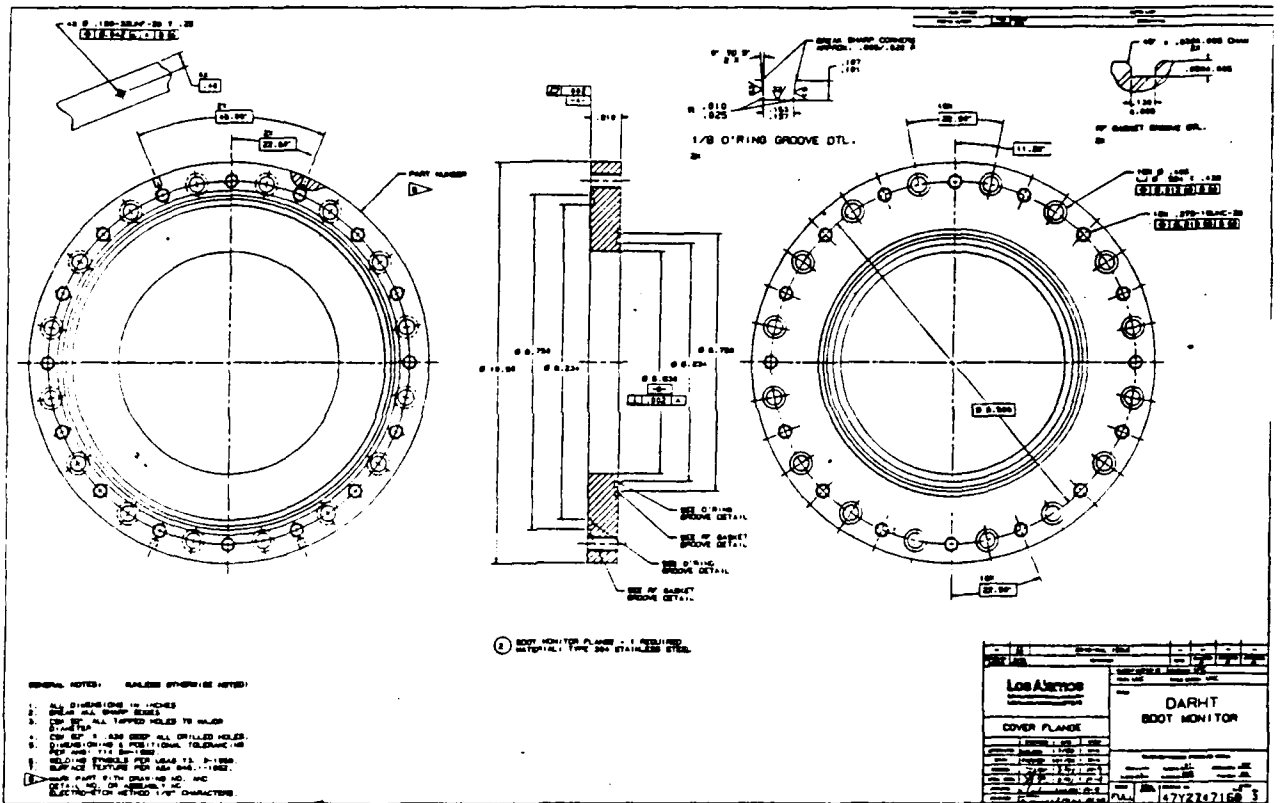
The attenuators used to reduce the signal levels required for oscillator input were manufactured by Applied Research Incorporated, model 24931 UG 89/U. The integrators were manufactured by a M-4 Group at Los Alamos and include a time constant of 1250 ns.

APPENDIX D  
B-DOT DRAWINGS

Detailed drawings of the B-dot sensor and supporting ring are shown as Figure D-1, parts (a), (b), and (c).









APPENDIX E  
DATA TABLES

TABLE 1  
B-DOT PORT-TO-PORT DIFFERENCE MEASUREMENTS  
02 MAR 90

B-DOT RING	PORT AREA (n Vs)	AVERAGE AREA* (n Vs)	PORT DIFFERENCE* (% ABOVE AND BELOW AVERAGE
ABR1	TOP 0.9104	50 $\Omega$ 0.9150	0.90% below
	EAST 0.9181		0.05% below
	BTM 0.9319		1.45% above
	WEST 0.9138		0.50% below
	WIRE1 1.85		2.07% below
	WIRE2 1.87		-0-
	WIRE3 1.89		1.07% above
	WIRE4 1.87		-0-
	Wire:1.87		
ABR2	TOP 0.9049	50 $\Omega$ : 0.91615	1.23% below
	EAST 0.9909		0.98% above
	BTM 0.9247		0.93% above
	WEST 0.9251		0.68% below
	WIRE1 1.90		0.66% above
	WIRE2 1.89		0.13% above
	WIRE3 1.88		0.40% below
	WIRE4 1.88		0.40% below
	Wire:1.8875		

\* "Average Area" =  $\frac{T + B + E + W}{4}$  or  $\frac{1 + 2 + 3 + 4}{4}$

+ "Port Difference" =  $\frac{(\text{Avg Area}) - (\text{Port Area})}{\text{Avg Area}}$

TABLE 1 CONT.

Measurements taken 20 Mar 90

ABR1	TOP		2.03% below
	EAST		0.31% above
	BOTTOM	0.969375	0.90% above
	WEST		0.83% above
ABR2	TOP		2.19% below
	EAST		0.40% above
	BOTTOM	0.969825	1.11% above
	WEST		0.60% above
	WIRE1 1.90		1.30% below
	WIRE2 1.93		0.26% above
	WIRE3 1.94	1.925	0.78% above
	WIRE4 1.93		0.26% above
	TOP 0.9432		3.21% below
	EAST 0.9843		1.90% above
	BTM 1.000		2.62% above
	WEST 0.9705	50n 0.9745	1.10% below
	WIRE1 1.93		1.03% below
	WIRE2 1.98		1.54% above
	WIRE3 1.97		1.03% above
	WIRE4 1.92	Wire 1.95	1.54% below
TOP 0.9325		2.70% below	
EAST 0.971		1.32% above	
BTM 0.9769		1.93% above	
WEST 0.953	50n 0.95835	0.56% below	
WIRE1 1.94		1.52% below	
WIRE2 2.01		2.03% above	
WIRE3 1.99		1.06% above	
WIRE4 1.94	Wire 1.97	1.52% below	
TOP 0.9441		2.35% below	
EAST 0.9775		1.01% below	
BTM 0.9885		2.24% above	
WEST 0.9574	50n 0.966875	0.98% below	
WIRE1 1.94		0.90% below	
WIRE2 2.00		2.17% above	
WIRE3 1.97		0.64% above	
WIRE4 1.92	1.9575	1.92% below	
TOP 0.9422		2.04% below	
EAST 0.9762		1.45% above	
BTM 0.9736		1.23% above	
WEST 0.9552	0.9618	0.69% below	

TABLE 1 CONT.

Over all the 20 March ABR2 data sets, the average port-to-port differences are:

for ABR2 Fluke 8840A  
Multimeter Resistor  
Readings

TOP	2.5 ± 0.5% below average	
EAST	1.2 ± 0.2% above average	
BOTTOM	2.0 ± 0.6% above average	51.90 ohms
WEST	0.7 ± 0.2% below average	51.17 ohms
WIRE1	1.2 ± 0.3% below average	50.50 ohms
WIRE2	1.9 ± 0.2% above average	51.90 ohms
WIRE3	0.9 ± 0.2% above average	
WIRE4	1.7 ± 0.2% below average	

for ABR1

TOP	1.8 ± 0.5% below average	
EAST	0.5 ± 0.3% above average	
BOTTOM	0.9 ± 0.1% above average	
WEST	0.6 ± 0.4% above average	
WIRE1	1.2 ± 0.2% below average	
WIRE2	0.2 ± 0.1% above average	
WIRE3	0.9 ± 0.2% above average	
WIRE4	0.2 ± 0.1% above average	

TABLE 2  
B-DOT PORT LOOP AREA MEASUREMENTS

B-DOT RING	PORT	PIN HEIGHT (INCHES)	PIN TAB TO WALL (INCHES)	THEORETICAL LOOP AREA (PRODUCT) (SQ. INCHES)
TEST STAND B-DOT RING	1	0.394, 0.394	0.397, 0.397	
	2	0.401, 0.400	0.396, 0.396	
	3	0.405, 0.403	0.399, 0.396	
	4	0.403, 0.403	0.398, 0.396	
	5	0.403, 0.404	0.397, 0.398	
	6	0.391, 0.392	0.398, 0.396	
	7	0.393, 0.394	0.396, 0.396	
	8	0.400, 0.401	0.396, 0.399	
		AVERAGE PIN HEIGHT (INCHES)	AVERAGE TAB TO WALL (INCHES)	
		0.3940	0.3970	0.156418
		0.4005	0.3960	0.158598
		0.4040	0.3975	0.160590
		0.4030	0.3970	0.15999
		0.4035	0.3975	0.16039
		0.3915	0.3970	0.15543
		0.3945	0.3960	0.15622
		0.4005	0.3975	0.15920

Average pin height, all ports = 0.399 ± .005 in.

Average tab to wall, all ports = 0.397 ± .001 in.

Average loop area, all ports = 0.1584 ± .0020 sq. in.

TABLE 2 CONT.

		PORT DIFFERENCE (PERCENT) ( <u>Avg area - Port area</u> (100)) Avg area		
	1	1.25		
	2	-0.13		
	3	-.138		
	4	-1.00		
	5	-1.26		
	6	1.88		
	7	1.38		
	8	-0.51		

TABLE 2 CONT.

B-DOT RING	PT	PIN HEIGHT (INCHES)	PIN TAB TO WALL (INCHES)	THEO. LOOP AREA (PROD) (SQ. IN)
ABR2  P1=Top P2=Wire1 P3=East P4=Wire2 P5=Btm P6=Wire3 P7=West P8=Wire4	1	0.402,0.402,0.403	0.396,0.397,0.398	
	2	0.404,0.403,0.403	0.396,0.306,0.306	
	3	0.405,0.407,0.405	0.305,0.306,0.395	
	4	0.407,0.406,0.406	0.396,0.397,0.396	
	5	0.401,0.404,0.401	0.396,0.397,0.396	
	6	0.404,0.405,0.403	0.397,0.396,0.398	
	7	0.406,0.403,0.404	0.395,0.397,0.396	
	8	0.402,0.402,0.401	0.395,0.395,0.397	
		AVERAGE PIN HEIGHT (INCHES)	AVERAGE TAB TO WALL (INCHES)	
	1	0.4023	0.3970	0.159713
	2	0.4033	0.3960	0.159707
	3	0.4057	0.3953	0.160373
	4	0.4063	0.3963	0.161017
	5	0.4017	0.3963	0.159194
	6	0.4040	0.3970	0.160388
	7	0.4043	0.3960	0.160103
	8	0.4017	0.3957	0.158953

P=port

Average pin height, all ports =  $0.404 \pm .002$  in.Average tab to wall, all ports =  $0.396 \pm .001$  in.Average loop area, all ports =  $0.1600 \pm 0.003$  sq. in.

TABLE 2 CONT.

		PORT DIFFERENCE (PERCENT) $(\text{Avg area} - \text{Port area}) / (100)$ Avg area		
	1	0.18		
	2	0.18		
	3	-0.23		
	4	-0.64		
	5	-0.50		
	6	-0.24		
	7	-0.06		
	8	0.65		

TABLE 3  
EFFECTIVE LOOP AREA CALIBRATION FACTORS

B-DOT RING	PORT	MAG. (pk-pk, v)	PRED. MAG. Eq. (14), Tab II Areas (v)	CALIB. FACTOR
ABR2 MEASMT SET 1 (ROUGH)	TOP	0.2245	0.177	1.268
	WEST	0.2279	0.176	1.295
	BTM	0.2313	0.173	1.337
	EAST	0.2286	0.173	1.318
MEASMT SET 2	TOP	0.1648	0.1398	1.179
	WEST	0.1734	0.1420	1.221
	BTM	0.1743	0.1464	1.191
	EAST	0.1682	0.1435	1.172
MEASMT SET 3	TOP	0.1665	0.1383	1.204
	WEST	0.1695	0.1405	1.206
	BTM	0.1752	0.1448	1.210
	EAST	0.1735	0.1412	1.229
MEASMT SET 4	TOP	0.1680	0.1416	1.186
	WEST	0.1710	0.1438	1.189
	BTM	0.1762	0.1482	1.189
	EAST	0.1742	0.1453	1.199
MEASMT SET 5	TOP	0.1595	0.1371	1.163
	WEST	0.1632	0.1392	1.172
	BTM	0.1693	0.1435	1.180
	EAST	0.1681	0.1407	1.195

Average Loop Area Calibration Factors  
(Excluding Measurement Set 1, a rough set)

Top	1.183 ± 0.017
West	1.197 ± 0.021
Bottom	1.193 ± 0.013
East	1.199 ± 0.023

Average of all four = 1.193



```

a='' ; a string variable
file=''
scope_header=strarr(80,30) ;for the scope setup
time=fltarr(512) ;waveform time
waveform=fltarr(512) ;the waveform volts
; Get and open the scope waveform file name
read,'TEKTRONIX DCS waveform file name',file
openr,1,file
; Read the waveform header info and waveform
i=0
while not EOF(1) do begin
  if ((i gt 19) and (i lt 532)) then begin
    ;read the waveform numbers
    readf,1,'$(f8.6)',f
    waveform(i-20)=f
  endif else begin ;read header info
    readf,1,a
    scope_header(i)=a
  endelse
  i=i+1
endwhile
; Parse the waveform header for needed parameters
camera_number=STRMID(scope_header(3),STRPOS(scope_header(3),':')+2,3)
pos1=STRPOS(scope_header(6),':')+2
waveform_start=STRTRIM(STRMID(scope_header(6),pos1,3),2)
pos1=STRPOS(scope_header(7),':')+2
waveform_stop=STRTRIM(STRMID(scope_header(7),pos1,3),2)
date=STRTRIM($
  STRMID(scope_header(8),STRPOS(scope_header(8),':')+2,30),2)
pos1=STRPOS(scope_header(10),':')+2
horiz=STRTRIM(STRMID(scope_header(10),pos1,20),2)
pos1=STRPOS(scope_header(11),':')+2
vert=STRTRIM(STRMID(scope_header(11),pos1,20),2)
pos1=STRPOS(scope_header(12),':')+2
time_per_point=STRTRIM(STRMID(scope_header(12),pos1,20),2)
pos1=STRPOS(scope_header(13),':')+2
volts_per_point=STRTRIM(STRMID(scope_header(13),pos1,20),2)
; Set the plot title and axes labels
; case vert of
; '5.000000e-02': !YTITLE='50mVolts/DIV'
; else: !YTITLE=vert='Volts/DIV'
; endcase
; case horiz of
; '5.000000e-05': !XTITLE='50u-sec/DIV'
; else: !XTITLE=horiz+'Time/DIV'
; endcase
; Set up for plotting
!XTICKS=-10 & !YTICKS=-8 & !GRID=10 & !TYPE=4
; SET_XY, FIX(waveform_start), FIX(waveform_stop)
time=indgen(512)
newwave=fltarr(512)
SET_PLOT,1
; Plot the waveform, properly scaled
print,'camera number ',camera_number
print,'waveform start ',waveform_start
print,'waveform stop ',waveform_stop
print,'date ',date
print,'horizontal time setting ',horiz
print,'vertical voltage steeing ',vert
print,'time per point ',time_per_point
print,'volts per point ',volts_per_point

read,'press 1 AND THEN PRESS RETURN to display waveform',t
start=fix(waveform_start)& stop=fix(waveform_stop)
plot,time(start:stop),waveform(start:stop)
plot,waveform(start:stop)
print,'Use cursor to select range for FFT'
cursor,s1,s2,x1,y1
cursor,s1,s2,x2,y2
newwave=waveform(x1:x2)
plot,newwave
STOP
newwavef=abs(fft(newwave,-1))
plot,newwavef
norm=x2-x1
f=1/norm
xnorm=fltarr(norm)
for i=0,norm-1 do xnorm(i)=i
inter=time_per_point*norm
xnorm=xnorm/norm
xnorm=xnorm/time_per_point
!xmax=xnorm(norm-1)/2
plot,xnorm,newwavef
read,'input lower frequency of plot',t2
!xmin=t2
read,'input max freq of plot',t
!xmax=t
plot,xnorm,newwavef
; Finish up
close,1
PRINT,'THIS IS THE ENDDDDDDDDDD!!!!!!'
end

```

## REFERENCES

1. Carlson, R.L., Relativistic Beam Experiment (REX) Accelerator Design and Performance, Los Alamos National Laboratory Report M-4:GR-88-8, September 1988.
2. Kouppila, T.J., Builta, L.A., Carlson, R.L., et al. The Measurement of Electron Beam Emittance Using Streak Cameras and Image Analysis Techniques, Los Alamos National Laboratory Report LAUR-90-1109, March 1990.
3. Carlson, R.L., Ridlon, R.N., and Stout, L.E., Multigigahertz Beam Current and Position Monitor for Relativistic Electron Beams, Rev. Sci. Instrum. 57(10), October 1986.
4. Caporaso, G.J., Cole, A.G., and Struve, K.W., Beam Breakup (BBU) Instability Experiments on the Experimental Test Accelerator (ETA) and Predictions for the Advanced Test Accelerator (ATA), IEEE Trans. Nuc. Sci., Vol. NS-30(4), August 1983.
5. Hughes, T.P., Clark, R.M., Carlson, R.L., et al, Diode and Transport Calculations for REX, DARHT, and PHERMEX, Mission Research Corporation Report MRC/ABQ-R-1244, February 1990.
6. Hughes, T.P., Carlson, R.L. and Moir, D.C., High Brightness Electron Beam Generation and Transport, Los Alamos National Laboratory Report LA-UR-89-3367, February 1990.
7. Schneider, R.F., Nguyen, K.T., Smith, J.R., et al, Instability Measurements of an Intense Relativistic Electron Beam Propagating in an Ion Focussing Regime Channel, Proceedings of the IEEE 187 Particle Accelerator Conference, Vol. 2, September 1987.
8. Wright, L., Differenced B- $\theta$  Loop Signals Including Contributions of Return Current, Mission Research Corporation Calculation notes (undated)
9. Carlon, R.L. and Stout, L.E., A Multigigahertz Beam-Current and Position Monitor, IEEE Trans. Nuc. Sci., Vol. NS-32(5), October 1985.
10. Hughes, T.P., Clark, R.M., Carlson, R.L., et al, Beam Generation and Transport on REX:Theory and Experiment,

Mission Research Corporation Report MRC/ABQ-R-1133, February 1989.

11. Product Group 58, Tekware DCSOL Digitizing Camera System Instruction Manual 070-7230-00, Tektronix Corporation, August 1988.

12. Burns, M., Calculations for REX Steering Magnets, Los Alamos National Laboratory, notes and calculations, March 1990.

## BIBLIOGRAPHY

Caporaso, G.J. and Struve, K.W., Experimental Studies of the Beam Breakup Mode on ETA: Comparison with Theory, Lawrence Livermore National Laboratory Report UCID-19402, January 1982.

Carlson, R.L., A Shot in the Arm for Accelerator Technology, Los Alamos National Laboratory Research Highlights 1989, LALP-89-42, March 1990.

DeFord, J.F., Craig, G.D. and McLeod, R.R., The Amos Wakefield Code, Lawrence Livermore National Laboratory Report UCRL-102731, January 1990.

Fessenden, T.J., Stallard, B.W. and Berg, G.G., Beam Current and Position Monitor for the Astron Accelerator, Rev. Sci. Instrum. 43(12), December 1972.

Hughes, T.P., Mostrom, M.A. and Mack, J.M., Simulations of REX Diode and Focussing Magnet, Mission Research Corporation Report AMRC-R-987, October 1987.

Prono, D.S., et al, First Studies of ATA Injector, Lawrence Livermore National Laboratory Report UCID-19862, August 1983.

Struve, K.W., ATA Injector Noise Levels from Differenced B- $\theta$  Loops, Lawrence Livermore National Laboratory Beam Physics Note 50, February 1983.

Struve, K.W., Differenced B- $\theta$  Loops for Measuring Low Level Excitations of the Beam Breakup Instability in Linear Accelerations, Lawrence Livermore National Laboratory notes, September 1985.